ABSTRACT

Title of Document:	DIRECTED SELF-ASSEMBLY OF NANOSTRUCTURES AND THE OBSERVATIONS OF SELF-LIMITING GROWTH OF MOUNDS ON PATTERNED CRYSTAL SURFACE DURING EPITAXIAL GROWTH
	Chuan-Fu Lin, Doctor of Philosophy, 2012
Directed By:	Professor Raymond J. Phaneuf, Department of Materials Science and Engineering

In this thesis I describe an approach toward investigating moving interfaces, surface stabilities and directing self assembly of nanostructures, using lithographic patterning to perturb a flat crystalline surface over a range of spatial frequencies, followed by epitaxial growth. GaAs(001) shows a transient instability toward topographical perturbations. We model this behavior using an Ehrlich-Schwoebel (ES) barrier which impedes the diffusion of atoms across steps from above. We show via both kinetic Monte Carlo (kMC) simulations and molecular beam epitaxial (MBE) growth experiments that patterning in the presence of an ES barrier can be used to direct the self assembly of mounds.

Second, as we track the time evolution of mound formation, we find the evidence of "Self-Limiting Growth" on surfaces - we find that in the initial stage of growth, the pattern directs the spontaneous formation of multilayer islands at 2-fold

bridge sites between neighboring nanopits along [110] crystal orientation, seemingly due to the presence of an Ehrlich-Schwoebel barrier and the effect of heterogeneous nucleation sites on the surfaces. However, as growth continues, the height of mounds at 2-fold bridge sites "self-limits": the mounds cease to grow. Beyond this point an initially less favored 4-fold bridge sites dominate, and a different pattern of self assembled mounds begins. The observation of self-limiting behavior brings us new understanding of mechanism for crystal growth. We also find that the transient amplification of pattern corrugation during growth is correlated with self-limiting behavior of mounds. We propose that a minimum, 'critical terrace size' at the top of each mound is responsible for the observed self-limiting growth behavior.

Finally, the observation of the sequence of the mounds forming on the patterned surfaces gives us rather direct evidence that the formation of growth mounds on the surface is a nucleated process, rather than an instability.

DIRECTED SELF-ASSEMBLY OF NANOSTRUCTURES AND THE OBSERVATIONS OF SELF-LIMITING GROWTH OF MOUNDS ON PATTERNED CRYSTAL SURFACE DURING EPITAXIAL GROWTH

By

Chuan-Fu Lin

Dissertation submitted to the Faculty of the Graduate School of the
University of Maryland, College Park, in partial fulfillment
of the requirements for the degree of
Doctor of Philosophy
2012

Advisory Committee:
Professor Raymond J. Phaneuf, Chair
Professor Robert M. Briber
Professor Theodore L. Einstein
Professor Manfred Wuttig
Professor Mario Dagenais

Dedication

To my parents, Hsieh-Huang Lin（林燮煌）*and Pin-Shia Chiang*（江蘋霞）*,*

and my wife, Yuyun Peng（彭郁云）

for their love, supports and encouragements

In memory of my grandmother, Hong-Juan Zhu（江朱紅娟）*, (1930-2011)*

Acknowledgements

I am deeply grateful to my Ph.D. advisor, Prof. Raymond Phaneuf, for his full support, encouragement, inspiration throughout my Ph.D. study. He gave me a great chance to involve in very interesting topics in the field of surface science, and through which I learned how to deal with scientific problems, think critically and solve problems with maturity. His scientific enthusiasm, curiosity and insights direct and inspire me greatly in my research. Besides, I would like to thank him for showing me a role model of being a great scientist and a great mentor who always advises me at every important moment and push me forward to overcome the barriers I met in my Ph.D. career. Overall, I am grateful to have the opportunity to work with him for the past few years.

I would like to give a special thank to Prof. Hung-Chih Kan, who encouraged and helped me start my Ph.D. study at the University of Maryland. He always provides valuable scientific insights, guidance and supports while working with him. He is also an example of great scientists that I would like to follow, and it is really a privilege to interact and work with him as a team.

I would like to thank my collaborators for their great contributions in my research and this dissertation. I appreciate Dr. Christopher Richardson, Dr. Kanakaraju Subramaniam for providing excellent MBE facilities and helping me out with MBE growth; Prof. Ajmi B. H. Hammouda for providing initial Fortran codes of kMC calculations; Prof. Timothy Corrigan and Dr. Ben Palmer for giving assistance of E-beam lithography; Laurence C. Olver, Scott Horst and Steven Brown for helping me in the cleanroom; Chih-Feng Wang and a few of REU students for their help with

the AFM measurements and data analysis.

Special acknowledgement to the members of my thesis committees: Professor Manfred Wutting, Professor Theodore L. Einstein , Professor Robert M. Briber, and Professor Mario Dagenais. They are all inspiring professors, and it's really my great honor to have them sit in my committee.

Also, I would like to thank my colleagues and friends, Tsung-Cheng Lin, Chih-Feng Wang, Dr. Tim Corrigan, Dr. Sherman Guo, Dr. Shu-Ju Tsai, Dominic Britti, Amy Marquardt and Miriam Cezza, who have been liberally sharing thoughts and giving assistance during the past four years

Finally, I would like to express maximum gratitude to my parents, Hsieh-Huang Lin and Pin-Shia Chiang, and my sisters, Mu-Yu Lin, Ching-Yun Lin and their families for their endless love, prayers and support. I would also thank the Chiang's family for their gentle care and accompany. A special thank to my wife Yuyun Peng for her love and thoughtfulness during these years, and my lovely son, Benjamin Ken Lin and my daughter, Elizabeth Chiao Lin for the joy they gave me and the precious moments being with them.

My greatest appreciation to the Lord, Jesus Christ. It is Him who makes everything possible.

Table of Contents

List of Tables

List of Figures

Chapter One:

Chapter Two:

Chapter Three:

Chapter Four:

Appendix A:

Appendix B:

Chapter One

Introduction

1.1 Motivation and Goals

One of the motivations of this work is that based on the timetable of Moore's Law [1.1] and the international technology roadmap for semiconductors [1.2], the conventional fabrication of devices is reaching the limit, so that one of the grand challenges in nanotechnology is achieving the fabrication of huge density of nanometer-sized structures with controlled placement, on a practical time scale. Intensive efforts have been put into the combination of templating the substrates and spontaneously assembly of structures, which is a potential candidate to break through the bottleneck of nanotechnology. However, in the systems reported earlier, they typically involved local chemistry [1.3] or strain [1.4-1.6] as the driving forces for directing self assembly of nanostructures. It would be interesting and important to understand under what conditions kinetic effects, such as the Ehrlich-Schwoebel barrier, which oppose the crossing of steps from above by diffusing adatoms, can also

be used as a mean of directing assembly of nanostructures. In chapter three of this thesis, we present simulations predicting that indeed directed of self assembly of nanostructures through patterning the substrate, and in the presence of an Ehrlich-Schwoebel barrier.

In addition, the evolution of surface morphology remains a crucial issue in the field of thin film deposition. It is necessary to understand the surface kinetics for improving the quality and smoothness of thin films. There are remaining crucial problems of growth and surface evolution that haven't been understood, even for systems that were investigated for many decades, such as GaAs. In previous related work Kan et al., and Tadayyon-Eslami et al. reported the surprising result [1.7, 1.8] that the corrugation of pits they built-in increases initially and eventual decays during epitaxial growth on GaAs(001). Important still unresolved questions in this system were: What drives this transient amplification of pattern corrugation? and what are the atomic-scale mechanisms that cause a reversal of the surface evolution modes , specifically transition from amplifying to decay?

Furthermore, the formation of mounds is an important feature that arises during growth, and a long disputed issue concerns the mechanism of forming mounds on GaAs(001) [1.9-1.12]. Does the formation of mounds come from the instabilities introduced by the Ehrlich-Schwoebel barrier or the roughness of the starting surface introduced by oxide removal techniques?

In chapter four, we investigate the surface evolution of nano-patterned GaAs(001), and we observe evidence for self-limiting growth that provides a key element in explaining the reversal of pattern amplification to pattern decay. We also report that reaching the critical terrace size of the top of each mound cause this self-limiting behavior. Most interestingly, we observe a sequence of sites of mound formation on patterned surfaces that give us new insights of the mechanism of formation of mounds.

1.2 Background

1.2.1 Epitaxy

Crystalline solids are known to be the stable form of most materials at low temperature under moderate pressure (with the exception of helium). The reason that many of the materials around us are not single-crystalline is that crystal growth is kinetically hindered. It is subject to barriers and instabilities which cause defects and finally polycrystalline or amorphous material. The technique of growth of single crystals is called "Epitaxy", from the Greek roots --- epi, meaning "above", and taxis, meaning "in ordered manner", which refers to the method of depositing a single crystalline film on a single crystalline substrate. The deposited film is denoted as a epitaxial film or epitaxial layer. Epitaxial films may be grown from vapor or liquid phases of materials, and because the substrate acts as a seed crystal, the deposited film takes on a lattice structure and orientation identical to those of the substrate.

Epitaxial films can be classified into two categories: homoepitaxy, for which the film is deposited on a substrate of the same composition as the substrate; and heteroepitaxy, for which the film is deposited on a substrate with other compositions of materials. Epitaxy is used widely in nanotechnology and in semiconductor fabrication, and it is the only affordable method of high quality crystal growth for many semiconductor materials, including technologically important materials as silicon-germanium, gallium nitride, gallium arsenide, indium phosphide and graphene.

1.2.2 Description of crystalline surface

Usually the substrate used for epitaxy is a single crystal, cut along a low Miller index plane, however it is always misoriented to some degree from the intended orientation. Usually wide terraces appear, divided by mono-atomic steps to compensate for the misorientation. (Misoriented Si(111) provides an exception to this, as it facets into flat regions separated by step bunches [1.13, 1.14]) An intentionally misoriented surface is called a vicinal surface, in contrast to an ideally atomically flat low index oriented surface. For a uniform vicinal surface, the distance between steps, called the terrace width L, depends only on the misorientation angle (α) and the step height (h):

$$h = L \times \tan\alpha \qquad \text{..... (1.1)}$$

Fig. 1.1 shows a TSK (Terrace Step Kink) model of crystalline surface originally proposed by Kossel and Stranski [1.15, 1.16], which describes the thermodynamics of

crystal surface formation and transformation, as well as the energetics of surface defect formation. The TSK model can be applied successfully to surface science topics such as crystal growth (including epitaxial growth), surface diffusion, surface roughening, and desorption.

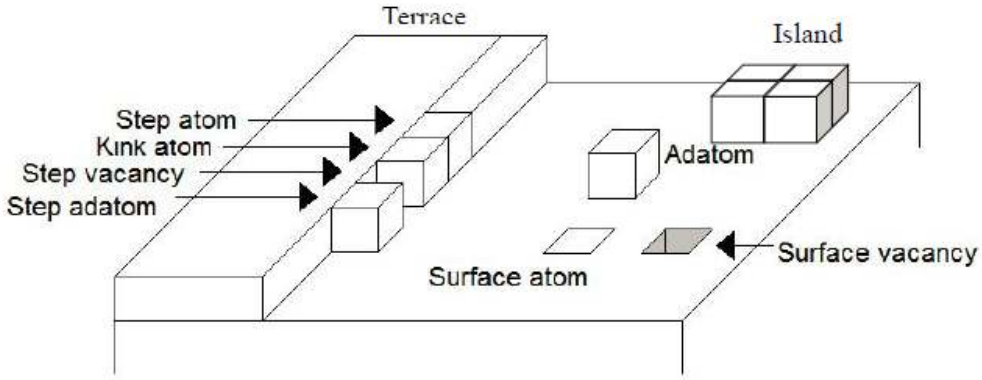

Fig. 1.1 *Schematic of TSK (Terrace-Step-Kink) model of crystalline surface*

1.2.3 Growth

Crystal and thin film growth occurs far from equilibrium and is a kinetic process where a high effective pressure is produced at the substrate to achieve condensation. The growth of crystal typically includes the following steps: 1) Adsorption of atoms

at the surface; 2) Diffusion of adatoms on the surface; 3) Incorporation into solid; 4) Desorption of adatoms from the surface, which competes with incorporation. The longer the adatom diffuses on the surface the higher the probability of desorption.

During growth adatoms arrive at the surface from the vapor, then they are absorbed by the surface and diffuse across the terraces until they are incorporated into solid by attaching to the existing step edges, islands, kink sites or vacancies or desorption. For those adatoms captured by vacancies or step edges, there is much less probability for them to escape due to bondings with near neighboring atoms, and the bonding strength is proportional to the number of nearest neighbors. Besides, the number of nearest neighbor sites of an adatom depends strongly on crystal symmetry and orientation of the surface. In addition, vacancies are very unlikely to be formed in great numbers during growth, because a relatively large number of atoms would need to be previously attached to other sites in exactly the right order. Thus, during growth on real surfaces vacancies appear only rarely and can be neglected.

1.2.4 Surface Diffusion

One of the most important parameters dictating the surface evolution of a film or a crystal is the kinetics of surface diffusion of adatoms. Diffusion on a solid surface is the motion of particles or adatoms on a discrete lattice. For a thermally activated surface diffusion process, the diffusivity of an adatom D can be expressed by the Einstein relation as shown in Eq. (1.2) where v *i*s the hopping rate of an adatom on a substrate and d is the dimension of the motion.

$$D = \frac{\nu}{2d} \qquad \text{..... (1.2)}$$

The diffusion hopping rate is the inverse of the average time needed for an adatom to jump from one site to another on the surface. D is often divided into a pre-factor D_0 and a Boltzmann factor as shown in Eq. (1.3)

$$D = D_o \exp(-\frac{E_d}{k_B T}) \qquad \text{..... (1.3)}$$

where D_0 is maximum diffusion constant, E_d is the activation energy that an adatom has to overcome for a hopping, k_B is Boltzmann's constant and T is absolute temperature. During deposition, a flux of atoms arrives at the growth front with a rate of F (in monolayers per second, or *ML/s*). Usually in MBE growth, the diffusion hopping rate is fast compared to the typical arrival rate from the flux, at typical growth rates of a 0.1~1 monolayer per second. Upon arrival an adatom diffuses on the surface till it meets another adatom to form a dimer, and the mean free path (diffusion length) of adatom diffusion is the mean distance on the surface that the monomer travels before it joins the surface (incorporation), or it leaves the surface (evaporation). In a kinetically limited growth scenario, the dimers are observed to be stable from a basic energetics point of view such that the critical nucleus size is i=2; for GaAs(001) under standard growth conditions this is thought to correspond to two Ga adatoms colliding in the presence of adsorbed As_2 [1.17]. Upon further deposition the number of dimers increases and becomes comparable to the density of monomers. Therefore, the chances of a monomer finding another monomer decreases, the growth rate of islands (trimers) competes with the growth rate of dimers, and further deposition contributes to island growth alone. At this saturation island density,

mean-field theory suggests that the mean free path of diffusing adatoms is equal to the mean island separation assuming that the monomer density outside the islands approaches the average value.

The mean free path, l , of adatoms relates closely with D and follows a power law as shown in Eq. 1.4 [1.18, 1.19]

$$l \propto (\frac{D}{F})^{1/6} \qquad \text{..... (1.4)}$$

The dependence of l on the ratio D/F ratio alone relates to the amount of time available for an adatom to diffuse before it encounters another adatom from the incoming flux, i.e., higher flux of deposition decreases the mean free path of adatoms. In Eq. (1.4) the diffusion coefficient D is a function of temperature according to Eq. (1.3), therefore, we can derive the temperature dependence of mean free path of adatoms from above equations; that the mean free path (diffusion length) increases exponentially with temperature.

For GaAs(001) during growth, both gallium and arsenic, in the form of As_2, diffuse on the surface [1.17]. Arsenic has much higher vapor pressure; thus up to a thousand times more arsenic than gallium is directed to the surface. Usually arsenic is present in excess, and under this condition, it is thought that the arrival and diffusion of gallium controls the growth [1.20]. However, as more arsenic is exposed to the surface, the probability for a diffusing gallium atom to form a bond to an arsenic molecule and to be incorporated is higher; therefore, the effect of changing the arsenic flux is definitely not negligible [1.20]. On the other hand, if more gallium is incorporated, fewer diffusing Ga atoms move on the surface, and the mean free path for diffusion increases.

1.2.5 Interlayer Transport - Effect of Ehrlich-Schwoebel Barrier

When diffusing adatoms move on the terrace, they will encounter an additional diffusion barrier when they approach descending step edges to impede adatoms cross step from above, indicated as E_S in Fig. 1.2, and this addition diffusion barrier, so called "Ehrlich-Schwoebel" barrier was first demonstrated experimentally by Ehrlich and Hudda in 1966 [1.21] through field ion microscopy. They observed diffusing

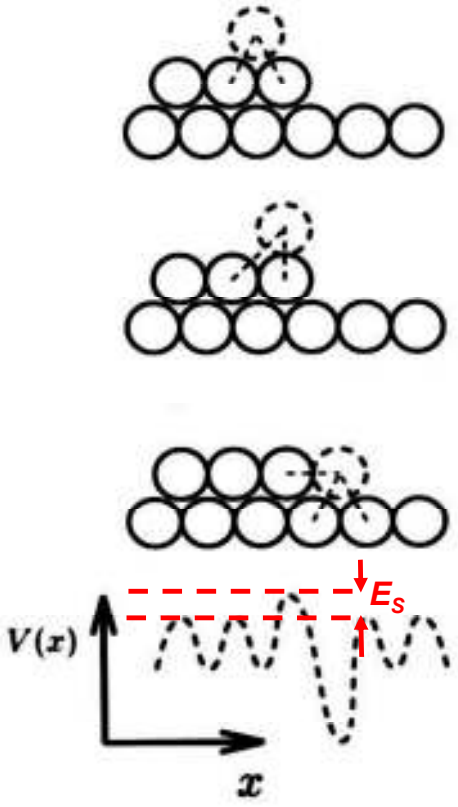

Fig. 1.2 *Schematic of the additional diffusion barrier at step edge (Ehrlich-Schwoebel barrier). It is rather unlikely for an adatom to cross the step atom from above due to increased hopping barrier.*

tungsten atoms on terraces which appeared to be repelled by descending terraces. Schwoebel and Shipsey interpreted this observation as due to a change in potential barrier for an adatom which diffuses across the step edge [1.22, 1.23]. As shown in Fig. 1.2, when an adatom crosses the step from above, it moves from a meta-stable state (top schematic, two bond countings) to an unstable state (intermediate schematic, one bond counting), which is unfavored.

If there is presence of the Ehrlich-Schwoebel barrier on crystal surface, the diffusing adatoms have lower possibility to move downward the steps and form a flat, two-dimensional film on surface, i.e. the interlayer transport between terraces is hindered. Instead, the presence of the Ehrlich-Schwoebel barrier will result in three-dimensional growth - formation of multilayer islands. Fig. 1.3 shows an example of the multilayer island formation during homoepitaxial growth with the presence of significant Ehrlich-Schwoebel barrier on Pt(111) surface [1.24, 1.34]. In Fig. 1.3, the existing steps direct the nucleation of new islands on top of the existing terraces, and result in wedding-cake shape of multilayer islands. So an interesting question would be: could we direct the formation of multilayer islands by building in artificial steps through patterning techniques with the effect of this kinetic barrier? This question has been investigated and reported in chapter three of this thesis.

The possible existence of this barrier on semiconductor surfaces is a very important but unresolved question. For example for elemental semiconductors, this barrier might be able to explain the roughening of Si(001) surfaces before it becomes amorphous. In the case of Ge(001) the barrier is found to be very weak [1.25]. For GaAs, Johnson et al. suggested that mound formation during growth might be due to

the existence of this barrier [1.9]. Finally even for the case where the Ehrlich-Schwoebel barrier is very weak, it has been proposed that a cooperative multistep Ehrlich-Schwoebel barrier for closely bunched steps might lead to observable effects [1.26].

Fig. 1.3 *STM images of formation of Pt multilayer islands on Pt(111) surface due to the presence of strong Ehrlich-Schwoebel barrier. After 37.1 ML of Pt deposited on top (Fig. 3 in Ref.[1.34])*

1.2.6 Growth Modes

The occurrence of individual epitaxial growth modes depends on various parameters of which the most important are the thermodynamic driving force and the misfit between substrate and layer. The growth mode characterizes the nucleation and growth process. There is a direct correspondence between the growth mode and the film morphology, which gives the structural properties such as perfection, flatness and interface abruptness of the layers. It is determined by the kinetics of the transport and diffusion processes on the surface. Different atomistic processes may occur on the surface during film growth: deposition, diffusion on terraces, nucleation on islands, nucleation of second-layer islands, diffusion to a lower terrace, attachment to an island, diffusion along a step edge.

Experimentally, the distinction between three classical growth modes is well known: Frank-van der Merwe (FV), Volmer-Weber (VW) and Stranski-Krastonov (SK). In addition to the three well-known epitaxial growth modes mentioned above, there are four distinct growth modes: step flow mode, columnar growth, step bunching, screw-island growth.

Frank-van der Merwe (FV) (Layer by Layer) Growth Mode

During FV or layer-by-layer growth mode, a new layer is nucleated only after completion of the layer below. This growth mode requires the diffusion length of adatoms smaller than the average terrace width, so that the growth is via island nucleation. In the idealized case in which interlayer transport is perfect, all the atoms arriving on the surface are incorporated at island borders. The optimum layer

homogeneity can be achieved by one dimensional movement of steps in FV mode initiated by a precise controlled small angle substrate misorientation.

Volmer-Weber (VW) (Island Nucleation) Growth Mode

A VW growth mode consists of large number of surface nuclei in first phase and consists of their spreading in second phase. Thus, VW growth often results in a high mosaicity of the material inside the layer. From the point of view of kinetics, it requires large terraces of the substrate, and adatoms arrive at the surface and diffuse around; nucleation happens when a sufficient number of adatoms meet each other. Islands grow by addition of further atoms until they coalesce. This process is similar to nucleation of a condensed phase from a supersaturated gas [1.27]. In this case, the interlayer transport is inhibited.

Stranski-Krastonov (SK) Growth Mode

SK mode is considered as intermediate between the FV and VW growth modes, and it is caused by significant lattice misfit from film and substrate. The lattice mismatch between the substrate and the film creates a build-in strain as a consequence of the increasing elastic energy with increasing layer thickness. The first deposited layer is atomically smooth (FV growth mode), compressively strained layer up to a certain thickness called the critical thickness. When the deposition time is enough to exceed the critical thickness – a grow mode transition to islands rapidly takes place (VW growth mode), because the nonuniform strain field can reduce the

strain energy by an island array, compared with a uniform flat film, resulting in the SK growth mechanism.

Step Flow Growth Mode

Step flow mode is clearly distinct from layer-by layer growth in FV mode. Surfaces usually have steps, which are preferred sites for incorporation of adatoms into the growing crystal. In step flow growth regime, the diffusion length of adatoms or the average island separation are much longer than the average terrace width, therefore, adatoms will be easily captured and incorporated by step edges [1.28]. The effect of preferred incorporation at steps is more pronounced if the steps are close together. This mode is often used to avoid island formation and island coalescence in epitaxy from the vapor phase.

1.2.7 Formation of Growth Mounds

When the interlayer transport of the atoms is inhibited, the growth leads to mound formation [1.20], and mound formation results in increased roughness of the surface. As has been mentioned above, the ease of movement of atoms between layers affects whether layer-by-layer growth or the formation of the mounds occurs.

In this section, we introduce mechanisms for the formation of growth mounds on GaAs surface. Certainly, one of the earliest and the most famous works that talked about the formation of mound on GaAs surface is by Johnson et al. [1.9]. In their work, they employed numerical simulation and molecular beam epitaxial

growth experiments to check the growth behavior on both vicinal (stepped) and singular (flat) starting surfaces. They concluded that in the presence of step-edge (Ehrlich-Schwoebel) barrier, the growth on singular surface is unstable and results in the formation of mounded structures with stable slope selection [1.29]. In contrast, the growth on a vicinal surface (the miscut above a certain critical slope, depending in the diffusivity of adatoms) is rather stable and leads to step-flow growth regime. From their observation, they proposed that the presence of Ehrlich-Schwoebel barrier destablize the singular surface toward to formation of mounds. However, a lower temperature oxide removal method was not applied in their experiment (e.g. applying atomic hydrogen source), there might be non-negligible roughness existing on the starting surface through removing the oxide thermally at 600 ℃ [1.30], and the roughness may affect further growth and bring in some complications during growth.

Theoretically, Politi et al. came up with the interpretation that the Ehrlich-Schwoebel barrier results in an instability toward mound formation on surface during growth [1.10, 1.11]. The growth instabilities were classified by Politi et. al. as follows: a) Diffusion instabilities: this kind of instability is typical for growth from solution or from melts. In the case of limited diffusion, atoms or molecules tend to stick to the nearest point of the solid, and dendrites form. b) Kinetic instabilities: these usually happen when the growth is fast compared to diffusion and the surface can not attain its equilibrium shape. c) Thermodynamic instabilities: these occur during the formation of thermodynamically unstable materials or during the heteroepitaxial growth with lattice mismatch. d) Geometric instabilities: an example

is shadowing, in which the geometry of the surface prevents stable and uniform growth.

A few years later, the Ballestad et al. [1.31] reexamined the question of instability toward mound formation, carrying out experiments similar to those done by Johnson et al., i.e. homoepitaxial growth on flat GaAs(001) surfaces. In this case

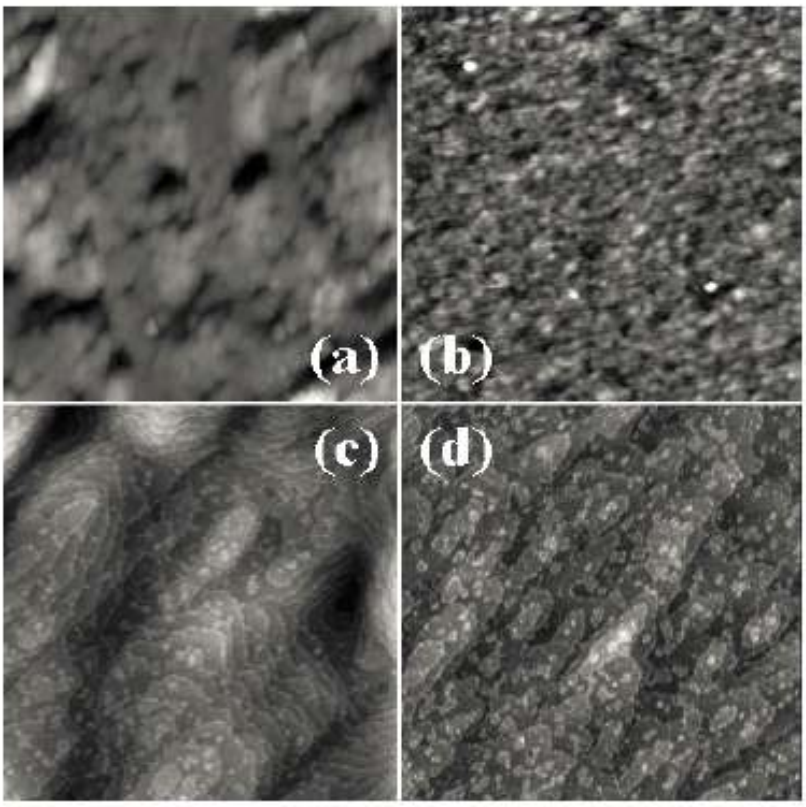

Fig. 1.4 *AFM images (all 2 μm x 2 μm) of GaAs surfaces after (a) thermal cleaning, (b) etching with atomic hydrogen, (c) growth on thermally cleaned substrate, and (d) growth on atomic H-etched substrate. Grayscales are (a) 30 nm, (b) 2.5 nm, (c) 4 nm, and (d) 2.5 nm. (Fig. 3 in Ref. [1.31])*

they compared the results of thermal desorption of the oxide layer at 600 ℃ with a process using atomic hydrogen at lower temperature of 300 ℃ ~ 400 ℃, which the latter method minimizes the initial roughness of starting GaAs(001) surface by approximately an order of magnitude [1.30]. Their results are reproduced in Fig. 1.4, and indicate that no mounding indicative of unstable growth was observed in the films cleaned with atomic hydrogen and suggest that homoepitaxial growth on flat GaAs is stable, and that the mounds commonly attributed to growth instabilities are in fact due to the initial roughness of the oxide-desorbed GaAs surface.

More recently, Tadayyon-Eslami et al. reported the formation of mounds around micron size pits she patterned on GaAs(001) surface for growth at temperatures below ~540 ℃, with the mounds selectively decorating certain edges of pits, i.e. running perpendicular to [110] crystal orientation of GaAs. This result is shown in Fig. 1.5. Tadayyon-Eslami et al. interpreted this as evidence of the existence of a small, aniostropic Ehrlich-Schwoebel barrier on GaAs(001) surface [1.8]. In this thesis we reexamine this interpretation and present evidence that, instead, heterogeneous nucleation of mounds, rather than instability associated with the Ehrlich-Schwoebel barrier, explains this observation.

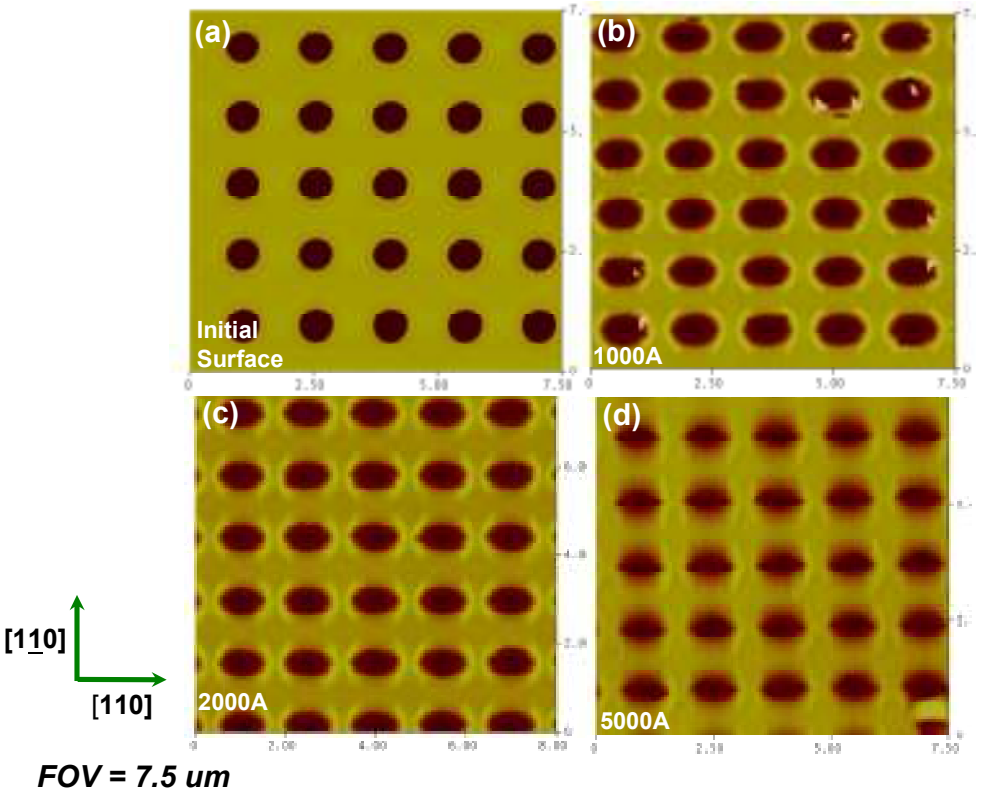

Fig. 1.5 *Selective formation of mounds around pits along [110] orientation during homoepitaxial growth at temperature of 540℃. The growth thickness is (a) 0 nm; (b)100 nm; (c) 200 nm; (d) 500nm. The pit size is 0.7 μ m and the spacing between pits is 1.4 μ m (Reproduced figure from ref. [1.30])*

1.2.8 Reflection High Energy Electron Diffraction (RHEED)

Reflection High-Energy Electron Diffraction (RHEED) is a versatile analytical tool for characterizing thin films during growth by molecular beam epitaxy, since it is very sensitive to surface structure and morphology; it is particularly sensitive to surface roughness, down to monolayer sensitivity. An accelerated incident electron beam with high energy (5-100 keV) is incident on the surface with very small angle (< 3 degree). Although energetic electrons can penetrate deeply into materials, the glancing incident angle makes this technique very sensitive to the surface [1.32], and the sample region is typically only a few atomic layers into the material. Fig. 1.6 shows the geometry employed in the RHEED [1.33]. Upon reflection, electrons interfere and form a diffraction pattern. The diffraction pattern is determined by the surface morphology and the atomic structure of the surface. A perfectly flat surface will result in a RHEED pattern which consists of the intersection of reciprocal lattice rods with the Ewald sphere, i.e. streaks. The RHEED techniques also allows us to monitor the growth rate of layers of atoms on the surface by analysing the periodic variations of the RHEED intensity during growth, this is so called RHEED oscillations. Besides, by knowing both the distance from the sample to the screen or recording medium and the energy of the electron source, it is possible to calculate the lattice spacings of the sample through RHEED patterns.

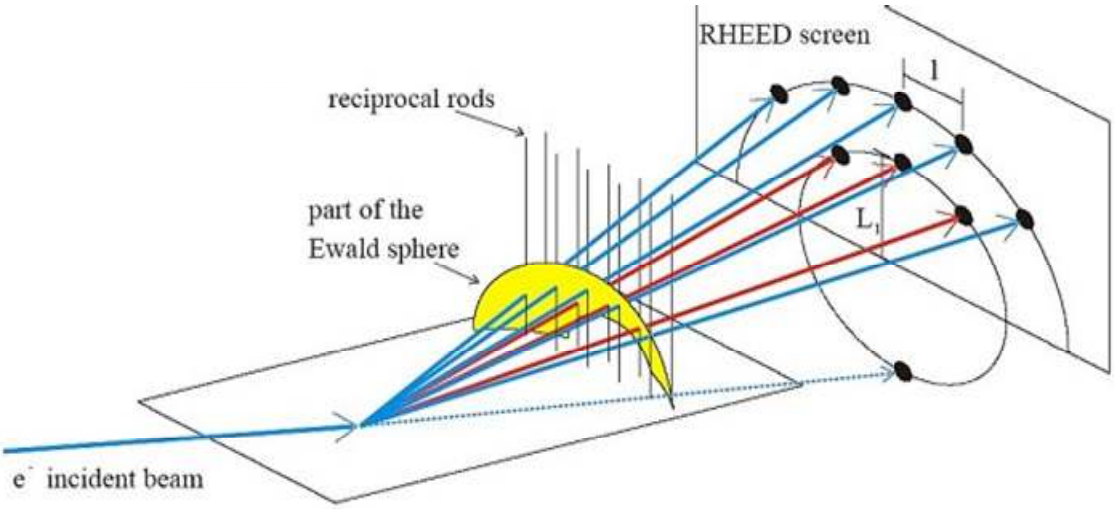

Fig. 1.6 *Schematic of RHEED. A glancing angle is used between incident beam and the sample that allows us to obtain the information for only few layers of surface atoms*

Chapter 2

Experimental and Simulation Procedures

In this chapter, we describe the techniques employed in the investigation of surface evolution and directing self-assembly of nanostructures during growth on patterned substrates which form the major part of this thesis from both experimental and numerical simulation aspects. In order to make direct comparisons between experiments and atomistic calculations, it is desirable to fabricate our patterns within nanometer, rather than micron, scale due to limitations in computational power.

First, we introduce the techniques required for nano-pattern fabrication, crystal growth and characterization from the experimental aspect. Then, we will introduce the idea of kinetic Monte Carlo (kMC) simulation, which we used in our atomistic numerical calculations in order to understand the effect of kinetic parameters on surface evolution and nanostructure formation during growth.

2.1 Growth Experiments on Patterned GaAs(001)

2.1.1 Fabrication of Nanopatterns

We create periodic, square arrays of square nanopits using electron beam lithography on GaAs(001) substrates. The n-type GaAs wafers used in these experiments were two inches in diameter with thickness of 500 $\pm$ 25 μm and surface orientation of (001) $\pm$ 0.5^{o}, supplied by American Crystal Technology (AXT). A summary of patterning process is show in Fig. 2.1.

All the processes described below have been carried out in a class 10 cleanroom to minimize the presence of particles on the surface. Impurity clusters act as nucleation centers for growth of rough structures or pinning of the steps during growth, which significantly affect the evolution of surface morphology. We have taken special care to remove all residues of the e-beam resist from the patterned surfaces, using multiple cycles of solvent rinses and oxygen plasma etching. We examined the results by scanning the surfaces with AFM after each cycle to judge the results. This is repeated until all detectable resist has been removed.

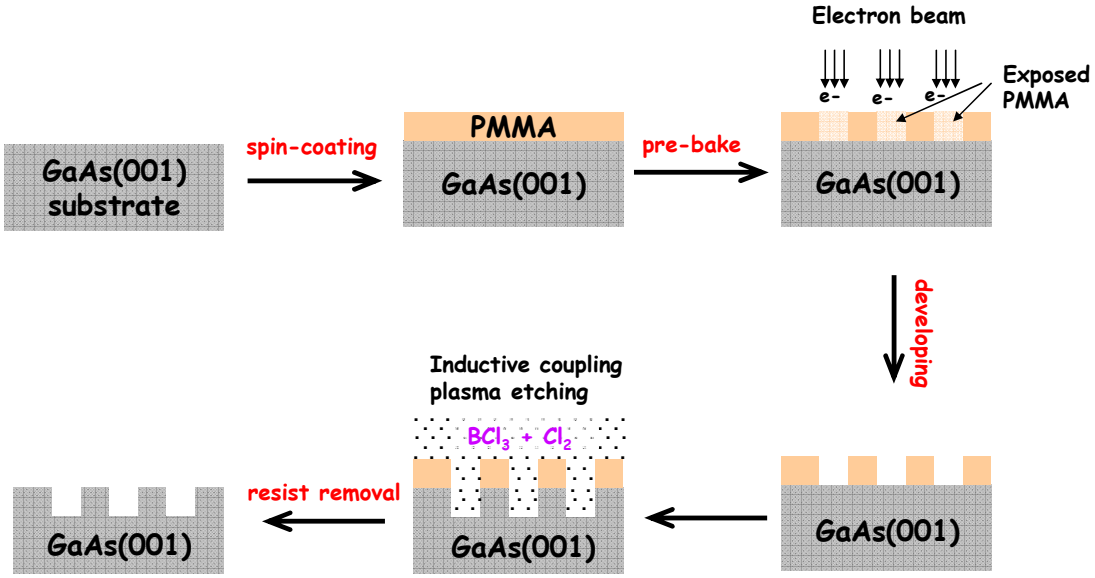

Fig. 2.1 *Schematic of processes of nano-pattern fabrication on GaAs(001) substrates by electron beam lithography and plasma etching techniques.*

2.1.1.1 Electron Beam Lithography (EBL)

We choose commercial Poly-methyl methacrylate (PMMA) fabricated by MICROCHEM as our electron-beam resist [2.1], which is a positive resist, i.e. the regions of PMMA exposed to the electron beam are damaged (chain scission) and can be subsequently removed during a developing process. PMMA is a versatile polymeric material that is well suited for many imaging and non-imaging microelectronic applications, and it is also the most commonly used as a high resolution positive resist for direct write e-beam as well as x-ray and deep UV microlithographic processes. Standard PMMA products cover a wide range of film thickness and are formulated with 495,000 and 950,000 molecular weight (MW)

resins in either chlorobenzene or the safer solvent anisole. The PMMA we use is 950 PMMA A4, which means we have PMMA with 950,000 molecular weight, and the concentration of PMMA is 4% dissolved in solvent anisole.

We first deposited several drops of PMMA on the wafer with a disposable pipette, and the wafer was then spun at 5000 rpm for 60 seconds with the ramp speed 500 rpm/sec to speed up and down. This spinning rate creates a fairly uniform film of PMMA with thickness of ~200 nm on top of the wafer. The wafer was then put on a hot plate and pre-baked at 180 °C for 5 minutes to harden the PMMA and to enhance its adhesion to the wafer.

The system we used is a field emission scanning electron microscope (SEM, JEOL JSM-6500F), which has been modified for electron beam lithography control (Nabity), which allows us to fabricate nanostructures at least down to 50 nm. We optimize the size and spacing of fabricated patterns to fit the nominal values by refining the dosages of electron beams. Typically, we varied the dosages from 400~900 $\mu C/cm^2$. We then transferred the pattern to the substrate by inductive coupling plasma etching, removed the resist and measured the pit topography by carbon nanotube terminated tips with atomic force microscopy (AFM).

After exposing the resist, we transferred the wafers into resist developer: 1:3 MIBK (methyl isobutyl ketone) to IPA (isopropyl alcohol). The exposed PMMA was removed by immersing into resist developer for 20 seconds with slightly shaking. The wafers were then rinsed with IPA for another 40 seconds to remove the residues of the developer, and then blown dry with dry nitrogen. Furthermore, we also used short 15 second oxygen plasma exposures to remove the residues of PMMA in the

trenches of patterns, in order to control the uniformity of pattern transfer in the next etching step. At this point, we also characterized the patterned PMMA film by optical microscopy to check if the processes above were successful..

2.1.1.2 Inductive Coupling Plasma (ICP) Etching

The next step in the patterned substrate fabrication process is transferring the pattern to the substrate using inductive coupling plasma etching. We chose a dry etching method which allows for anisotropic etching, resulting in pits with nearly vertical side walls. The etching was done in a Plasmatherm SLR ICP system. The operating parameters for the process are given in table 2.1.

BCl_3 Gas	12.5 sccm
Cl_2 Gas	2.5 sccm
He Gas	4.0 sccm
Pressure	4.0 mTorr
RF 1 Power	60 W
RF 2 Power	100 W
DC Voltage	310 V
Etching Time	25~40 sec

Table 2.1 Parameters used for etching GaAs(001) in Inductive Coupling Plasma (ICP) etching system.

With our etching condition, the etching rate for GaAs(001) is about 1 nm/sec. This condition reduces our total etching time to within a minute for fabricating 20 - 50 nm depth nanopit arrays; this short etching time is advantageous to avoid overheating the substrate that will harden the PMMA and make it hard to be removed from the substrate.

2.1.1.3 Sample Cleaning and Characterization

After transferring the pattern to the substrate via ICP, we dissolved the resist with acetone, while agitating in an ultrasonic bath for 30 minutes. We then immersed the wafer in boiling (~80 ºC) n-methyl-2-pyrrolidone (NMP) for 60 minutes. The wafer was next rinsed with a series of solvents: acetone, methanol, and isopropyl alcohol. Finally, we rinsed the wafer with flowing deionized (DI) water, and then dried the wafer using a jet of dry nitrogen gas. Repeating the solvent cleaning process described above does not completely remove these residues. We found that in order to remove the residual resist completely, it was necessary to subject the wafers to oxygen plasma cleaning for another 10 minutes after solvent cleaning.

It is very important to fully remove the PMMA on the patterned substrate; otherwise, the residues will strongly affect the growth results by molecular beam epitaxy. Therefore, we carefully characterized the patterned surface by AFM and particular checked if we see clear pit edges, which are the places PMMA residues stay mostly. If residues of PMMA was detected, we further run a few cycles of the solvent rinsing and the oxygen plasma etching in order to remove all residues to beneath the detectable limit by AFM imaging.

2.1.1.4 Pattern Design

In order to use a model containing atomic-scale processes to understand the growth behavior, we decided to make nano-scale patterns. We first fabricated a series of square-nanopit arrays, varying the initial pit width, including widths of 60 nm, 80 nm, 100 nm, 140 nm, 200 nm, 280 nm and 400 nm. In all cases, we fixed the ratio of the initial width to pitch (center-to-center spacing) to be 1: 2, and fabricated a finite size of 20 x 20 squared-nanopits in each array, and this allows us to compare the growth behavior between the patterned region and the unpatterned part of the surface. Fig. 2.2 shows examples of AFM images of nano-patterned GaAs(001) substrates with varying initial pit widths.

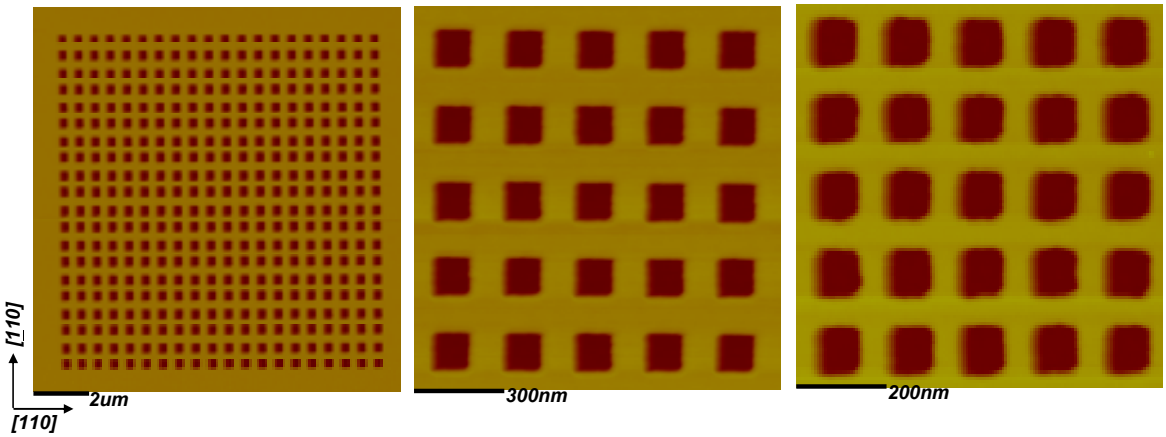

Fig. 2.2 *AFM images of squared-nanopit arrays made by electron beam lithography and plasma etching techniques on GaAs(001) substrates. The width of nanopits varies from 60 nm to 400 nm, and the depth of nanopit is approximately 50 nm.*

Device fabrication with architectures containing various geometries and designs typically involves lots of pattern transfer. Therefore both from scientific and technological points of view, we were curious about how shapes of the patterns affect the growth or the thin film deposition. In order to address this question, we fabricated nanogrooved pattern on GaAs(001) substrate by varying its length/width aspect ratio of patterns from 1:1000 to 1000:1, in which the two orthogonal edges of the patterns are along [110] and [$\underline{1}$10] crystal orientations. Examples of scanning electron microscopy images of nanogrooves are shown in Fig.2.3. (The results of growth of nanogrooved patterns are described in Appendix A)

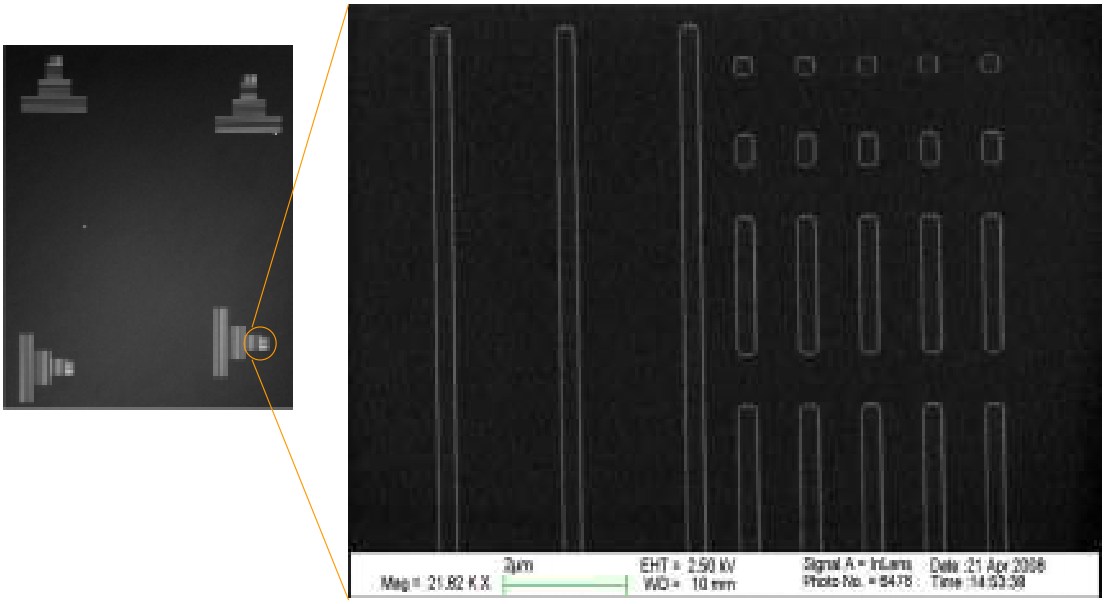

Fig. 2.3 *SEM images of nanogrooves on GaAs(001) substrates. The width of this set of nanogrooves is 200 nm, the depth is approximately 20 nm, and the ratio of length to width of nanogrooves varies up to 200:1, corresponding to a 40 μm long grooves.*

2.1.2 Molecular Beam Epitaxy (MBE)

Molecular Beam Epitaxy (MBE) is an Ultra High Vacuum (UHV)-based technique for producing high quality epitaxial structures with monolayer (ML) control. Since its introduction in the 1970s as a tool for growing high-purity III-V semiconductor films, MBE has evolved into one of the most widely used techniques for producing epitaxial layers of metals, insulators, and superconductors as well, both at the research and the industrial production level. The principle underlying MBE growth is relatively simple: it consists essentially of atoms or clusters of atoms, which are produced by heating up a solid source. They then migrate in an UHV environment and impinge on a hot substrate surface, where they can diffuse and eventually incorporate into the growing film. Despite the conceptual simplicity, a great technological effort is required to produce systems that yield the desired quality in terms of material purity, uniformity and interface control [2.2]. In this section, we further describe the procedures used in the final surface preparation and in MBE growth in our growth experiments.

2.1.2.1 Pre-Loading Preparation

Prior to loading a wafer into the MBE system one final series of solvent rinses was performed. This consisted of a sequence of rinses, 3 minutes each, while agitating in an ultrasonic cleaner. The sequence of solvent was trichloroethylene (TCE) followed by acetone, methanol and isopropyl alcohol: A clean beaker used for each step. The sample was then rinsed with flowing DI water and then blown dry with N2.

2.1.2.2 MBE Growth Stations

Our MBE growth was done in a commercially available MBE growth systems, which is a VG-80H MBE system with the capability for growing compounds based on Ga, Al, As, N and Sb; also with in situ atomic hydrogen source, reflection high energy electron diffraction (RHEED), and residual gas analysis diagnostics. The schematic of the MBE system is shown in Fig. 2.4.

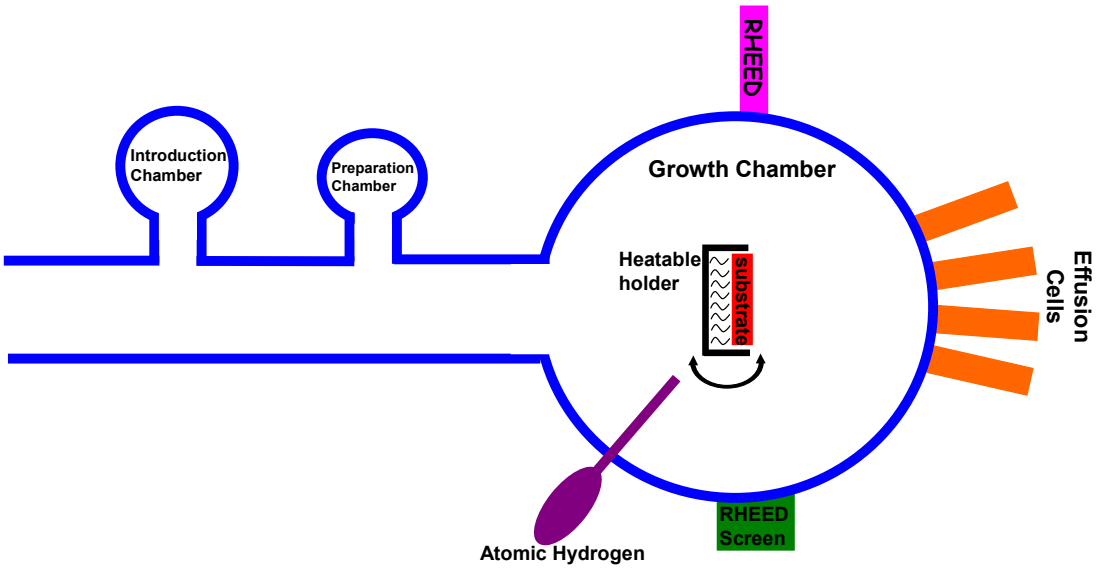

Fig. 2.4 *Schematic of the MBE system we used in our experiment. The system is equipped with RHEED and atomic hydrogen source.*

After solvent rinsing, the sample was loaded into the introduction chamber of the MBE system through a load-lock system, and degassed for 12 hrs at 180 ºC at a background pressure of approximately 10^{-11} torr. Next, the sample was transferred into the preparation chamber ($P = 10^{-11}$ torr) where the second stage of degassing of the sample was carried out, typically for 30 minutes at 400 ºC.

Prior to growth, the beam equivalent pressures (BEP) of the As_2 flux and the Ga flux from the effusion cells were measured using an ion gauge located in the growth chamber; this was done while the sample was still in the preparation chamber. Once both the As_2 flux and Ga flux were calibrated to the desired settings, the sample was then transferred to the growth chamber for growth. For the growth, As_2 flux was used in excess so the growth rate was controlled by the Ga flux.

2.1.2.3 Oxide Removal

In order to get epitaxial growth on GaAs(001) substrate, the native oxide on the substrate must be removed. This can be done in two ways, desorption by heating to ~582 °C or desorption while heating to ~400 °C in the presence of atomic hydrogen. [2.14, 2.15] In our experiments we desorbed the oxide layer with the presence of atomic hydrogen to minimize the surface roughness due to heating. Desorption of the oxide was monitored using RHEED and as the oxide was removed, the RHEED pattern turns from hazy background to diffraction streaks, which is characteristic of crystalline surface reconstruction of GaAs(001) surface. Fig. 2.5 shows examples of

our RHEED patterns for a GaAs(001) surface before and after removing the oxide layer for the electron beam incident along the [$\bar{1}$10] azimuths.

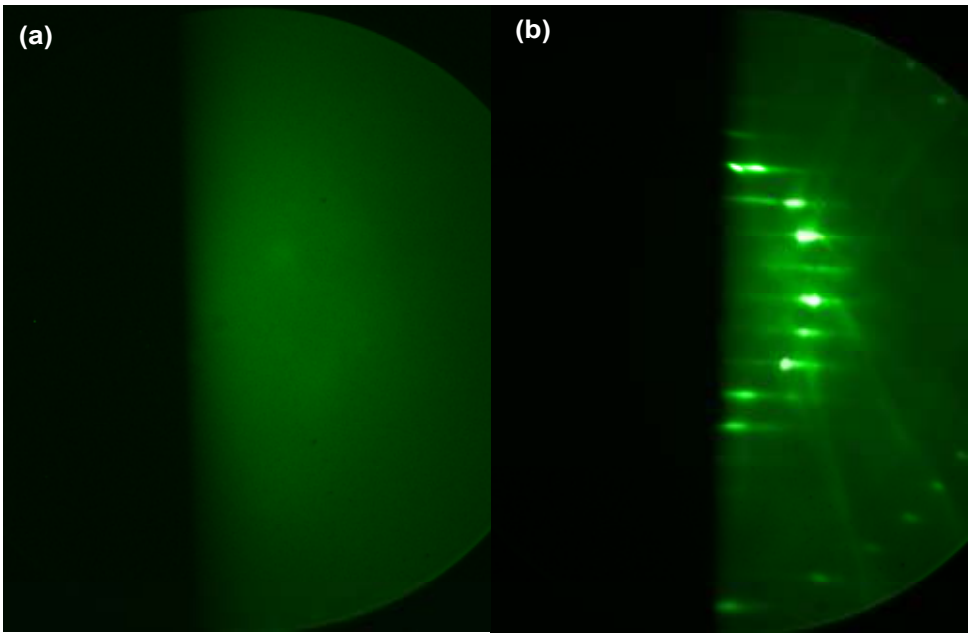

Fig. 2.5 *RHEED patterns for GaAs(001) surfaces along [$\bar{1}$10] crystal orientation; (a) before deoxidization with atomic hydrogen source; (b) after deoxidization with atomic hydrogen for 3 hours at 400℃.*

Removing the oxide in the presence of atomic hydrogen gives us a rather smooth starting surface with RMS roughness of 0.15 nm measured by ex-situ atomic force microscopy. On the contrary, the deoxidized surface prepared by heating up to 582 °C will result in a rougher surface, which has the RMS roughness about 1 nm [2.3]. The reducing roughness of starting surface prepared by atomic hydrogen further reduced the possibilities for heterogeneous nucleation of mounds that lead us to the new

understanding of the mechanism of mound formation and will be discussed in Chapter 4.

2.1.2.4 Growth Experiments and Surface Reconstructions

In the work described in this thesis, we carried out homoepitaxial growth of GaAs on patterned GaAs(001) substrates. The patterning on the substrate acts as a probe to realize the effect of kinetic barrier on GaAs(001) surface and to understand the mechanisms of crystal growth and mound formation on surfaces.

Patterned samples were cycled between a molecular beam epitaxy (MBE) growth chamber (base pressure 2 x 10^{-11} mbar) for homoepitaxial growth and an atomic force microscope (AFM) for surface topography determination in atmosphere. Before each growth experiment the surface oxide was desorbed by heating to 400 ℃ in the presence of atomic hydrogen, producing negligible desorption induced roughness. The growth was performed in the excess of As_2 flux with beam equivalent pressure (BEP) of 7.5 x 10^{-6} torr, and we set the BEP ratio for As_2 : Ga is 10:1 that the BEP for Ga flux is about 7.5 x 10^{-7} torr. The opening of valve for Ga flux determines the onset of GaAs growth on the substrate, and the growth rate was held fixed at 0.28 nm/s. In this research, we did our growth experiments mainly at temperatures of 460 °C and 525 °C.

We used reflection high energy electron diffraction (RHEED) to monitor our surface reconstructions after de-oxidization. In Fig 2.6 (a) and (b), we show the RHEED patterns along [010] and [$\underline{1}$10] crystal orientations, respectively, of the

surfaces heated at 525 °C. The existing "4x" peaks (1/4 beam) along [010] orientation, and "2x" peaks (1/2 beam) along [$\underline{1}$10] orientation are the characteristic of a c(4x4) surface reconstruction of GaAs(001). In Fig. 2.6 (c) and (d) show the RHEED patterns along [110] and [$\underline{1}$10] crystal orientations of the surfaces heated at 580 °C. Evidently, the "2x" peaks (1/2 beam) along [110] orientation, and "4x" peaks (1/4 beam) along [$\underline{1}$10] orientation are the characteristic of β_2-(2x4) surface reconstruction of GaAs(001) [2.3, 2.4]. Clearly, we see a surface reconstruction phase transformation between growth temperatures 525 °C and 580 °C.

Therefore, in order to know the starting microscopic conditions of the initial surface we are dealing with, we carefully check the surface reconstructions of GaAs(001) over a range of growth temperatures, which is show in Fig. 2.7. By tracking the RHEED patterns taken along [$\underline{1}$10] orientation, we see a transition from showing prominent "2x" peaks to "4x" peaks as we increase the temperature, which indicates a phase transition from c(4x4) to β_2-(2x4) surface reconstructions at 557 °C. Consequently, the growth experiments reported in the thesis are at the temperatures below this phase transition, which are at the c(4x4) reconstruction regime.

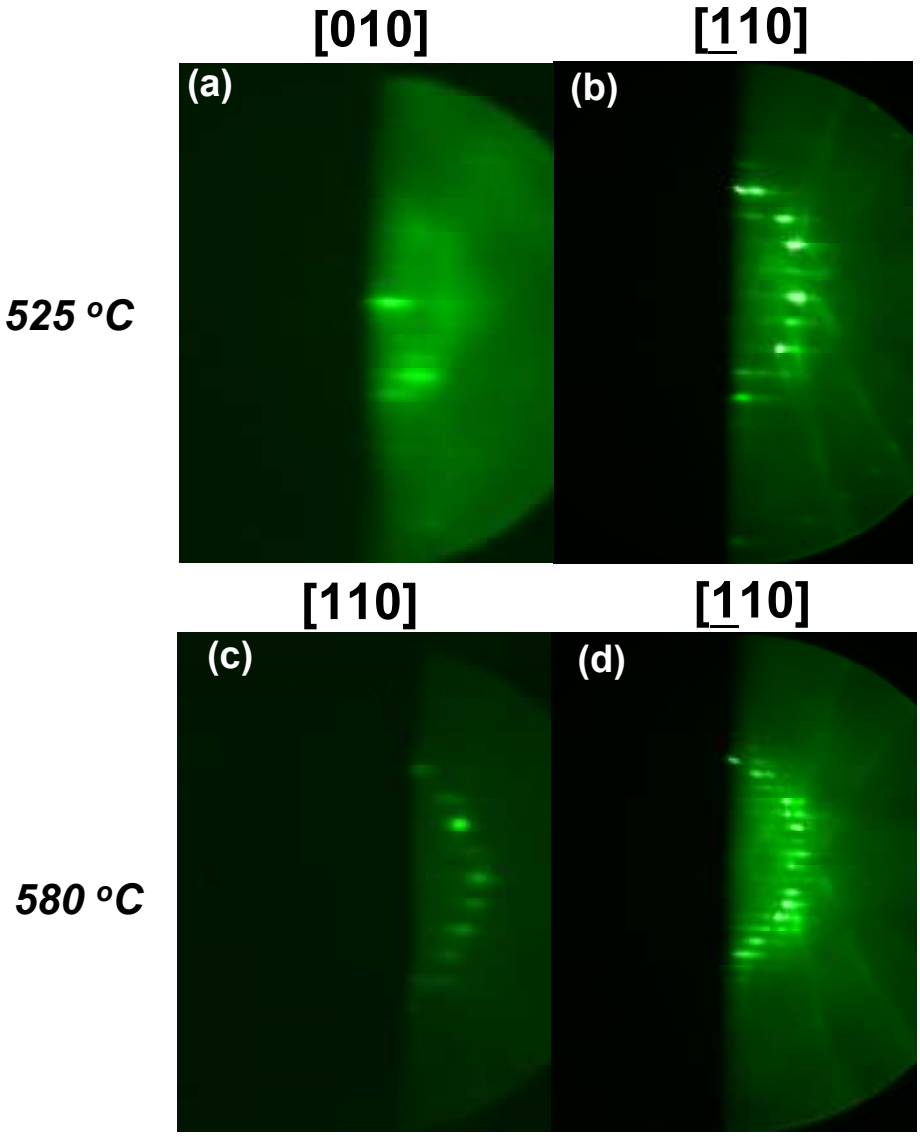

Fig. 2.6 *RHEED patterns for GaAs(001) surfaces at (a) 525 °C along [010] crystal orientation; (b) 525 °C along [1̄10] orientation; (c) 580 °C along [110] orientation; and (d) 580 °C along [1̄10] orientation after deoxidization with atomic hydrogen for 3 hours at 400℃. The RHEED patterns indicate a phase transition at the temperature between 525℃ and 580 ℃.*

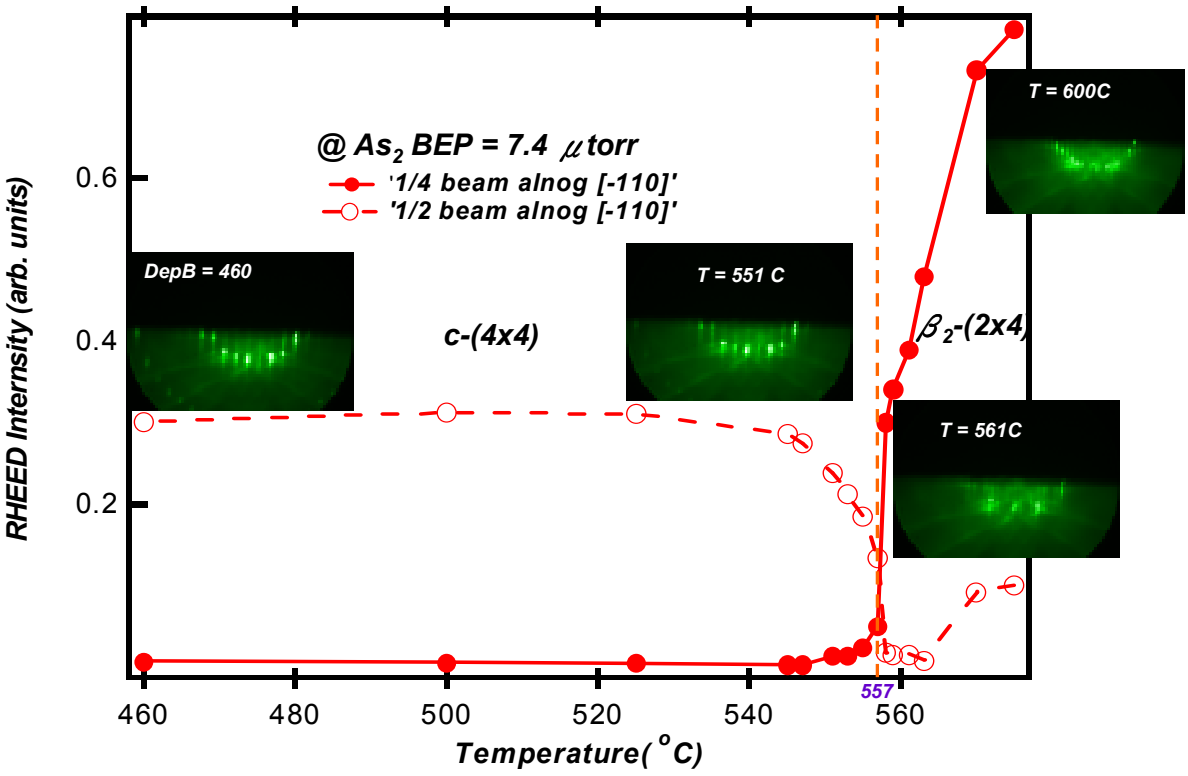

Fig. 2.7 *Peak intensity analysis of RHEED patterns taken along [1̲10] crystal orientation vs. growth temperatures for GaAs(001) surface. We observe a phase transition at 557 °C*

2.1.3 Characterization

We use atomic force microscopy (AFM) for ex-situ characterization of the grown surfaces after they were taken out from the vacuum chamber. Typically for rather flat surfaces, silicon AFM tip with pyramid-shape is frequently used for tapping mode scanning. However, due to the narrow and deep nanoscale patterns we made on the substrates, regular pyramid-shape tip will result in strong convolution with the patterns and not image the shape of patterns correctly. Therefore, we adopt commercially available carbon nanotube (CNT) terminated AFM tips [2.5] whose terminal radii were nominally between 10 nm and 30 nm to characterize the patterned surfaces; these resolve the pit edges and bottoms in the range of pattern sizes used in our experiments. Scanning electron microscopy (SEM) was also used in characterizing the lateral dimensions of the grown substrates. However, we found that the characterized areas by SEM show differences in growth topography for cycled substrates; this may be due to the carbon contamination from SEM or the charging effect of the substrates. Thus we used SEM to characterize the surfaces only at the final stage, i.e. beyond which no further growth was planned.

2.2 Kinetic Monte Carlo (kMC) Simulation Method

2.2.1 Brief Review of kMC

Monte Carlo simulation refers to a broad class of algorithms that solve problems through the use of random numbers, and the name means just what it sounds like, referring to the random nature of the gambling at Monte Carlo, Monaco. The most famous of the Monte Carlo methods is the Metropolis algorithm [2.6, 2.7], invented over 50 years ago at Los Alamos National Laboratory. Metropolis Monte Carlo is accomplished through surprisingly simple rules, involving almost nothing more than moving one atom at a time by a small random displacement. This algorithm and the numerous methods built on it are at the heart of many of the simulations studies of equilibrium properties of physical systems.

In the 1960's researchers began to develop a different kind of Monte Carlo algorithm for evolving systems dynamically from state to state. The earliest application of this approach for an atomistic system may have been demonstrated by Beeler with the simulation of radiation damage annealing [2.8]. In the 1990's the terminology for this approach settled in as kinetic Monte Carlo, though the early papers typically use the term of "dynamic Monte Carlo" [2.9]. The popularity and range of applications of kinetic Monte Carlo (kMC) has continued to grow, and kMC is now a common tool for studying materials subjects. A questionable issue with kMC is whether it can, in principle, give the exact dynamical evolution of a system. Although this ideal is virtually never achieved, and usually not even attempted, the kMC method is presented here from this point of view because it simplifies the real system with computational models and makes a good framework for understanding

what is possible with kMC, what the approximations are in a typical implementation, and how they might be improved.

Why use kMC method or perhaps equivalently, what is the benefit of using kMC? In particular, in computational materials science molecular dynamics (MD) simulations exist that allow one to follow the dynamics of molecular processes in great detail. In particular, the combination of MD simulations with density functional theory (DFT) calculations of the electronic structure has brought us a great step further; since DFT enables us to describe a wide class of chemical bonds with good accuracy, it has become possible to model the microscopic dynamics in

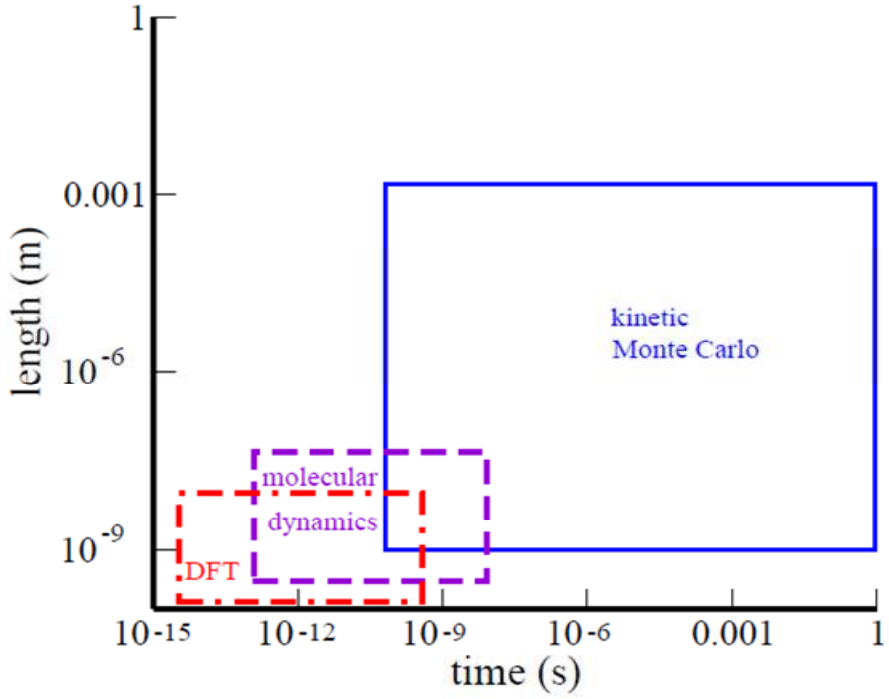

Fig. 2.8 *Typical length and time scales associate with computational methods. KMC can reach much larger scale than MD and DFT. (Fig.1 in [2.10])*

materials. Hence any simulation that aims at predictive power should start from the sub-atomic scale of the electronic many-particle problem. However, for many questions of scientific or technological relevance, the phenomena of interest take place on much larger length and time scales. This "time-scale problem" brings up the limitation of DFT and MD calculations as shown in Fig. 2.8. Kinetic Monte Carlo attempts to overcome this limitation by exploiting the fact that the long-time dynamics of this kind of system typically consists of diffusive jumps from state to state. Rather than following the trajectory through every period, these state-to-state transitions are treated directly. The result is that can reach vastly longer time scales, and can be applied to tackle with complex many-particle systems [2.10].

2.2.2 KMC Model in this Work

Our kinetic Monte Carlo simulations are carried out using a Fortran-based code developed by our collaborator Ajmi Ben Haj Hammouda [2.11,2.12]. It uses a standard solid-on-solid (SOS) description of the growth of a simple cubic crystal. The SOS model assigns an integer height , measured above the average vicinal plane, to each point on a square grid of dimensions 500a x 500a, where a is the lattice constant. We use periodic boundary conditions in both directions.

The microscopic processes considered are the deposition of atoms with an incident flux F and diffusion; desorption is not considered. In most of the results reported above we fixed the incoming flux at a value corresponding to the arrival of 1 monolayer of atoms per second. Absorbed adatoms hop from site to site in the

presence of three energetic barriers: the diffusion barrier, E_d, the in-plane nearest neighbor interaction barrier, E_a and in order to probe the effect of Ehrlich-Schwoebel (ES) barrier on semiconductor surface directly, we build the Ehrlich-Schwoebel barrier, E_{ES}, at step edges in our kMC calculation. The schematics of a microscopic view of diffusing adatoms associated with these energetic barriers is shown in Fig. 2.9.

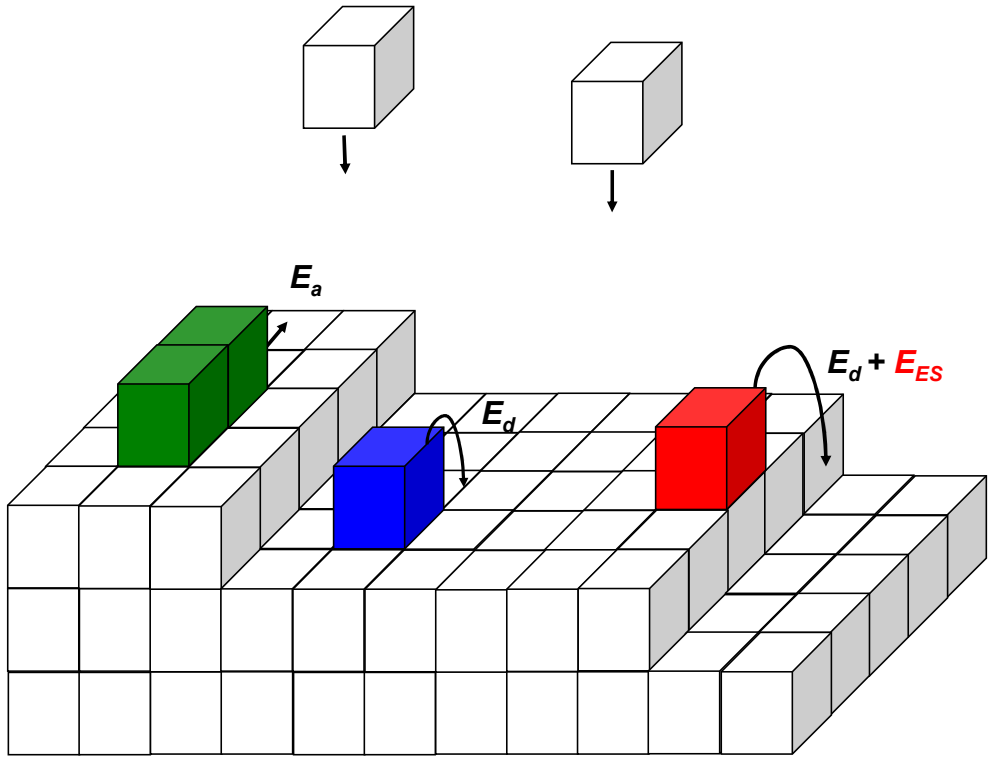

Fig. 2.9 *Schematics of solid on solid (SOS) model built in our kMC model with presence of three energetic barriers: the diffusion barrier, E_d, the in-plane nearest neighbor interaction barrier, E_a and the Ehrlich-Schwoebel (ES) barrier, E_{ES}.*

The overall barrier to hopping is

$$\boldsymbol{E_X = E_d + nE_a + \eta E_{ES}} \qquad \text{.....(2.1)}$$

Here n is the number of nearest neighbor adatoms with which a diffusing atom interacts; it ranges from 0 to 3, as atoms with 4 neighbors are immobile. η is equal to 1 if there is an Ehrlich-Schwoebel barrier for a particular hop, and 0 otherwise. The hopping frequency follows an Arrhenius form with a rate:

$$\Gamma = \nu_0 \exp\left(-E_X / k_B T\right) \qquad \text{.....(2.2)}$$

where ν_0=10^{13} Hz is a typical adatom vibration frequency, T is the substrate temperature, and k_B is Boltzmann's constant. We use values for the diffusion barrier and the in-plane nearest neighbor interaction barrier typical of those calculated by first principle calculations [2.13], and vary E_{ES}. In the simple model used here no preferential diffusion along step edges is considered. However, it is good enough to qualitatively demonstrate the effect of Ehrlich-Schwoebel barrier during growth on a patterned surface.

The initial simulations start with a surface shown in Fig. 2.10, containing a square array of flat-bottomed square pits, each of width 50 lattice constants wide and with a center-to-center spacing of 100 lattice constants. We start with pits 10 lattice constants deep, bounded by side walls, which form angles of 45° with respect to the surrounding surface. However, in our later simulations, we also treat the width,

depth and slope of side walls as changing parameters to determine how these pattern parameters affect the growth and surface evolution.

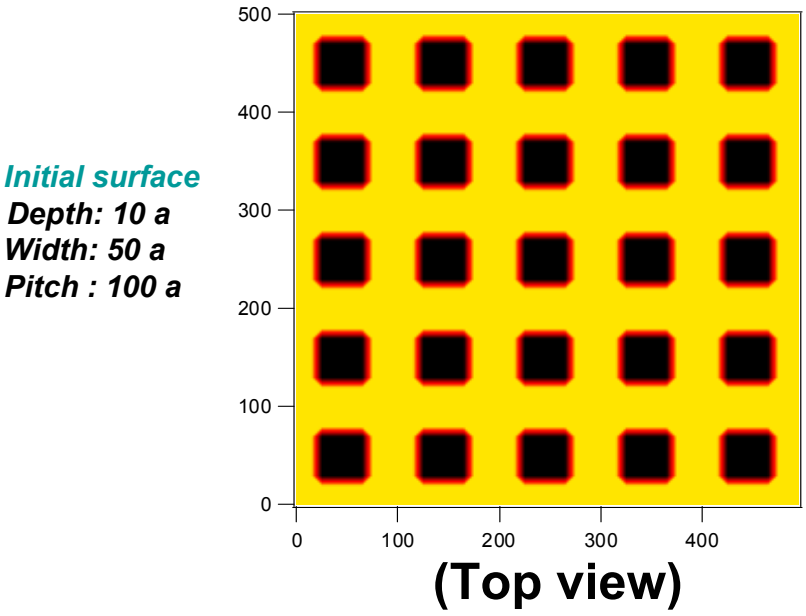

Fig. 2.10 *In our kMC simulations, we build in periodic patterns on the surface as our starting surface.*

Chapter 3

Kinetic Monte Carlo Study of Directing Self-Assembly of Nanostructures on Patterned Crystal Surface during Homoepitaxial Growth

A means of fast assembly of extremely large numbers of nanostructures with positional and size control will be required if technology is to keep pace with the ever decreasing size scale of devices called for by such timetables as Moore's Law [3.1] and the international technology roadmap for semiconductors [3.2]. Directed self-assembly [3.3], in which a template influences the otherwise spontaneous arrangement of atoms during processes such as growth [3.4-3.18] is an appealing candidate for achieving this. Mechanisms by which templates influence control over how atoms assemble are often based upon either local chemistry [3.3] or strain [3.19,3.20]. Here we demonstrate that a qualitatively different type of mechanism, in which an extra diffusion barrier to an atom crossing a step [3.21,3.22] can lead to self

assembly of a variety of ordered arrangements of nanometer-sized “mounds” during epitaxial growth on a patterned substrate.

A familiar example of self-assembly is crystal formation, in which atoms align in periodic arrangements which are dictated by local bonding. In this process kinetics limits the degree to which the lowest-energy, ordered arrangements can form. On the other hand, kinetic barriers have long allowed for the fabrication of structures in which atoms are not in their lowest free energy configurations. A particularly interesting type of diffusion barrier at step edges [3.21, 3.22] has been shown to lead both to the formation of multilayer islands or “mounds” during crystal growth [3.23-3.30] and step bunching or meandering instabilities during sublimation [3.31] or growth [3.32], respectively. Work by Tadayyon et al. on epitaxial growth of GaAs on patterned GaAs(001) substrates showed evidence that this “Ehrlich-Schwoebel” (ES) barrier might play a role in a transient growth instability we observe [3.33]. In this chapter we investigate the role of the Ehrlich-Schwoebel barrier during growth on patterned surfaces using kinetic Monte Carlo (kMC) simulations. Much of this work has been published in a recent article [3.40].

3.1 KMC Simulation Results

As mentioned in the previous chapter, we include the Ehrlich-Schwoebel barrier effect in our kMC simulations to probe its effect directly during crystal growth. In our early simulations we treated the Ehrlich-Schwoebel barrier as an adjustable parameter. As we are most interested in understanding its effect, we began with a relatively large Ehrlich-Schwoebel barrier, 0.1 eV, comparable to what is expected on certain metal surfaces, for example: Pt; we have also carried out an investigation of the effect of varying this barrier, presented below. Other energetic barriers are employed in a reasonable range of those resulting from first-principles calculations [3.37].

In Fig. 3.1 we show a series of simulated topographies for growth on a patterned surface at 600K, with diffusion barrier of E_d = 1.2 eV, an in-plane nearest-neighbor interaction energy of E_a = 0.3 eV and an Ehrlich-Schwoebel barrier of E_{ES} =0.1 eV . After about 10ML of growth, mounds form on the surfaces; these coarsen with deposition during the early stage of growth. The formation of mounds agrees qualitatively with simulations carried out several years ago by Johnson et al.[3.23], who attempted to model the unstable growth on unpatterned GaAs(001) surfaces during MBE growth.

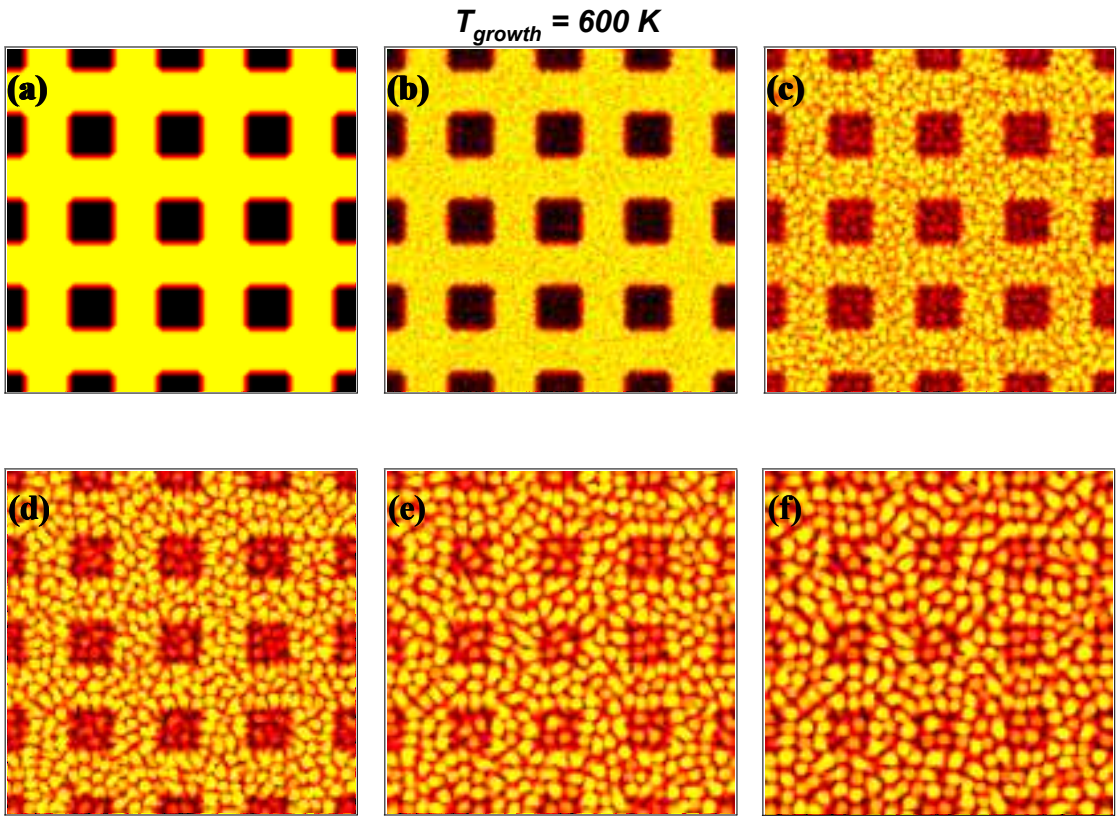

Fig.3.1 *Snapshots of simulated surface morphologies during growth at temperature 600 K with overall layer thicknesses of (a) 0ML; (b) 1ML; (c) 10ML; (d) 50ML; (e) 200ML (f) 500ML. The components of the energetic barriers were set at* E_d *=1.2 eV,* E_a *=0.3 eV,* E_{ES} *=0.1 eV, Flux= 1 ML/sec.*

In Fig. 3.2 we show the result of greatly lowering the value of Ehrlich-Schwoebel barrier in our kMC simulations, from 0.1 eV to 0.01 eV, on the formation of growth mounds. By comparing the images in Figs. 3.1(f) and 3.2(c), both of

which show the surface topography after 500 ML of growth at temperature of 600 K, we see the following in the low Ehrlich-Schwoebel barrier regime: first, the mounds become more irregular; second, the predefined patterns (artificial steps) have less of a tendency to direct the assembly of mounds; and third, three-dimensional island growth on the surface is surpressed; rather the simulation shows two-dimensional growth.

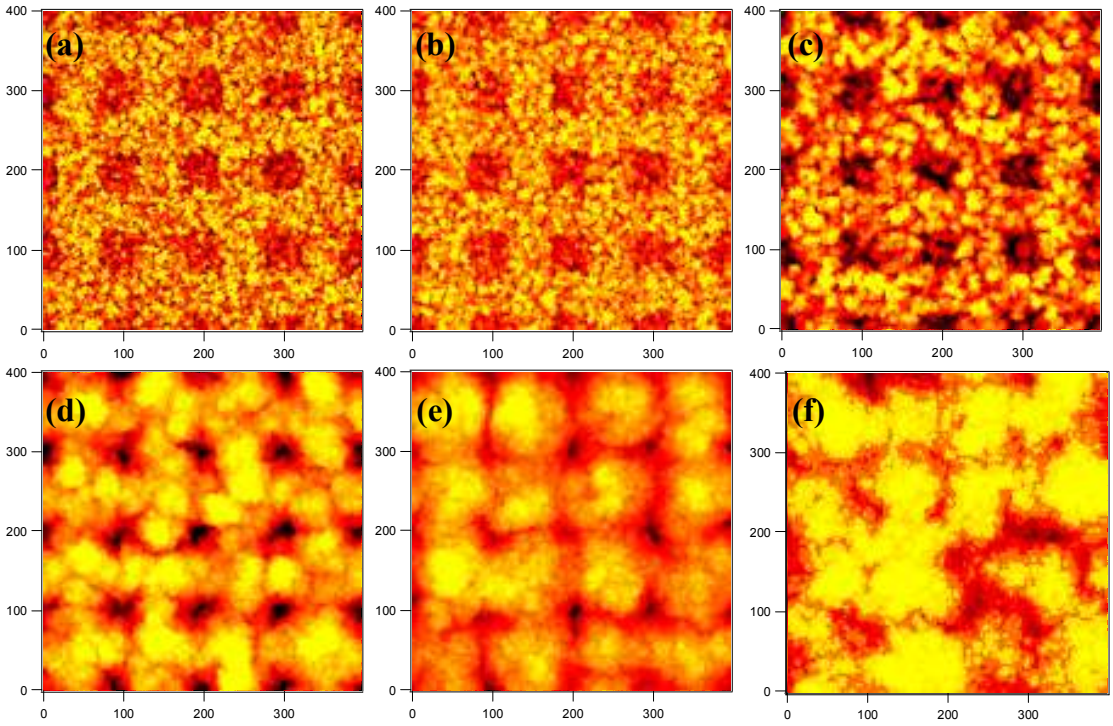

Fig.3.2 *Snapshots of simulated surface morphologies after 500 ML of growth with a reduced Ehrlich-Schwoebel barrier of E_{ES} = 0.01 eV, at growth temperature of (a) 500K; (b) 550K; (c) 600K; (d) 650K; (e) 675K (f) 700K. Other energetic parameters were set as E_d =1.2 eV, E_a =0.3, Flux= 1 ML/sec.*

At a relatively high temperature of 850K with the value of Ehrlich-Schwoebel barrier 0.1 eV, we see an inward collapse of the patterns and complete relaxation at an early stage of growth, 50 ML, as shown in Fig. 3.3. Growing at high enough temperature, the thermal energy of diffusing atoms on the surface is sufficient to overcome the Ehrlich-Schwoebel barrier, reducing the instability and eliminating the formation of mounds on the surfaces.

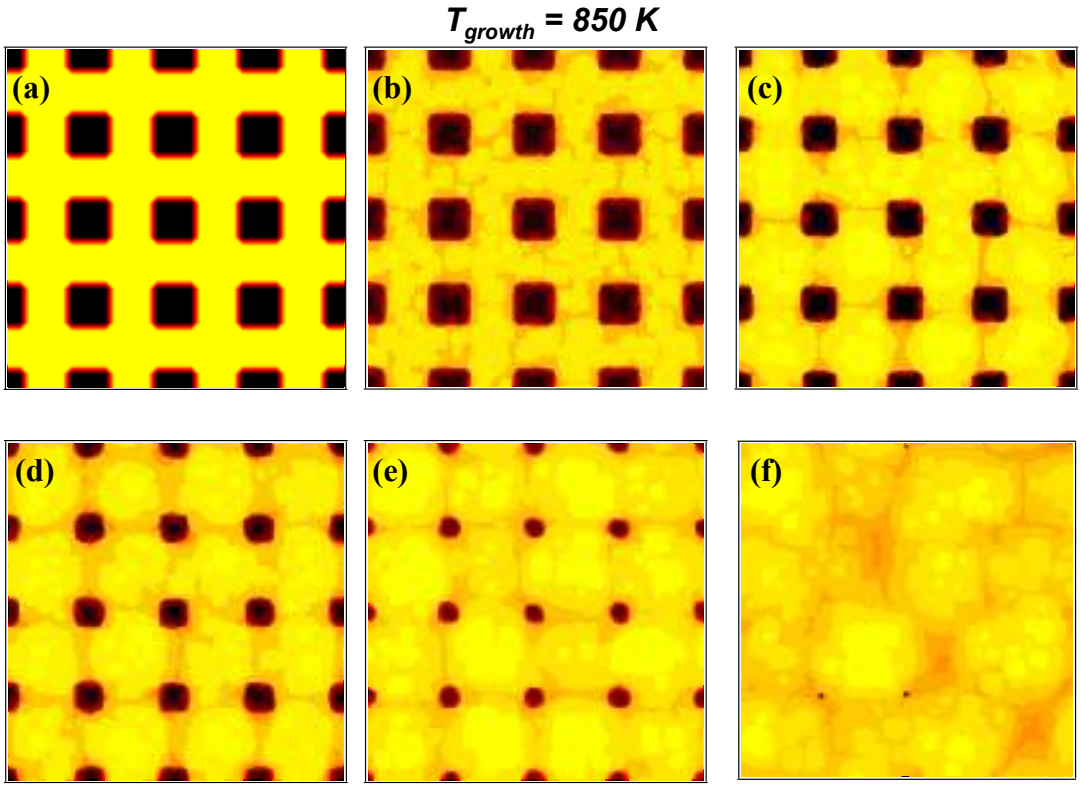

Fig.3.3 *Snapshots of simulated surface morphologies during growth at a temperature of 850K with layer thicknesses of (a) 0ML; (b) 1ML; (c) 5ML; (d) 10ML; (e) 20ML (f) 50ML. Energetic parameters were set as* E_{ES}*= 0.1 eV,* E_d *=1.2 eV,* E_a *=0.3, Flux= 1 ML/sec.*

Our kMC results indicate that for a moderate Ehrlich-Schwoebel barrier, and within a temperature window, patterns containing artificial step bunches (e.g. the sidewalls of the pits) on the surface can direct the self assembly of growth mounds kinetically.

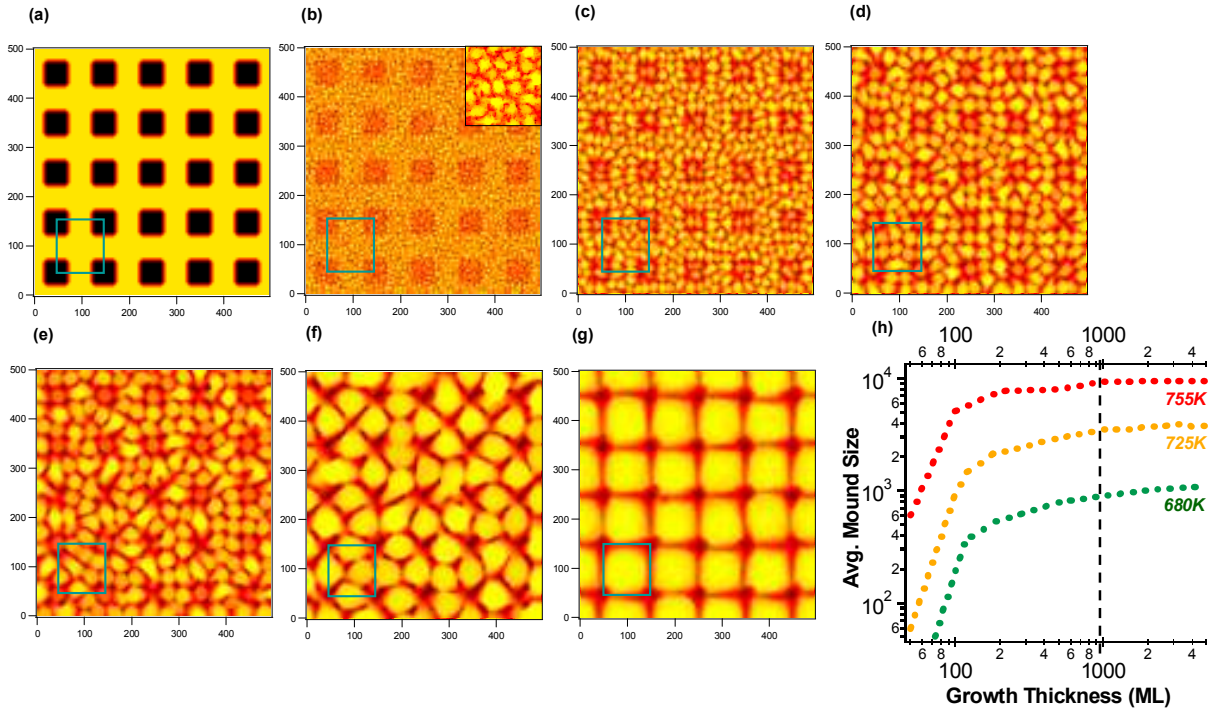

Fig. 3.4 Simulated topography vs. growth temperature*. (a) initial patterned surface; pits are 50a wide, 10a deep and separated by A=100a center-to-center, where a is the lattice constant. (b)-(g) simulated topographies after 1000ML grown thickness, at 1 ML/s. Energetic barriers are E_d=1.2 eV, E_a=0.3 eV, E_{ES}=0.1 eV. Growth temperatures are: (b) 550K; (c) 650K; (d) 680K; (e) 695K; (f) 725K; (g) 755K; (h) summary of average mound size vs. grown thickness at a series of temperatures; dashed line indicates 1000ML.*

In Fig. 3.4, we summarize our simulation results for an Ehrlich-Schwoebel barrier of 0.1 eV over a range of growth temperatures. Fig. 3.4(a) shows the starting surface, while Figs. 3.4 (b)-(g) show the topography that results after the simulated growth of a film of 1000 monolayers average layer thickness at a rate of 1 ML/s, for a series of increasing temperatures. Fig. 3.4(h) summarizes the average mound size vs. growth thickness for temperatures across this range and indicates that after 300 monolayers of growth, the average mound size nearly reaches steady state. Thus the snapshots we show here for 1000 ML thus reflect near-steady states of the evolution of surface topography in each case.

Fig. 3.4(b) is for simulated growth at a temperature of 550K, and shows a high density of irregular mounds decorating the surface. The dendritic shapes of individual mounds indicate that diffusive motion of atoms is slow compared to the arrival of new atoms from the flux at this temperature and suggest diffusion limited aggregation (DLA) growth [3.43]. Increasing the temperature results in the formation of larger mounds of more regular shapes, as can be seen in Figs. 3.4(c)-(d). By 680 K a strong correlation between the positions of the mounds and the original pattern is visibly evident, in which one growth mound sits at the center of each pit, and roughly two growth mounds form on the "bridge sites" in between neighboring pits. Further increases in the temperature result in larger mounds, whose shapes evolve from nearly isotropic, to distinctly diamond-like at 725 K. Fig. 3.4(f) show that growth of 1000 ML at 725K results in pits which have shrunk and mounds which form mainly at the bridge site between neighboring pits. On increasing the

temperature more, the mounds coarsen even further. In Fig. 3.4(g), which is for growth at 755K, the mounds almost span the entire pattern period to evolve to square shape. The initial pattern seemingly acts as an array of pinning sites to constrain the mound shapes and sizes. Growing above 770K produces mounds whose size exceeds that of the pattern cell, and the shapes become less regular.

3.2 Mound-Mound Separation Analysis

3.2.1 Height-Height Correlation Function Analysis and Correlation Maps

In this section, we statistically analyze the effect of the initial topographical pattern on the self assembly of the growth mounds, particularly evident in Figs. 3.4(d), 3.4(f) and 3.4(g), using a correlation function, defined as:

$$G_2(\vec{r}_{//}) \equiv \left\langle \left(z(\vec{R}_{//}) z(\vec{R}_{//} + \vec{r}_{//}) \right) \right\rangle_{\vec{R}_{//}} \quad .....(3.1)$$

In this expression $z(\vec{R}_{//})$ is the local height of the surface at a particular lateral position $\vec{R}_{//}$, $z(\vec{R}_{//} + \vec{r}_{//})$ is the height at position displaced laterally from this by $\vec{r}_{//}$ and $\langle\ \rangle_{\vec{R}_{//}}$ denotes the average over all values of $\vec{R}_{//}$. A more conventional form of the height-height correlation function (which we refer to as G_1 to distinguish from the one which we use in our analysis) is given by:

$$G_1(\vec{r}_{//}) \equiv \left\langle (z(\vec{R}_{//} + \vec{r}_{//}) - z(\vec{R}_{//}))^2 \right\rangle_{\vec{R}_{//}} \quad .....(3.2)$$

These two forms of the height-height correlation have a simple relation, and are equivalent in a statistical point of view. However, separations for which the height is highly correlated yield a peak in G_2, but a valley in G_1, i.e. they are complementary to each other. We adopt the former (i.e. G_2 , Eq.(3.1)), as this relationship between relative height and correlation seems more intuitive than that for the latter. Based on the simulated images, using Eq. (3.1) we can generate the corresponding real space, two-dimensional correlation maps. Fig. 3.5 shows some characteristics of the corresponding correlation maps which can be adopted to probe the long range ordering of the evolving nanostructures and surface morphologies during growth. Fig. 3.5(a) shows a perfect periodic structure, i.e. the model starting surface that we use in our kMC simulations, and the corresponding correlation map according to Fig. 3.5(a) is shown in Fig. 3.5(d). It consists of a set of peaks, with the separation between peaks given by the period of the starting patterns. This can be understood based on the fact that shifting the whole structure over one pattern period "*A*", results in a structure which is identical with that before the shift, i.e. the resulting structure is completely correlated. Consistent with this, profiles taken along the dashed arrow line shows that the intensity of the "first-order" (i.e. $R=A$) peaks, i.e. those displaced from the map center by a distance equal to the pattern period A along the horizontal <100> and vertical <010> directions, in this case is identical to the that of the central peak. More generally, based on the definition of height-height correlation function (Eq. (3.1)), the height of the central peak in these correlation maps is equal to the mean-square corrugation amplitude, with contributions from both the mounds that assemble spontaneously during growth and what remains of the original pattern. The

height of the "first-order" peaks gives a measure of the persistence of the pattern during growth.

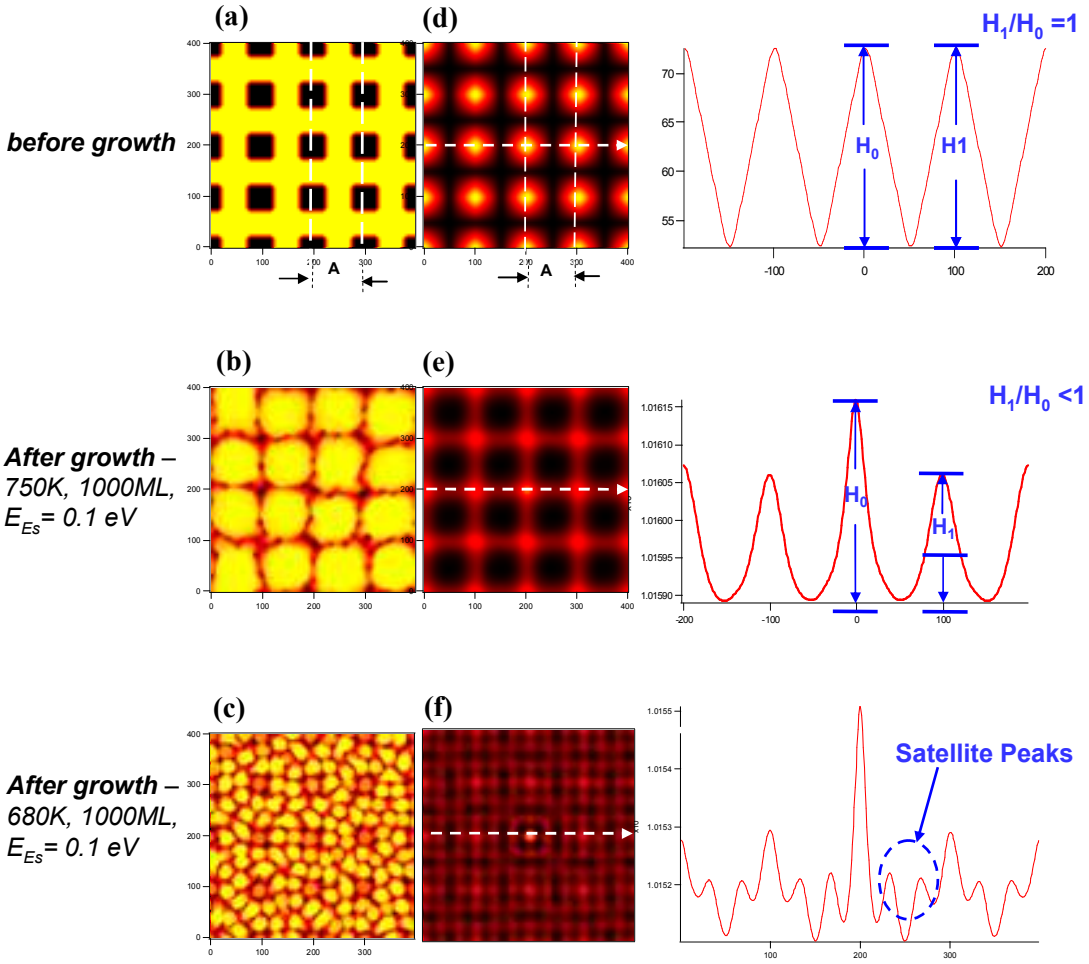

Fig. 3.5 Simulated topography and corresponding correlation maps*. (a) initial patterned surface with perfect periodicity; (b) surface topography with limited periodicity of patterns, growth at 750K after 1000ML of growth; (c) surface topography with ordered arrangement of mound structures, growth at 680K after 1000ML of growth; (d),(e) and (f) show the corresponding correlation maps and line profiles taken horizontally across the center of (a),(b) and (c), respectively.*

Therefore, for the grown surface morphology with limited order, as shown in Fig. 3.5(b), the correlation map shows periodic arrays; however, the height of "first-order" peaks has been reduced relative to the height of central peak (as shown in Fig. 3.5(e)). This indicates that the order is reduced, relative to that of the starting surface, due to the growth. From the point of view of directed self-assembly, the most interesting feature that arises during growth on our model patterned surfaces is the additional peaks-(which we hereafter refer to as "satellite peaks") which appear between those at displacements given by integral combinations of the pattern unit vectors; These are visible in Fig. 3.5(c) and (f); they signify additional periodicities that arise due to the ordering of the growth mounds. The separation between the first satellite peak position and the central peak corresponds to separations between mounds.

3.2.2 Comparison of Growth on Patterned and Unpatterned Surfaces

In this section, we compare the growth behavior on substrates with and without patterns, using analysis based on height-height correlation maps.

In Figs. 3.6 (a)-(d), we show the correlation maps calculated from kMC simulations of growth on patterned surfaces at 550K, 680K, 725K and 755K. Fig. 3.6 (b) is the correlation map corresponding to Fig. 3.4 (d), in which we see the separation between the positions of first satellite peak (right double-dotted line) and central peak (left double-dotted line) along <100> orientation is one-third of the pattern period (A/3); which confirms the visual impression from Fig. 3.4(d), i.e. that two mounds tend to form in the bridge between pits resulting in a (A/3 x A/3) structure. Fig. 3.6 (c) shows the correlation map corresponding to Fig. 3.4 (f). The positions of satellites have rotated by 45 degrees and appear only along <110> directions; the spacing between two dotted lines in the figure is exactly $A/\sqrt{2}$, and shows that the arrangement of mounds adopts an ($A/\sqrt{2}$ x $A/\sqrt{2}$) unit cell for growth at this temperature. The simulated images in this range (e.g. Fig. 3.4 (f)) show that a single mound forms in each bridge-site between near-neighbor pits; mounds do not form within pits at these temperatures. Fig. 3.6 (d) shows the correlation map from Fig. 3.4 (g); at this temperature, the mounds assemble into a third, even lower coverage arrangement, and adopt an (A x A) unit cell, in which all satellites are absent (i.e. coincide with integral peaks) in the correlation maps.

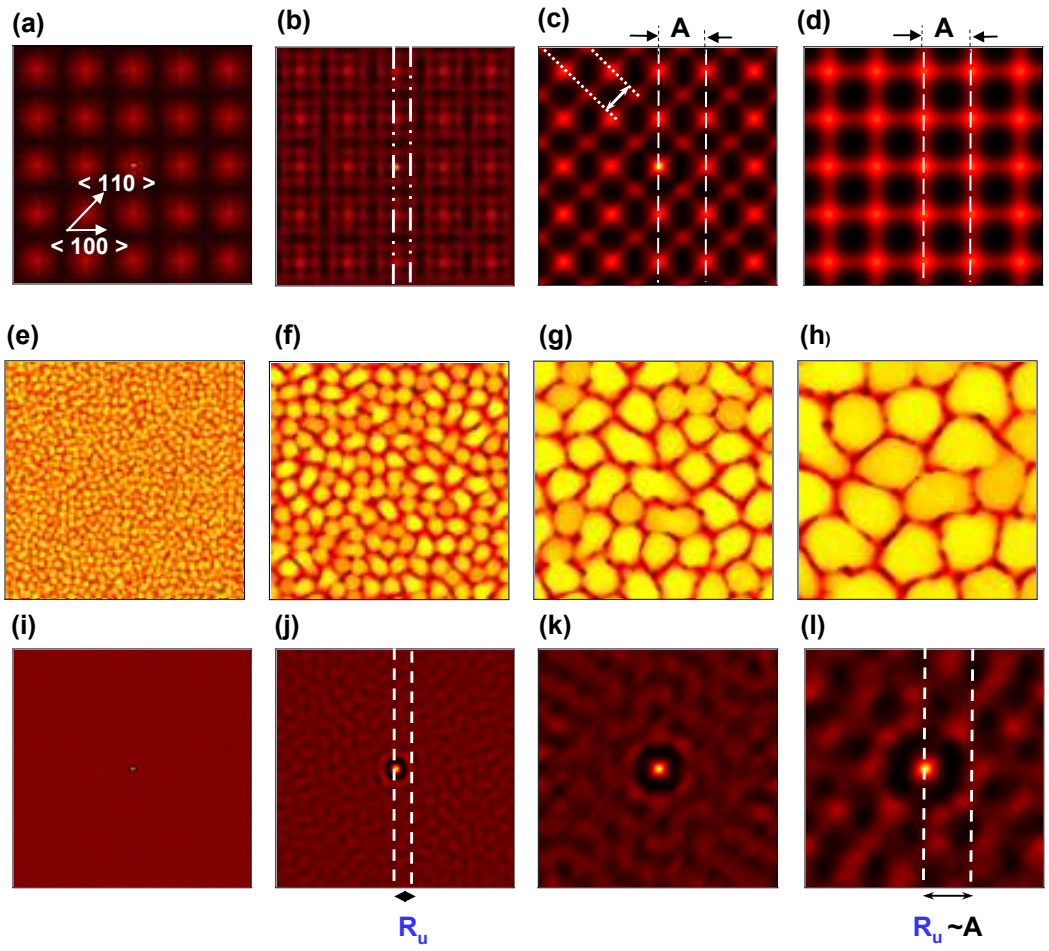

Fig. 3.6: Correlation maps for growth on patterned and unpatterned surfaces.

After 1000ML simulated growth, at 1 ML/s. (a) growth at 550K on patterned surface showing weak ordering; (b) growth on patterned surface at 680K, showing square ordering; double-dot dash lines show a separation of A/3; (c) growth on patterned surface at 725K, showing diagonally-ordered structure; dotted lines show a pacing of √2A/2; (d) growth at 755K on patterned surface showing original pattern period; 3.6 (e)-(h) growth on un-patterned initial surface (e) at 550K; (f) at 680K; (g) at 725K; (h) at 755K; 3.6 (i)-(l) corresponding correlation maps of 3.6 (e)-(h), showing liquid-like ordering: R_u indicates the radius of the ring in the correlation maps, corresponding to the near-neighbor mound separation.

This behavior is in sharp contrast to what we find for simulated growth on an unpatterned surface. Figs. 3.6 (e)-(h) show the topographical images of simulated growth on unpatterned surfaces at 550K, 680K, 725K and 755K; mounds again form on the surfaces due to the effect of Ehrlich-Schwoebel barrier. However, in the absence of initial patterns, mounds show nearly-close-packed arrangements with "natural" (near-neighbor) spacings which increase with temperature. Figs. 3.6 (i)-(l) show the corresponding correlation maps of Figs. 3.6 (e)-(h), respectively. The correlation maps on unpatterned surfaces show a nearly isotropic ring surrounding an excluded area around the central peak, but otherwise no indication of orientational ordering of the mounds: the arrangement is "liquid-like". The radius of the ring (R_u) in the correlation maps corresponds to the "natural" nearest neighbor mound separation.

Further analysis of the positions of the satellites as a function of temperature reveals an intriguing behavior in the assembly of mounds when an initial topographical pattern is present. This can be seen in Fig. 3.7, where we plot the position of the nearest satellite peaks along both the horizontal <100> and diagonal <110> directions vs. the radius of the ring (natural nearest neighbor spacing) on the unpatterned surface. The arrangement of mounds locks into a series of ordered arrays whose period is related to that of the pattern as the temperature is increased. This behavior is reminiscent of "devil's staircases", or sequences of higher-order commensurate phases which form as temperature or pressure is changed in adsorbate systems when there is a competition between preferred adsorbate-spacings and

substrate periodicities [3.38]. For growth at or below 600K the distances from center of the closest satellites along both of these directions are equal and given by the radius of the ring (R_u). At these low temperatures the mound separations are thus isotropic, and relatively insensitive to the presence of the pattern, which show up as a background in the correlation maps. By a growth temperature of 660K the pattern clearly exerts an influence on the mound spacing: the symmetry of the satellites visually indicates that the mounds assemble into a square lattice, with the ratio of the distances to the nearest diagonal satellite and to the nearest horizontal satellite in the ratio of $\sqrt{2}$:1. Interestingly, the mound lattice has adopted a lattice spacing of A/3, rather than the "natural" value of 0.26A which it would have in the absence of the pattern. It remains locked into this structure up until a temperature of 700K, in spite of an increase in the unpatterned mound spacing to 0.43A. Increasing the growth temperature slightly, to 710K, causes an abrupt change in the arrangement in which the mounds assemble. Evidently driven by the significantly larger natural spacing, the mound lattice rotates by 45 degrees, and adopts an ($A/\sqrt{2}$ x $A/\sqrt{2}$) unit cell. As for the intermediate temperature ($A/\sqrt{2}$ x $A/\sqrt{2}$) structure, the mounds lock into this lower coverage structure over a range of temperature, up to approximately 735K. Raising the temperature to 740K causes the mounds to assemble into a third ordered phase. The simulations show that the larger natural spacing of the mounds is accommodated by the assembly of individual mounds in the 4-fold sites between pits and form (A x A) structures. At the approximate center of the temperature range for this structure, 755K, the pattern period A coincides with the spacing mounds would naturally adopt. Increasing the growth temperature above 770K results in a

disordered structure; there is no simple relation of the placement of these large mounds to the topographical pattern, and even the first-order peaks are absent in the correlation maps.

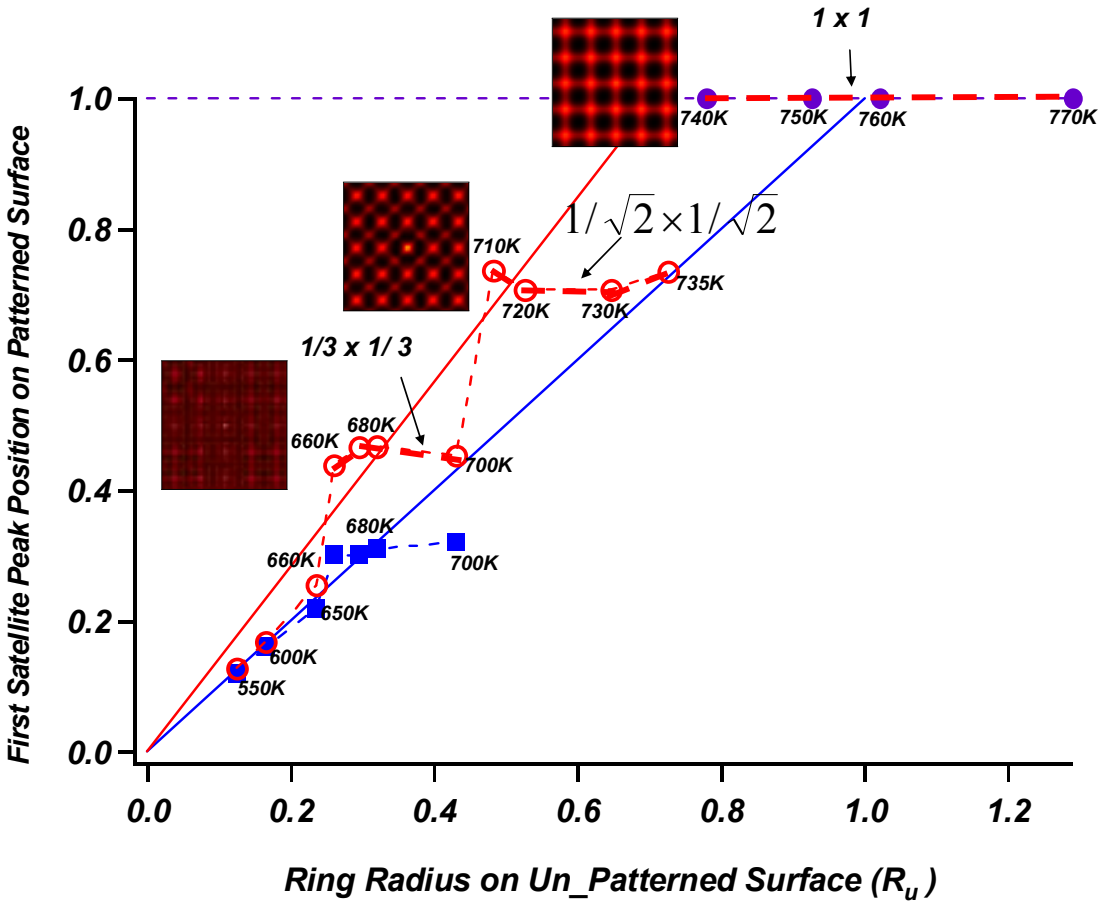

Fig. 3.7: Evidence for lock in of mounds to series of ordered structures. *Nearest satellite peak position from correlation maps after growth on patterned surface vs. ring radius for unpatterned surface, along <110> (red open circles) and <100> (blue solid squares). After 1000ML grown thickness, at 1 ML/s, with temperature as indicated. Solid blue line has slope 1, corresponding to mound spacing along <100> equal to that on an unpatterned surface. Solid red line has slope √2. Mound lattice vectors relative to pattern are indicated for three ordered structures. Insets from top to bottom show the correlation maps of surface morphologies after growth at 755K, 725K and 680K, respectively.*

3.2.3 The Effect of Changing Pattern Parameters on Mound Separation

An interesting question concerns how the choice of initial geometrical parameters might affect which ordered mound arrangements occur for growth on a patterned surface. To investigate this we carried out additional simulations for geometries in which the relative values of different pattern length scales are changed. We find that changing the depth of the pattern at fixed width and pitch has a subtle effect, as summarized in Fig. 3.8 for the case of the same pattern pitch and pit-width as in Figs. 3.1 - 3.4, but with the depth tripled to h = 30a. The same sequence of phases as in the h = 10a case occurs, with only changes in the transition regions between them. This may be in part due to the finite sidewall angle which causes a decrease in the widths of the flat mesa widths between pits with increasing pit depth.

On the other hand, changing the starting pit-widths for a fixed pitch and depth gives rise to a different sequence of mound structures with increasing temperature. Figure 3.9 summarizes the results for growth simulations in which the pitch and depth are maintained at the same values as in Figs. 3.1- 3.4, but in which the initial width of the pits is 0.75 times the pitch, i.e. w=75a. In this case the simulations predict four, rather than three ordered mound structures, with unit meshes given by A/5 x A/5, A/3 x A/3, A/2 x A/2 and A x A as the growth temperature is increased. Interestingly, the rotated $A/\sqrt{2}$ x $A/\sqrt{2}$ structure is "missing" in this case.

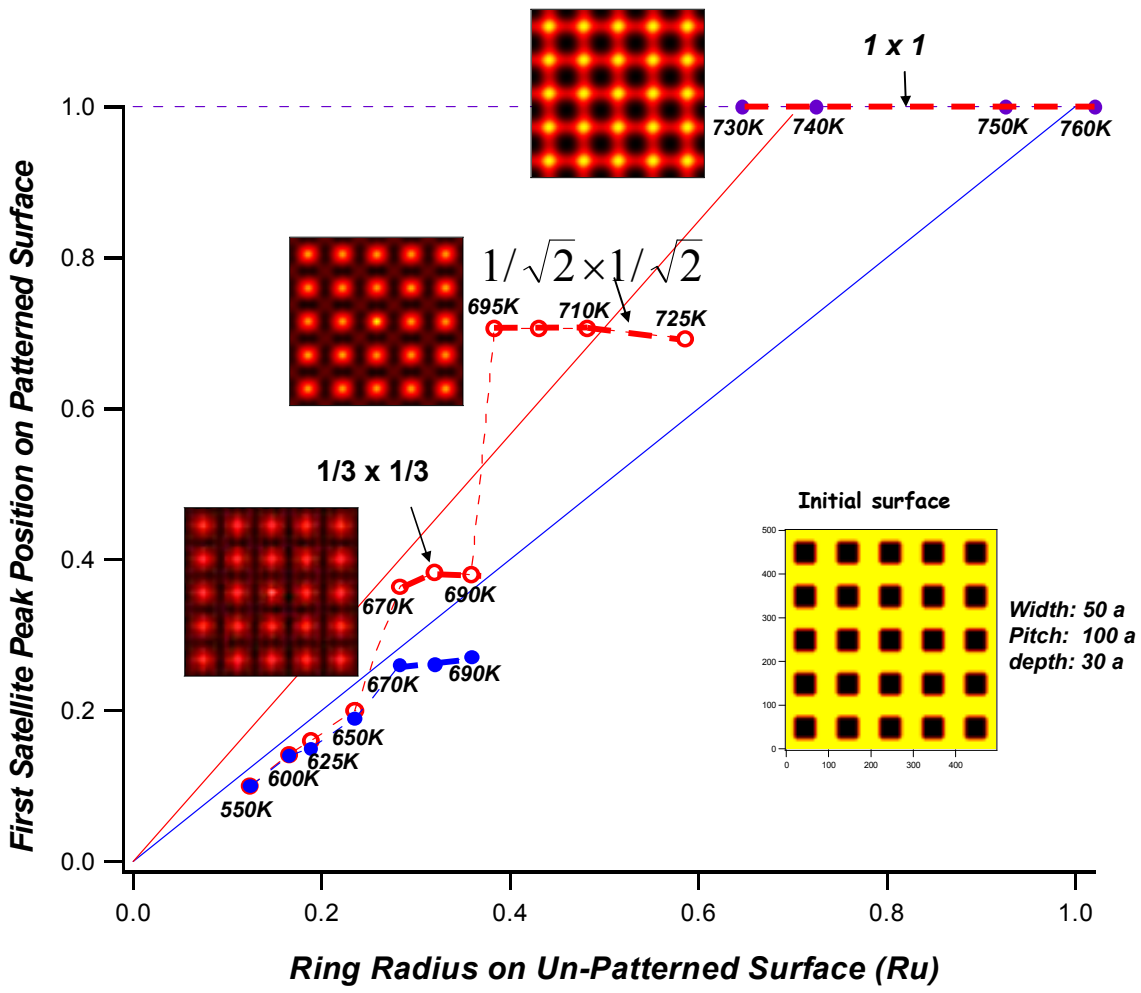

Fig. 3.8 Effect of pattern parameters on sequence of mound structures with temperature- changing depth of initial patterns *Nearest satellite peak position from correlation maps after simulated growth on patterned surface vs. ring radius for unpatterned surface, along <110> (red open circles) and <100> (blue solid squares). Satellite positions for initial pattern pitch A =100a and width w = 50a, but depth increased to h = 30a. Insets from top to bottom show the correlation maps of surface morphologies after growth at 740K, 710K and 680K, respectively. After 1000ML grown thickness, at 1 ML/s, with temperature as indicated.*

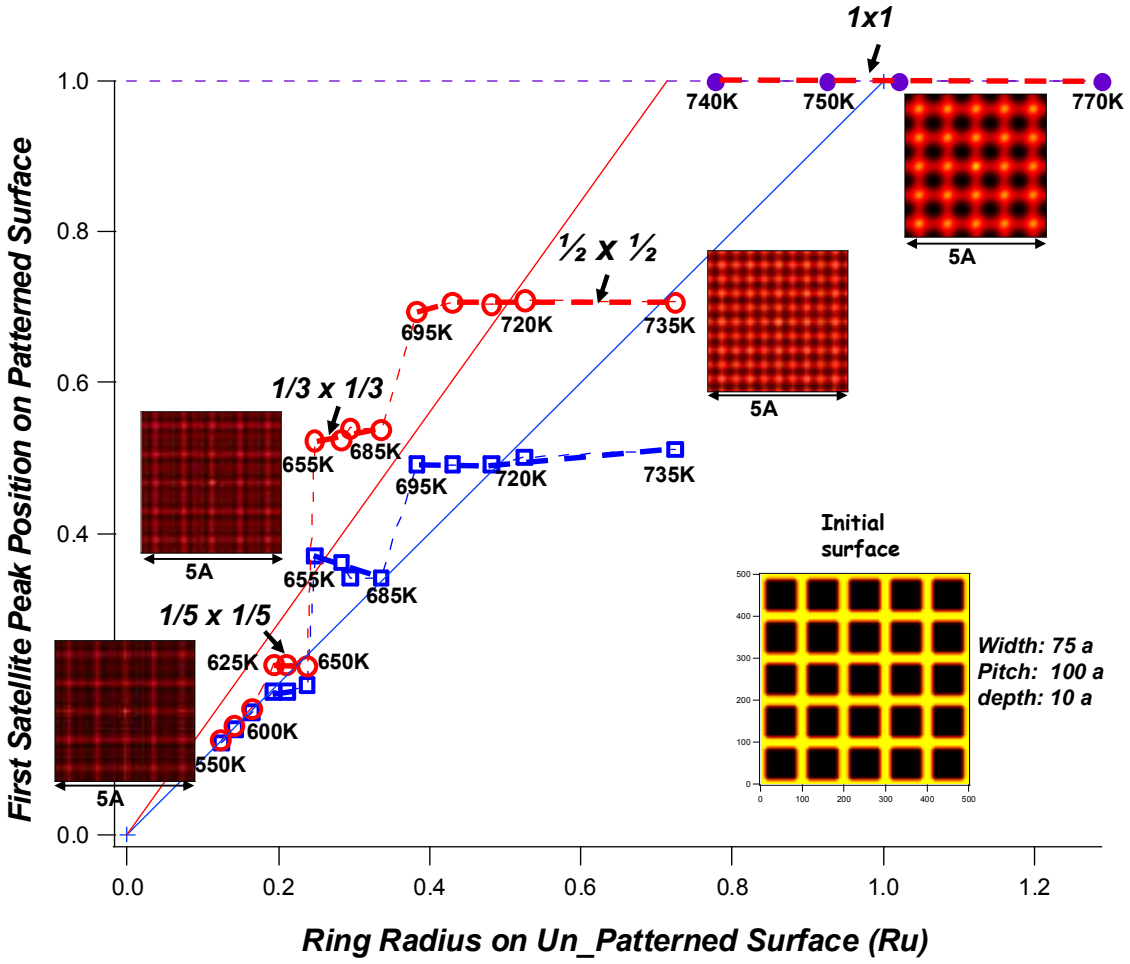

Fig. 3.9 Effect of pattern parameters on sequence of mound structures with temperature- changing width of initial patterns *Nearest satellite peak position from correlation maps after simulated growth on patterned surface vs. ring radius for unpatterned surface, along <110> (red open circles) and ,<100> (blue solid squares). Satellite positions for initial pattern pitch A = 100a, depth h = 10a and pit width w = 75a. Insets from top to bottom show the correlation maps of surface morphologies after growth at 760K, 720K, 675K and 630K, respectively.*

While we do not have a detailed understanding of the relationship between the pattern parameters and the mound structures which form, we expect that it involves a competition between a temperature-dependent natural nearest neighbor mound spacing, discussed above, and the pattern lateral length scales. The mound-pattern interaction is seemingly based upon the formation of mounds only on the flat mesas around and at the bottoms of pits. This restricts the configurational entropy of mounds on the surface, and results in an effective interaction which is entropic.

3.3 Effect of Changing Energetic Barriers and Growth Fluxes

One might wonder how general the series of self-assembled mound structures seen in Fig. 3.4 is. In particular: would a different set of barriers and growth flux produce mound structures with different periods? To address this we carried out additional simulations, changing Ehrlich-Schwoebel barrier over a wide range. Interestingly, we see the same sequence of three ordered phases in three temperature windows as the Ehrlich-Schwoebel barrier varies from 0.03 eV to 0.2 eV although the temperature boundaries shift to lower temperature ranges as we decrease the Ehrlich-Schwoebel barriers.

From Fig. 3.10 it is clear that for small Ehrlich-Schwoebel barrier, 0.03 eV, there are relatively small temperature windows in which each ordered phase forms. This is perhaps reasonable given that for a small Ehrlich-Schwoebel barrier, there is less tendency of mound formation. On the other hand, for a large Ehrlich-Schwoebel barrier, 0.2 eV, the apparent transitional regions (error bars) between ordered phases become significant. While this might be due to the possibility of wider regions of "phase coexistence", it may also indicate that for a very large Ehrlich-Schwoebel barrier interlayer transport is greatly reduced, slowing "equilibration" or better, achievement of near-steady state. .

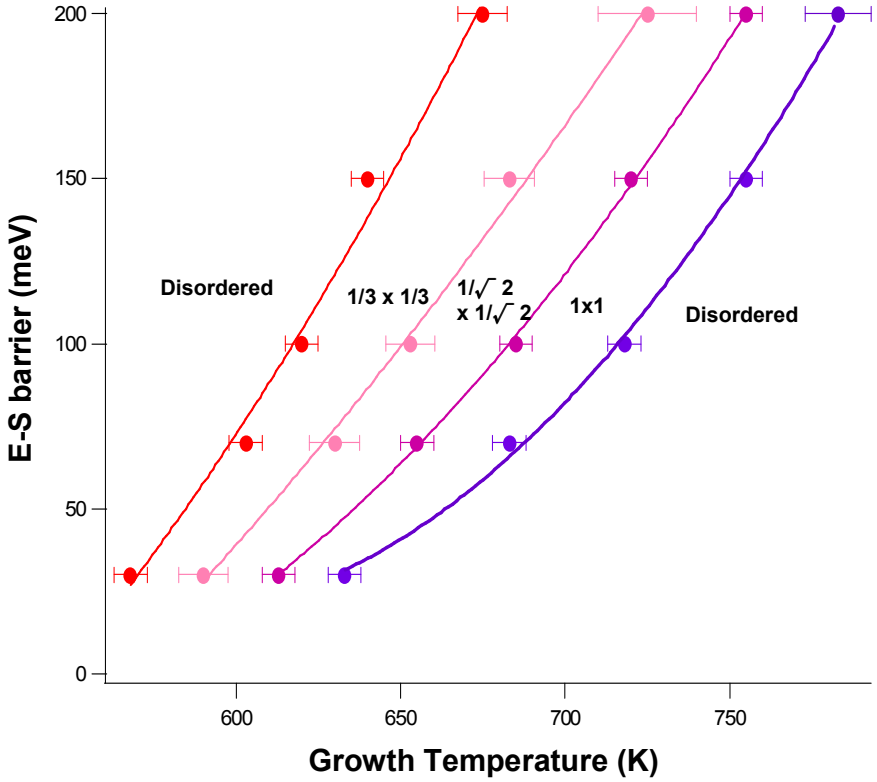

Fig. 3.10 Effect of changing Ehrlich-Schwoebel (ES) barriers. *The same sequence of three ordered phases shows up as the ES barrier varies from 30 meV to 200 meV.*

In addition , for an Ehrlich-Schwoebel barrier of E_{ES} = 0.1 eV we carried out simulations systemically changing the growth flux from 0.5 ML/s to 2.0 ML/s. Flux is important in self assembly since a competition occurs between the arrival of new atoms and the diffusivity of adatoms during growth. Once again, we find that the prediction is for a sequence of three ordered phases of mound arrangements as shown in Fig. 3.11.

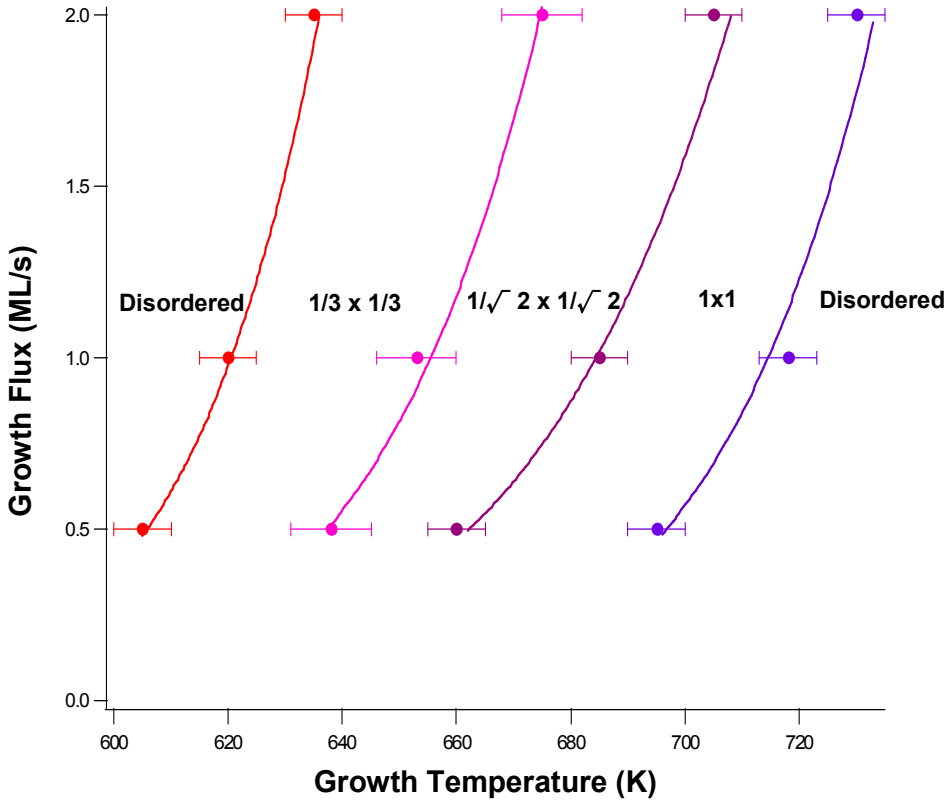

Fig. 3.11 Effect of changing growth fluxes. *Regions of three ordered phases shows for fluxes varying from from 0.5 ML/sec to 2.0 ML/sec. E_{ES} barrier is 0.1 eV.*

We also carried out simulations varying the diffusion barrier (E_d), from 0.8 eV to 1.2 eV, and the in-plane nearest neighbor interaction barrier (E_a), from 0.25 eV to 0.4 eV. In each case the same sequence of three ordered mound structures occur, although at different temperatures ranges. Overall, the prediction is that these directed self assembled structures should occur over a range of energy barriers on surfaces and incident fluxes.

3.4 Image Segmentation for Mound Size Analysis

From the systematical analyses of mound separations, we found a very interesting temperature dependence of ordered mound arrangements. A remaining, and interesting questions would be: what does this mean about the sizes of the mounds? Does the same lock-in series occur as a function of temperatures? In order to answer these questions, we carried out image segmentation to define each mound and calculate the average mound size after varying grown thicknesses.

3.4.1 Image Segmentation Method

A Fortran-based code (developed by Dr. Hung-Chih Kan) allows us to define the boundary of each mound and through that we can obtain the distributions of average mound size. The details of the code are provided in Appendix C.

Fig. 3.12 shows results of image segmentation on patterned substrates after 1000 ML of growth with various temperatures, which is indicated at the top of each image. The color codes used here is only for distinguishing mounds from their neighbors. From Fig. 3.12, we can see that the image segmentation works reasonably well in analyzing the average mound size vs. temperatures in the presence of initial patterns. Due to the limited size of each simulation frame, the statistics are limited, increasingly so for the growth at higher temperatures, as shown in the lower row of Fig. 3.12. In order to improve our statistics, we ran many sets of simulations and did the image segmentation for all sets of data.

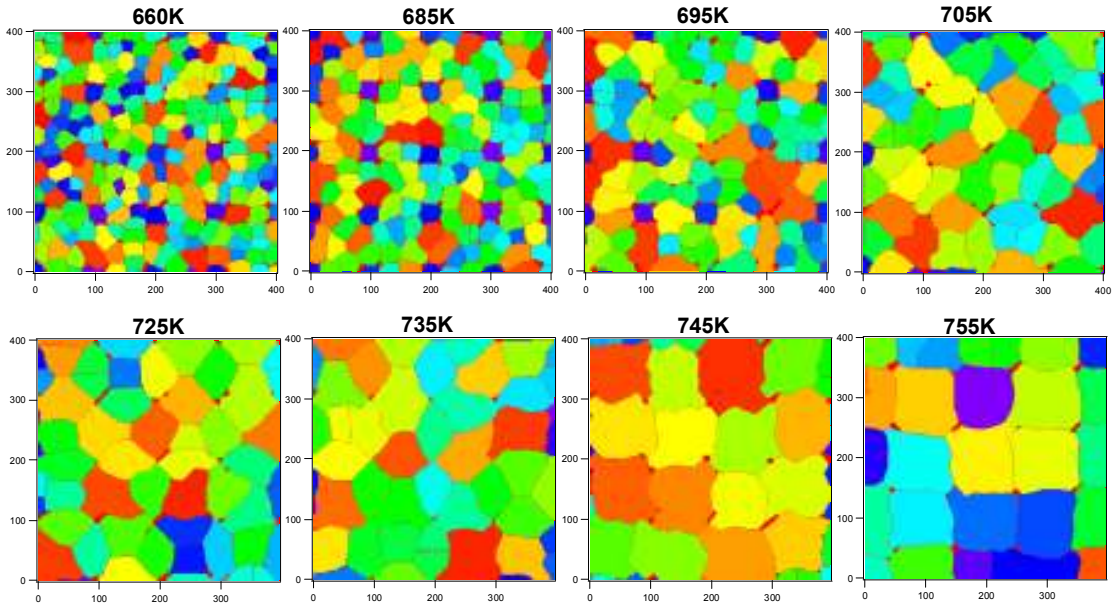

Fig. 3.12 Image segmentation of mounds grown on patterned surfaces. *The growth temperature for each case is indicated on top of each panel.*

For comparison and consistency, we use the same approach for results of the growth on unpatterned surfaces, as illustrated in Fig. 3.13. The image segmentation method again works nicely, and allows us to obtain the temperature dependent of "natural mound size". We plot the average mound size on patterned surfaces vs. natural mound size on unpatterned surfaces as a function of temperature, presented in Fig. 3.14, and discussed in the next section.

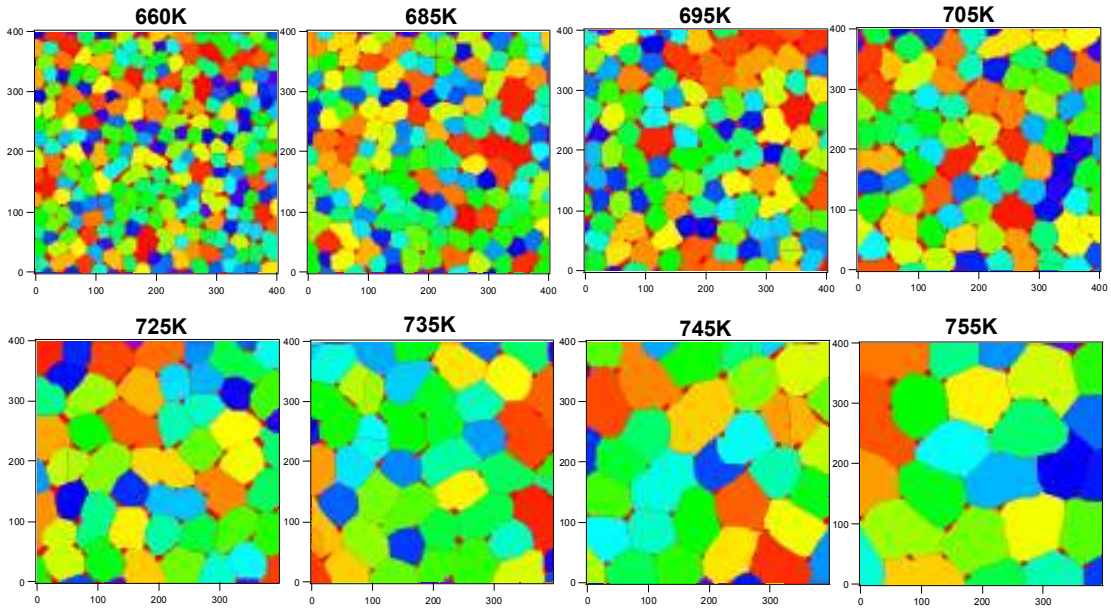

Fig. 3.13 Image segmentation of mounds grown on unpatterned surfaces. *The growth temperature for each case is indicated on top of each panel.*

3.4.2 Temperature Dependence of Average Mound Size

Interestingly, Fig. 3.14, indicates that the temperature dependence of the mound sizes shows some differences from what might be guessed from the temperature dependence of the correlation map satellite positions. No obvious break in the dependence of the mound size on temperature is seen in the range in which the (A/3 x A/3) structure forms; instead, the size of mounds follows its natural size (the mound size on unpatterned surface), which shows a monotonic increase of the mound size as

the temperature increases in the lower temperature growth regime. Surprisingly, in this regime, the mounds grow larger as a function of temperature, but the average separation is locked into a fixed amount. One can imagine that the interaction between mounds become increasingly repulsive with size, and that it becomes less favorable enegetically to accommodate mounds in the (A/3 x A/3) phase as the temperature increases. We next examine how the system responds.

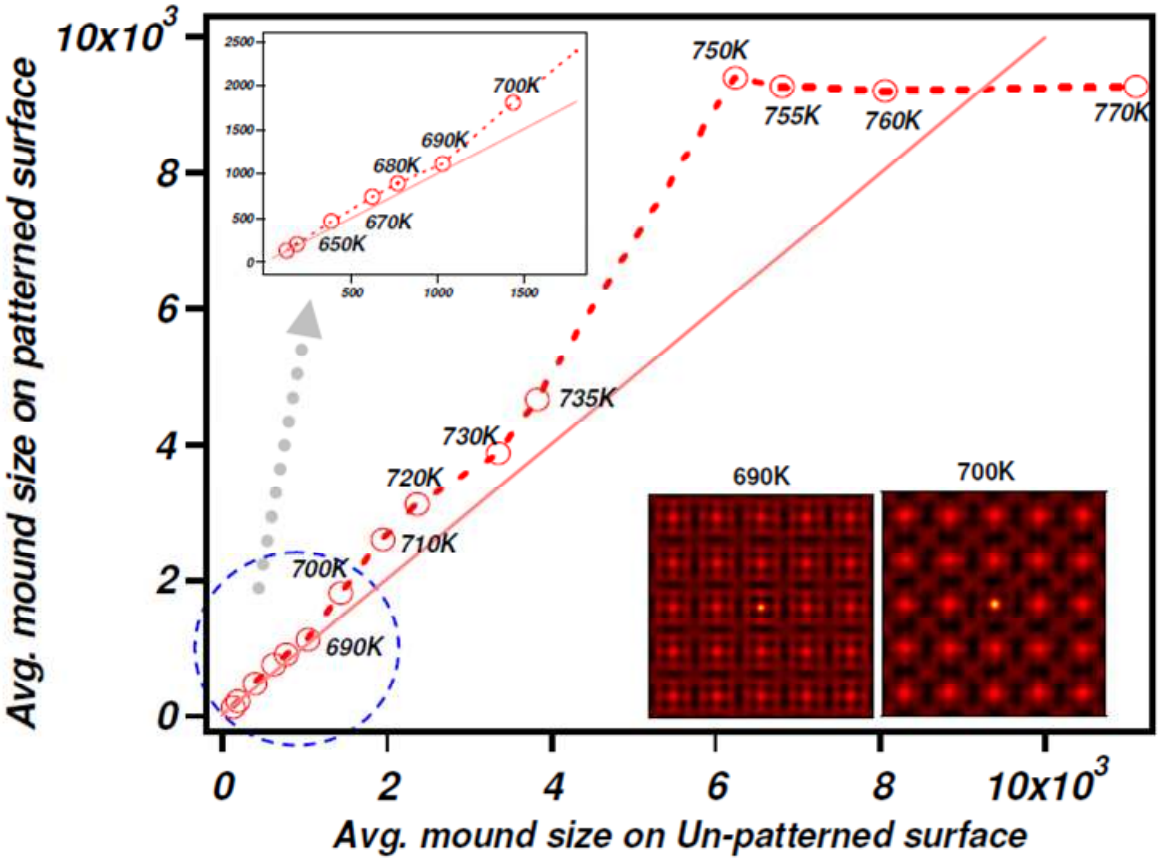

Fig. 3.14: Average mound size on patterned vs. unpatterned surfaces. *After growth of 1000ML at 1 ML/s, with temperatures as indicated. Insets at lower right are correlation maps for 690K and 700K, as indicated.*

In Fig. 3.15, the analysis shows a continuous decrease in the intensity of the nearest satellite along <100> relative to that along <110> as the temperature is increased from 680K to 700K, indicating that the mound lattice accommodates the increase in natural size by a continuous increase in the fraction of near neighbor mound-pairs which are separated along <110>, rather than <100> directions in this range. Indeed such a change in the near-neighbor arrangement of mounds is evident by comparing Figs. 3.4 (d) and (e), which in some sense the average arrangement of mounds is rotating in order to accommodate the mound with increasing size, and to turn the system into a lower density phase.

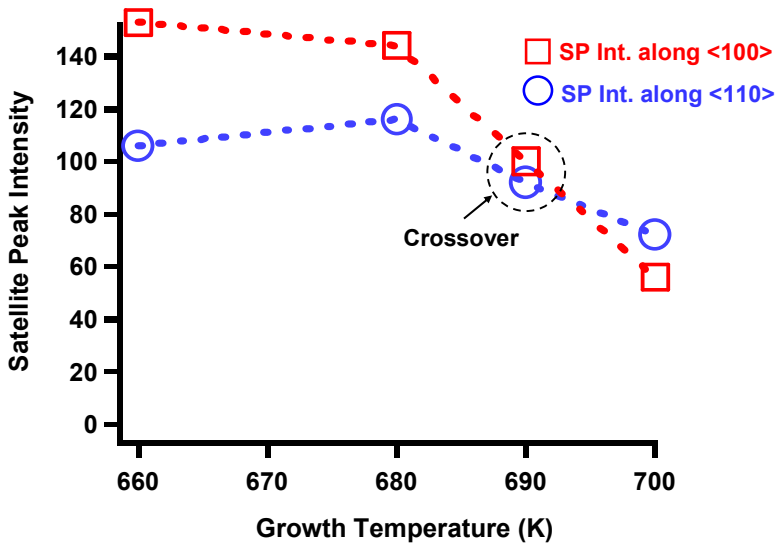

Fig. 3.15: Satellite peak intensity for peaks along <100> and <110> directions.

After growth of 1000ML at 1 ML/s, with temperatures as indicated.

We have also used the Generalized Wigner Surmise (GWS), which Einstein et al [3.41, 3.42] have used in terrace width distribution (TWD) analysis on stepped surfaces, to analyze our mound separation distribution. The details of this analysis are discussed in Appendix B.

3.5 Mechanisms of Directing Mounds

We now consider how an artificially imposed topographical pattern might act in directing the assembly of mounds during growth. One possibility is based upon the modification of the local density of adatoms on the surface. On relatively flat regions of a surface, such as those between the pits, growth via the formation of atom clusters ("islands") is favored over the addition of atoms to existing steps. As islands are most likely to form where adatom density is high, a seeming explanation for our observations is that the positions of the maxima in the adatom density relative to the pattern changes with temperature owing to thermal activation across the Ehrlich-Schwoebel barriers at the edges of pits.

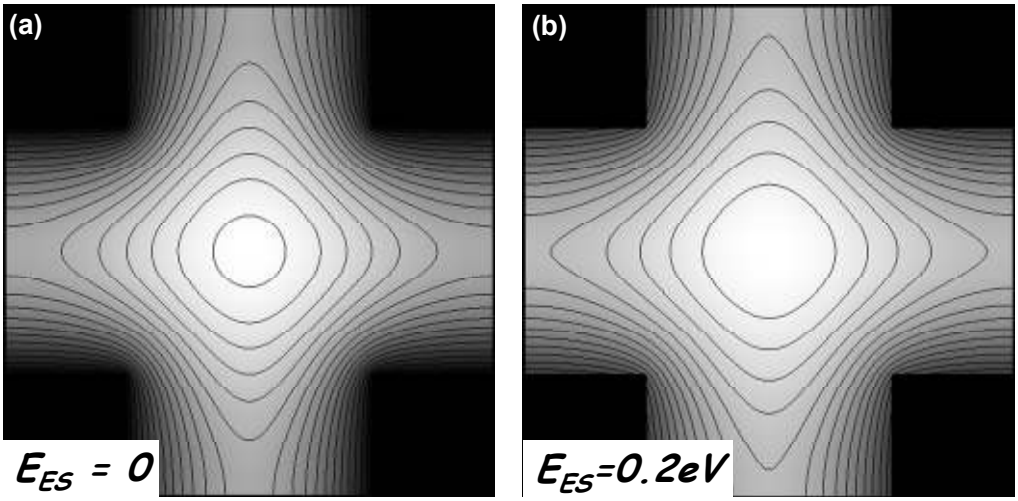

Fig. 3.16: Simulations of local density of adatoms by diffusion equation *(a) with Ehrlich-Schwoebe barrierl, E_{ES}=0 eV; (b) with E_{ES}=0.2 eV. Bright contrast: high density; dark contrast: low density.*

This possibility, however, is ruled out by a simple solution of the diffusion equation shown in Figs. 3.16 (a) and (b); the simulations based on the second Fick's law with and without the effect of Ehrlich-Schwoebel barriers both indicate that initially the adatom density is always highest between the corners of quartets of nanopit neighbors, which we refer as the centers of the "four-fold bridges" regardless the presence of Ehrlich-Schwoebel barriers. A moderate Ehrlich-Schwoebel barrier flattens this maximum out, but does not shift its position [3.39, 3.40]. Initially this favors island formation near the centers of the bridges between pits.

We thus further consider a second possibility, suggested by the upper-left inset of Fig. 3.14, that beneath 700K the mound sizes on the patterned surfaces follow those determined by kinetics in the absence of a pattern. This natural size arises from the competition of the Ehrlich-Schwoebel barrier, which favors vertical growth of multi-island stacks [3.24-3.31], and arrival of diffusing adatoms on the underlying surface favors lateral growth due to attachment to the edges of the bottom-most island. For this to be the correct explanation the mound positions would need to evolve during growth from the initial nucleation sites favored by highest adatom density to relative positions determined by their natural size, and the effects of the pattern. One of these is the reduction of the area of the underlying terrace, and thus the supply of adatoms for lateral growth, if a mound approaches the upper edge of a pit. Some evidence for this evolution is seen in Figure 3.17, which shows series of height profiles from our simulations for increasing grown thickness. Successive panels in this figure are for temperatures corresponding to the centers of the ranges in which the three ordered mound structures assemble for the pattern geometry of Fig. 3.4. For

the A/3 x A/3 arrangement of mounds seen in Fig. 3.4(d) two mounds can be accommodated in the bridge between near-neighbor pits, with a third forming in the pit bottoms; in Figure 3.17 (a) an initial height maximum forms near the center of the bridges in between two adjacent nanopits, which we refer as 2-fold bridge sites, but two maxima evolve near the bridge edges as the growth continues. Raising the temperature increases the rate of atom diffusion, and thus the natural size of the mounds. Larger mounds are accommodated by the 2-fold bridge sites in the A/$\sqrt{}$2 x A/$\sqrt{}$2 structure, and the largest in the 4-fold bridge sites of the A x A structure.

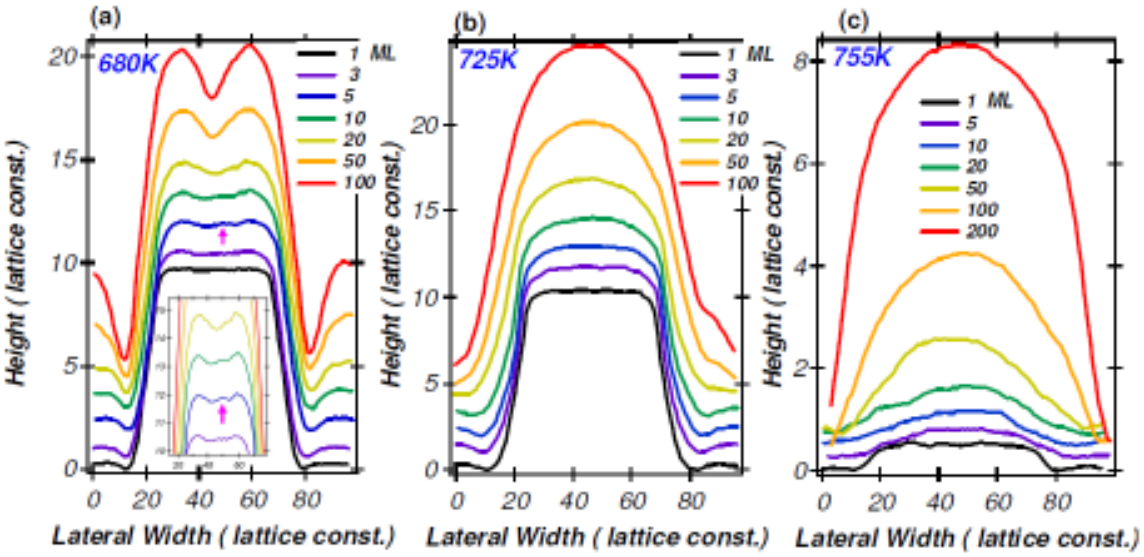

Fig. 3.17: Height profiles of simulated surfaces for increasing amounts of growth. *(a)-(b) show the evolution of morphologies of the 2-fold bridges at growth temperatures 680K and 725K, the arrow in (a) indicates a local height maximum near the center of 2-fold bridges at initial stage of growth; (c) shows the evolution of morphologies of the 4-fold bridges. The heights of profiles are rescaled to display subtle features at the early growth stage.*

3.6 Conclusion

The model used in our simulations is simple, and leaves out many effects, including elastic strain near the edges of pits, interaction between steps like those that bound the pits and anisotropy in the diffusivity and atom-step attachment probabilities. Nonetheless we show nice demonstration of the effect of Ehrlich-Schwoebel barrier both with the simulations and early experimental results.

In summary, our results show that a purely kinetic effect, i.e. an additional diffusion barrier, the "Ehrlich-Schwoebel" barrier, at step edges, which impedes atoms crossing steps from above, and has long known to produce mounds during growth on certain surfaces can act not merely to suppress the lowest energy atom arrangement during growth, but to direct a series of ordered arrangements of nanometer-sized mounds with temperature, by controlling the competition between the natural mound near neighbor spacing and the length scales imposed by an artificially produced pattern. The sequence of mound structures varies with the pattern length scales. Most importantly, the density of mounds in these structures can exceed that of the initial pattern, which demonstrate an amplification of resolution than the patterns we defined. We anticipate that this phenomenon could find application in the fast, controlled assemblies of nanostructures called for by current technology.

Chapter 4

Observation of Self-Limiting Growth in the Directed Self-Assembly of Mounds during Homoepitaxial Growth on Patterned GaAs(001)

In this chapter we report on growth experiments in a system for which directed self-assembly of nanostructures occurs, homoepitaxial growth on nanopatterned GaAs(001) [4.1, 4.2]. As shown in the previous chapter our kinetic Monte Carlo (kMC) simulations predict that the formation of a series of ordered "growth mounds", or island stacks at positions directed by the predefined topographical pattern arises in the presence of a sufficiently high additional barrier for diffusing adatoms to cross step edges from above, i.e. an "Ehrlich-Schwoebel" barrier [4.3- 4.5].

A remaining crucial issue in the application of directed self-assembly is that of the persistence of the structures that spontaneously evolve during processes such as

growth and deposition. There have been reports of the observation of certain types of "self-limiting" behavior in some experimental systems, with the interplay of energetic and kinetics during growth leading to the evolution of nanostructures which display a dominant size [4.6] or shape [4.7- 4.9]. These studies have not, however, dealt with self-limiting behavior in the literal sense of the term: i.e. how kinetics might limit the persistence of nanostructures during their evolution.

We investigate the question of the persistence of mounds during molecular beam epitaxial growth on nanopatterned GaAs(001) surfaces. We also investigate the evolution of preferred sites for mound formation in this system.. As we show in detail below, in the initial stages of growth, a lithographically-defined pattern directs the spontaneous formation of multilayer islands at the centers of bridges between near-neighbor nanopits along [110] crystal orientation, seemingly due to the presence of an Ehrlich-Schwoebel barrier. As growth continues, the heights of mounds at these 2-fold bridge sites "self-limit". Beyond this point mounds at other, 4-fold bridge sites dominate the topography, but these self-limit as well. We find that this self-limiting behavior leads to a range of film thickness over which these structures persist. This self-limiting behavior suggests the existence of a minimum, 'critical terrace width' for nucleation of islands during growth, and provides a physical mechanism for understanding the transient nature of the observed instability during growth on these patterned surfaces.

4.1 Results of Homoepitaxial Growth Experiments on Nano-Patterned GaAs(001)

4.1.1 Temperature Dependence of Growth Experiments

We have described in detail our experimental approach and setup for the experiments in chapter two. Here we review this material briefly. We patterned GaAs(001) wafers using e-beam lithography followed by inductively-coupling plasma etching, creating several sets of nanopit arrays in which the widths were varied from 60 nm to 400 nm, the center-to-center spacing maintained at twice the initial width, and the initial depths were approximately 50 nm. Patterned samples were cycled between a molecular beam epitaxy (MBE) growth chamber (base pressure 2 x 10^{-11} mbar) for homoepitaxial growth and an atomic force microscope (AFM) for surface topography determination in atmosphere. Before each growth experiment the surface oxide was desorbed by heating to 400 °C in the presence of an atomic hydrogen flux, resulting in negligible desorption induced roughness [4.29, 4.30]. The growth rate was held fixed at 0.28 nm/s, with the As_2 and Ga fluxes set for a beam equivalent pressure ratio of 10:1 [4.31]. The growth temperature were set at either 460 °C or 525 °C, , which are both in the temperature range in which the c(4x4) surface reconstruction occurs on GaAs(001).

4.1.2 Experimental Comparison of Growth on Patterned GaAs(001) Substrate with kMC Simulations

Previous work by Tadayyon-Eslami et al. explored the effect of lithographically patterning GaAs(001) surfaces on the subsequent topography which evolves as more GaAs is deposited, i.e. "homoepitaxial growth". In her work, she used photolithography followed by etching to create patterns in which the dimensions and spacings of the pits were microns, much larger than the nanometer scale structures we explored in our simulations. Nevertheless, these experiments produced interesting results which suggested that a small Ehrlich-Schwoebel barrier is present on these surfaces, at least for steps of a certain orientation. Specifically, on these "micro-patterned" surfaces we found that depositing Ga and As_2 (the latter in excess) at a temperature of 540 ºC and a rate of 1 monolayer per second results in the formation of mounds selectively at the edges of pits along [110] directions [4.3]. At these length scales, the pits are apparently too far apart to result in formation of ordered mound arrangements between them. In this thesis, we have implemented electron beam lithography to make structures whose dimensions and spacings are much smaller, approaching those used in the simulations.

Fig. 4.1 shows a series of atomic force microscopy maps of the topography which results from GaAs growth on such nanopatterned (001) surfaces at two different temperatures. At the lower of the two temperatures, 460 ºC, individual mounds span bridges between neighboring pairs of nanopits separated along [110] directions, ("[110] two-fold bridges").

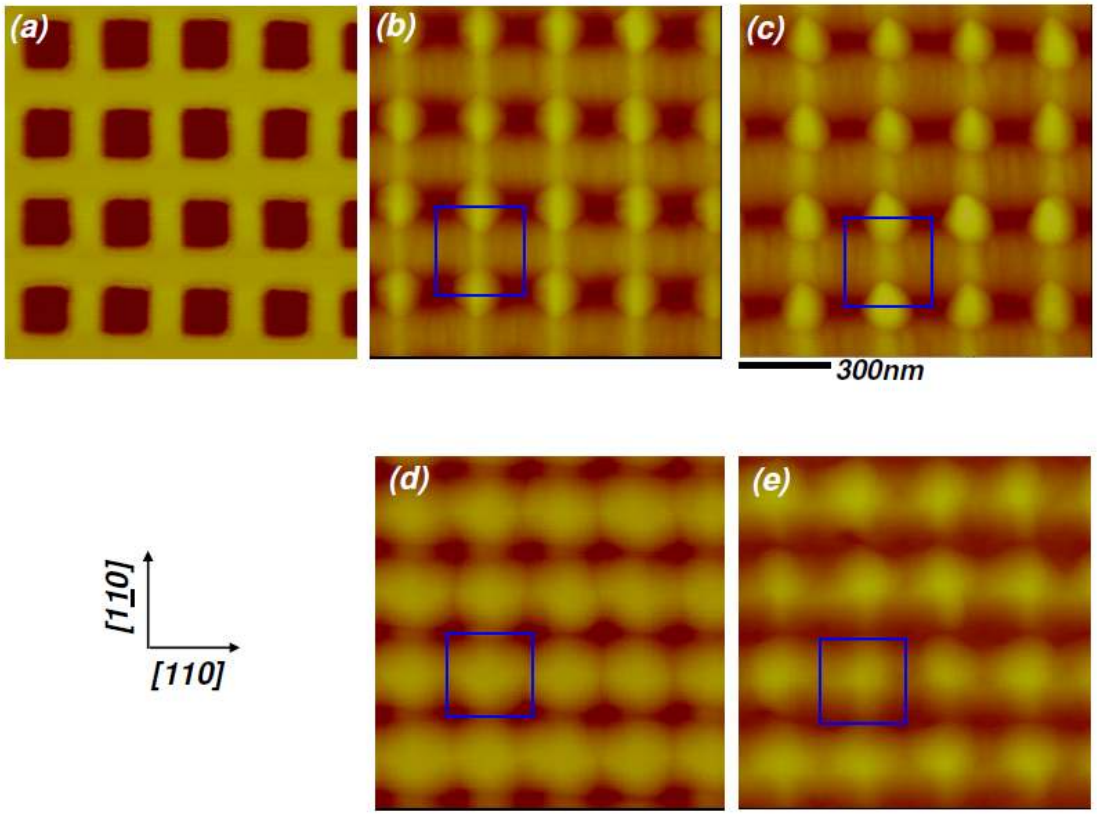

Fig. 4.1: Mound structures during growth of GaAs on nanopatterned surfaces.

(a) Atomic force microscope image of topography of patterned GaAs(001) before growth. Pits are 30 nm deep, 150 nm wide and spaced at A = 300 nm. (b) AFM image after growth of 60 nm of additional GaAs at 460ºC. The blue square shows the unit cell of the initial square pattern. (c) After growth of 100 nm at 460ºC. (d) After growth of 30 nm, at a temperature of 525ºC. (e) After growth of 60 nm at 525ºC.

It is at these same sites that mounds form in the second ordered arrangement, $A/\sqrt{2}$ x $A/\sqrt{2}$ structure, in the simulations for the first pattern geometry discussed above (Fig. 3.4(f)). A difference is that the mounds which form at the centers of the two-fold bridges along [110] directions in the simulations are missing in the experiments. The GaAs(001) surface, in fact is not 4-fold symmetric: both the Ga diffusivity [4.10,4.11] and adatom-step sticking probabilities [4.26] are different along [110] and [$\underline{1}$10], as is the geometry of steps running along [110] ("B-type") and [$\underline{1}$10] ("A-type") for both the c(4x4) [4.10] of interest here and the β_2(2x4) reconstruction [4.22-4.26] which occurs above ~550 ℃ [4.3, 4.32]. In addition, earlier results by Tadayyon et al. on micropatterned GaAs(001) suggested the presence of a finite Ehrlich-Schwoebel barrier along [110] but not obviously along [$\underline{1}$10]. Even more striking is the observation after increasing the experimental growth temperature to 525 ºC. In this case mounds again form at the centers of the "four-fold bridges" i.e. between the corners of quartets of nanopit neighbors, and lead to the same A x A structure seen at the higher temperatures in the simulations (Fig. 3.4(g)). Additional preliminary experiments at lower temperatures than those explored here is shown in Fig. 4.2; the experimental results look more complicated than the A/3 x A/3 structure we saw in kMC simulations.

In Figs. 4.2(a)-(c) we show three different modes of directing high density assembly of mounds with different length scales and shapes of the initial pattern at the growth temperature of 300 ºC. In each case, we have grown 40 nm of GaAs on top on the nanopatterned GaAs(001) surfaces. It is clear that the arrangements of mounds are sensitive to those pattern parameters as we mentioned earlier. However,

in these preliminary lower temperature growth experiments on patterned GaAs(001) substrates, we indeed see qualitative agreement of forming much higher density of nanostructures decorating the surfaces, and being directed by the predefined patterns.

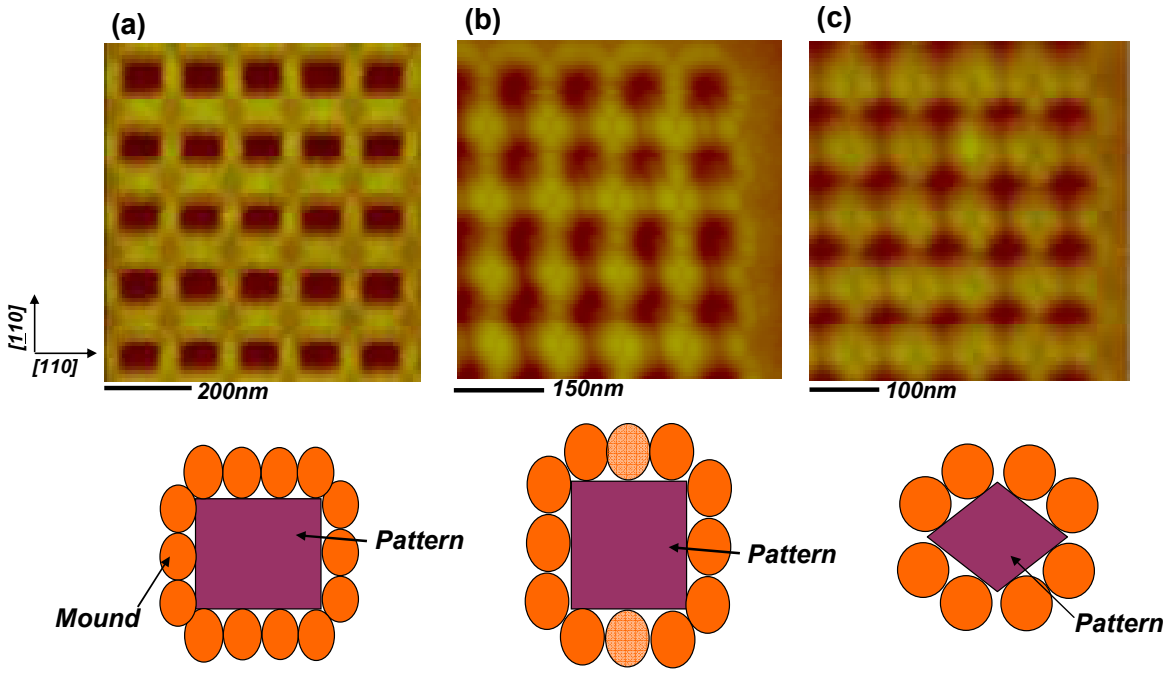

Fig. 4.2: High density mound structures formed with lower growth temperature *(a) -(c) top: atomic force microscope images of topography of patterned GaAs(001) after 40nm of GaAs grown on top at temperature of 300℃, which the spacings of pattern arrays are 200 nm, 160 nm and 120 nm respectively. Bottom: the schematics of various high density mound structures directed by patterns with different lateral sizes.*

4.1.3 Evolution During Growth at 525 ℃

In experiments, we observe more complicated structures and evolution as we track the morphologies as a function of growth thickness. In Fig. 4.3, we show a series of AFM images of surface morphologies of patterned GaAs(001) after growth at 525 ℃. We characterized the surfaces by AFM at four growth stages: after growth

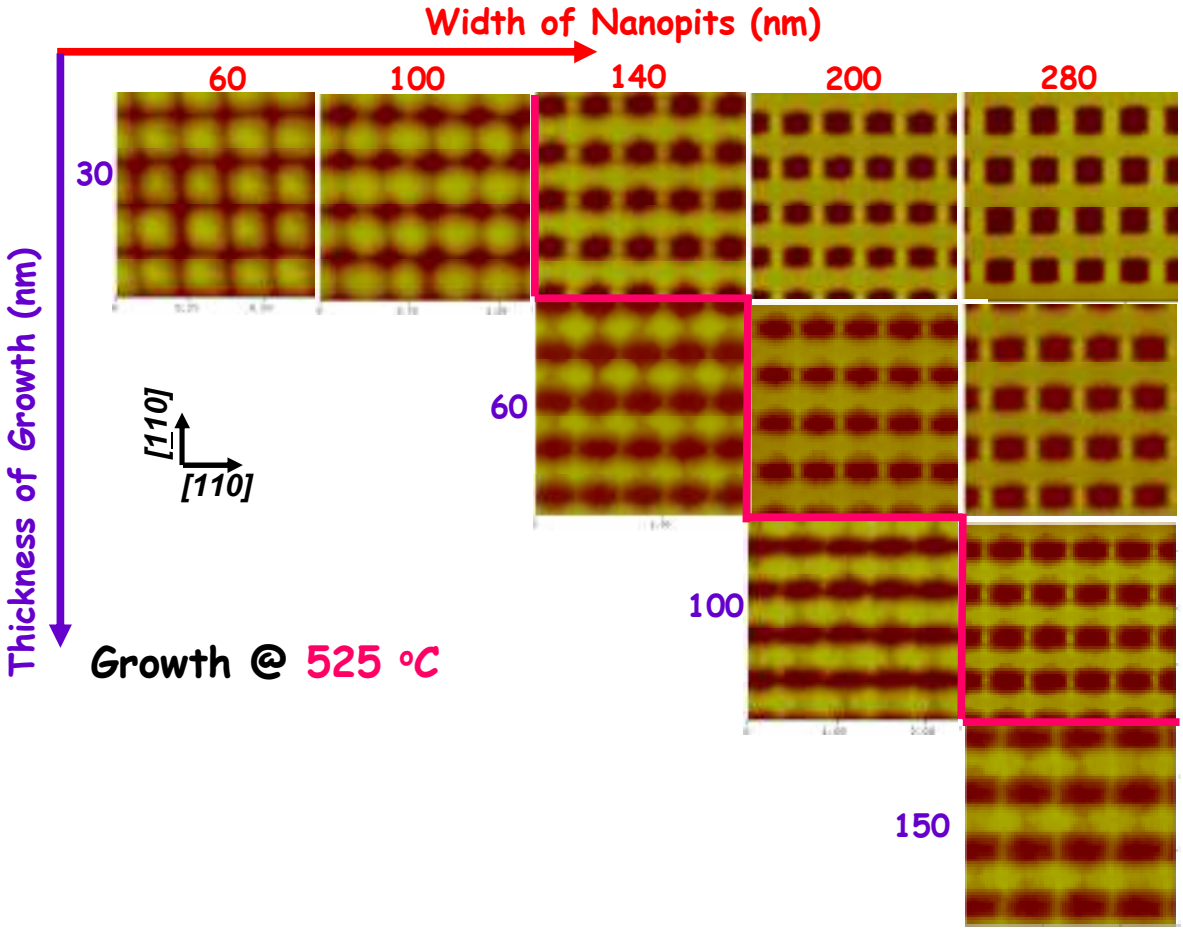

Fig. 4.3 *A series of AFM images for varying initial widths of nanopits (the size increases from left to right, the pitch is twice the initial width), and for different thickness of growth (the growth thickness increases from top to bottom). The growth temperature is 525 ℃.*

of GaAs layers of 30 nm, 60 nm, 100 nm and 150 nm average thickness. Along the horizontal direction, we show the grown surface profiles with fixed average growth layer thicknesses for varying nanopit patterns. The initial widths of the nanopits are varied from 60 nm to 280 nm from left to the right; along the vertical direction, the grown layer thickness varies from 30 nm to 150 nm from top to bottom. At the earliest stages of growth shown here, i.e. for the 30 nm average film thickness, for the smaller width nanopits, (i.e. 60 nm or 100 nm wide) we see that mounds have formed at the centers of "4-fold bridge sites", i.e. at sites between quartets of neighboring pits. This agrees with the predictions of our kMC calculations discussed in chapter three -- for the highest temperature, " 1 x 1" mound phase. However, for larger nanopit patterns, those for 140 nm or larger initial width, , we see that the mounds have instead formed at the 2-fold bridge sites after growth of 30 nm of GaAs. We track the evolution of surface morphology by scanning at the same area of the surface after thicker growth layers. After 60 nm we see that the mounds which initially formed at the 2-fold bridge sites decay in height, and that mounds at the 4-fold bridge sites begin to dominate the surface topography. This amounts to a "kinetic transition" from mound assembly in in 2-fold bridges sites to mound assembly in 4-fold bridge sites. As seen in fourth and fifth columns in Fig. 4.3 such a transition occurs for larger nanopit patterns as well, The zigzag line-segments in Fig. 4.3 marks the approximate kinetic phase boundary separating the two regimes; AFM images images above and to the right of this show the formation of mounds at 2-fold bridge sites, while images below and to the left show the formation of mounds at 4-fold bridge sites. Overall our results at this temperature show that mounds form at the 2-

fold bridge sites at the earlier stages of growth, then the surfaces evolve during growth and display a transition to a structure containing mounds at 4-fold bridge sites at later stages of growth, with the transition occurring at a thickness which increases monotonically with the spatial period of the pattern; for the smallest nanopit patterns, i.e. with initial widths of 60 nm and 100 nm wide nanopits, apparently the transition occurs a stage of growth, less than 30 nm thickness .

4.1.4 Evolution During Growth at 460 ℃

In the last section we described our observations of a very interesting evolution of surface morphologies for growth at a temperature just slightly below that at which Tadayyon, et al. observed a change in the mode of unstable growth on patterned GaAs(001) [4.3]., An obvious question concerns the effect of lowering the temperature yet further. To address this we carried out additional growth experiments using the same procedures as we described in the last section, but using a lower growth temperature of 460 ℃.

In Fig. 4.4, we show a summary of surface profiles as functions of the sizes of nanopits and the total growth thickness at the growth temperature 460 ℃. The dominant features for average grown-layer thicknesses less than, and pattern periods greater than those indicated by the zig-zag line are once again mounds at the 2-fold bridge sites, while for thicknesses beyond this and periods below this the dominant features are mounds in the 4-fold bridge sites.

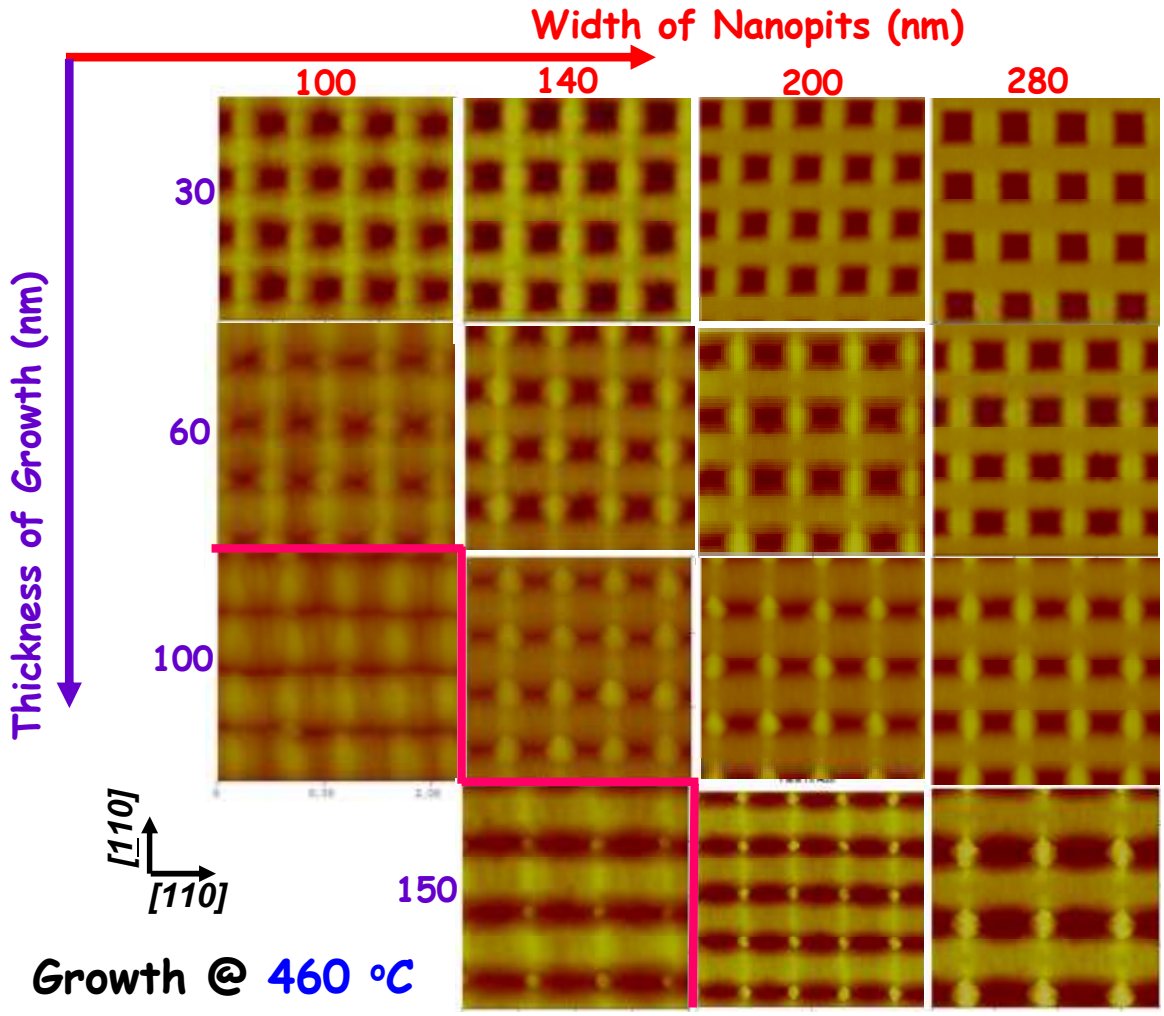

Fig. 4.4 *A series of AFM images for different initial widths of nanopits (the size increases from left to right, the pitch is twice the initial width), and for different thickness of growth (the growth thickness increases from top to bottom). The growth temperature is 460℃.*

Comparing with Fig. 4.3, i.e. the major behavior of surface evolution for these two different growth temperatures is qualitatively the same, but the boundary is shifted toward larger layer thicknesses and smaller periods for the lower growth temperature.

We now examine in more detail the effect of the pattern period, based upon AFM images like those shown in Fig. 4.4. For the larger patterns, i.e. initial nanopits of 200 nm and 280 nm widths, we see the that the mounds initially (i.e. at smaller thicknesses) appear as a pair of ridges around pit edges along [110]. This is qualitatively consistent with observations reported by Tadayyon [4.3] for growth experiments at 540 ℃ for GaAs(001) surfaces patterned with arrays of pits in which the characteristic sizes and spacings were microns. With thicker layers, we see instead single mounds at the centers of 2-fold bridge sites. The coalescence evidently occurs at film thicknesses which increase with spatial period, and thus is expected to will occur beyond the growth thickness we pursued here for the larger period patterns. .

For both of the growth temperatures reported on above, we observed a intriguing transition of the dominant sites for mound formation as we growth thicker films on top of the patterned surfaces. In the next few sections we probe the mechanisms that drive this transition through further quantitative analysis. .

4.2 Observation of Self-Limiting Growth

In this section we carry out a careful analysis of the growth experiments done at 460℃; since the surface evolves slower at this lower temperature it is easier to capture more details during surface evolution.

In Fig. 4.5, we show a series of AFM images as a function of growth thickness on a nanopatterned GaAs(001) surface with an initial pit width of 140 nm and a spatial period of 280 nm. These images have a relatively large field of view that includes the entire patterned area and the surrounding unpatterned parts of the surface. We measured height profiles from these images along the [110] orientation (red dashed line) cutting across both the 2-fold bridge sites and the bottoms of pits; these are shown in Fig. 4.6.

In Fig. 4.6, these profiles show that at the early stage of growth, i.e. after 30 nm, the local growth fronts at 2-fold bridge sites surpass that at the unpatterned areas. At a later stage, i.e. by an average film thickness of 100 nm, the growth fronts at some of the 2-fold bridge sites have been surpassed by the front at the unpatterned areas. Beyond this point, i.e. by a grown thickness of 150 nm, the fronts at all 2-fold bridge sites have fallen far behind that of the unpatterned regions. This is not a simple relaxation of patterns: we do not see typical sinusoidal shapes of line profiles, as might be expected if the evolution followed that predicted by a diffusion equation. On the contrary, we still see the sharp, cusp-like features at the top of 2-fold bridge sites. Seemingly, the growth fronts at 2-fold bridge sites at certain point cease, i.e. locally the surface stops growing; these regions are surpassed by the growth fronts of

the surroundings and the unpatterned regions. This is evidence for a 'self-limiting growth' behavior of mounds at these 2-fold bridge sites.

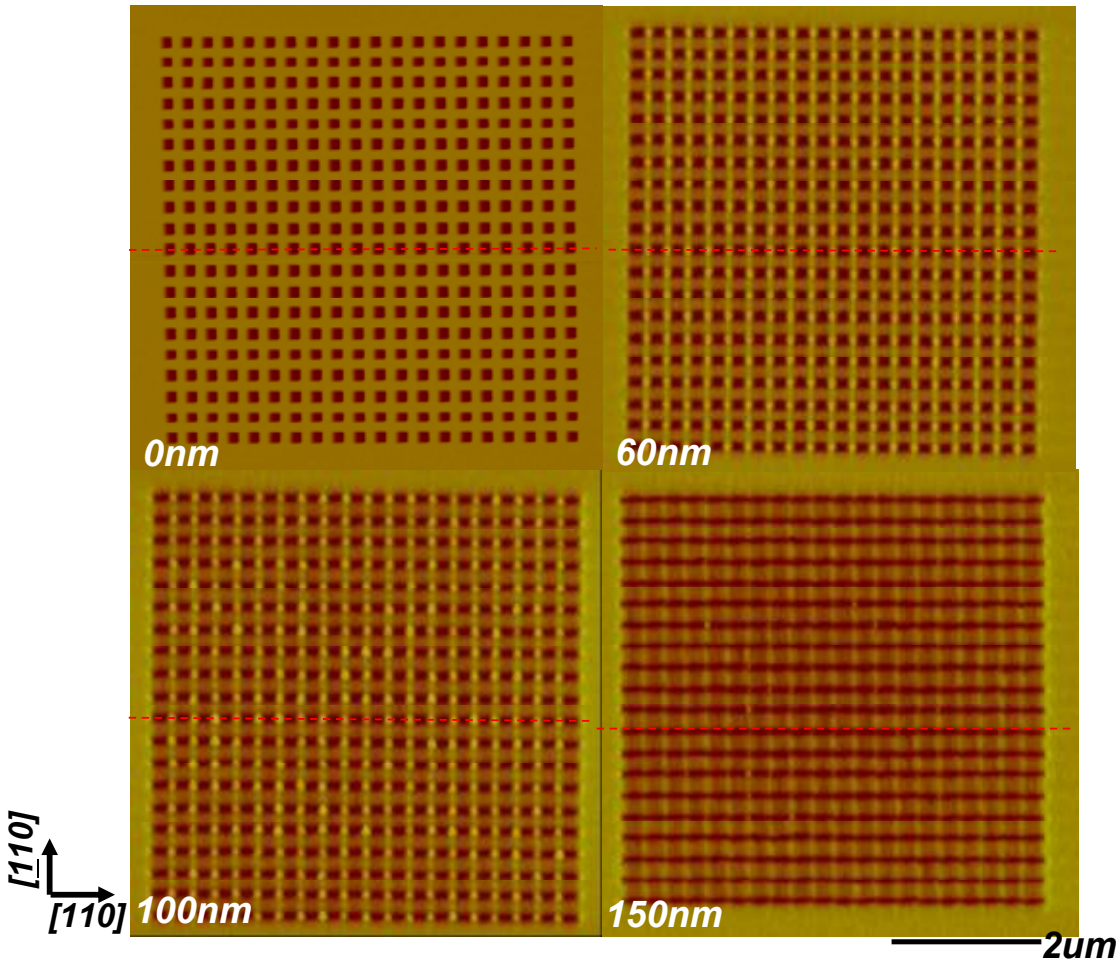

Fig. 4.5 *Large field of view of AFM images of nanopatterned GaAs(001) topography ,including both patterned and unpatterned parts of the surface, before growth and after homoepitaxial growth of 60 nm, 100 nm and 150 nm. Initial nanopit widths w =140nm; center-center spacing between nanopits = 280 nm; growth temperature = 460 ºC; growth rate = 0.28 nm/s.*

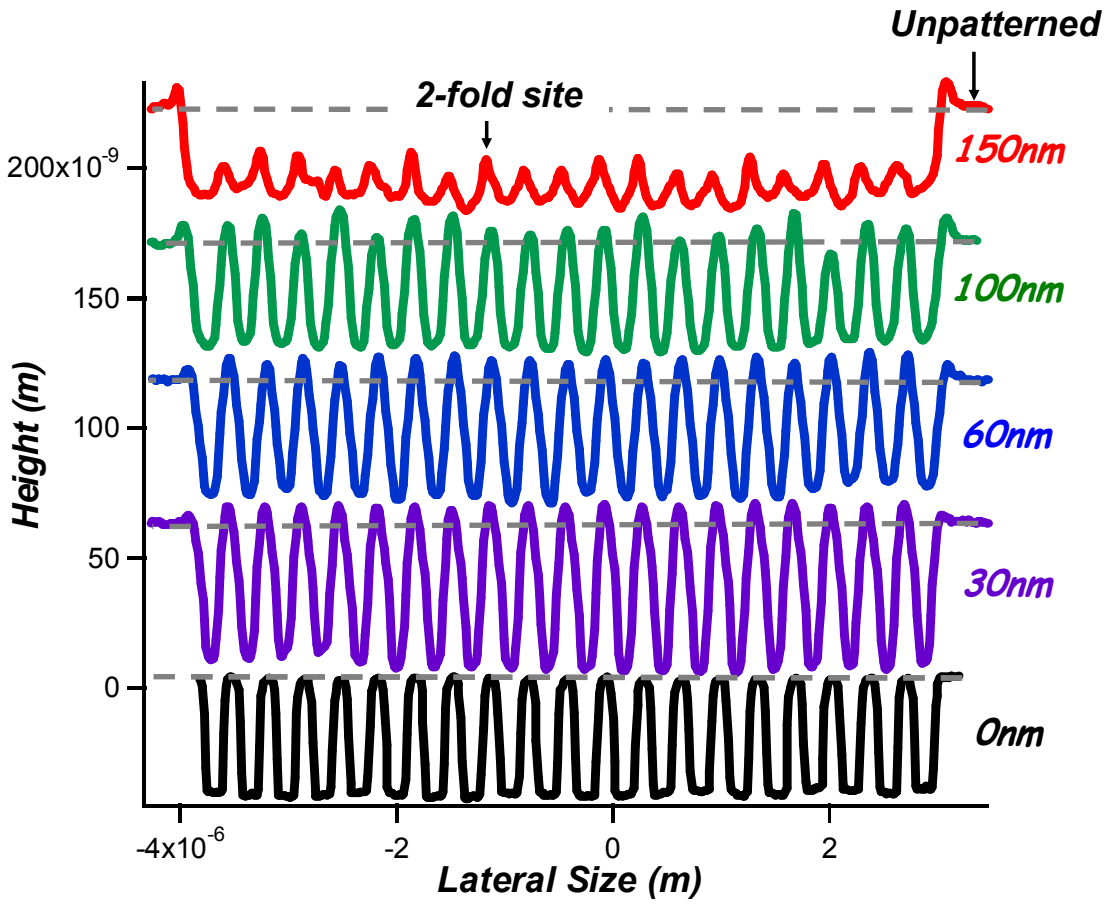

Fig. 4.6 *Measured height profiles from AFM images presented in Fig.4.5, taken along [110] and cutting across 2-fold bridge sites and the bottoms of nanopits, as indicated by red dashed line in Fig. 4.5.*

We next consider more details of the growth on a nanopatterned surface at 460 ℃, including further evidence of self-limiting behavior of mounds based upon a series of "zoomed-in" AFM images , and height profiles, in this case measured

along the [110] orientation (indicated by green dashed lines in Fig. 4.7), cutting across the bridges between nanopits. These are presented in Figs. 4.7 and 4.8.

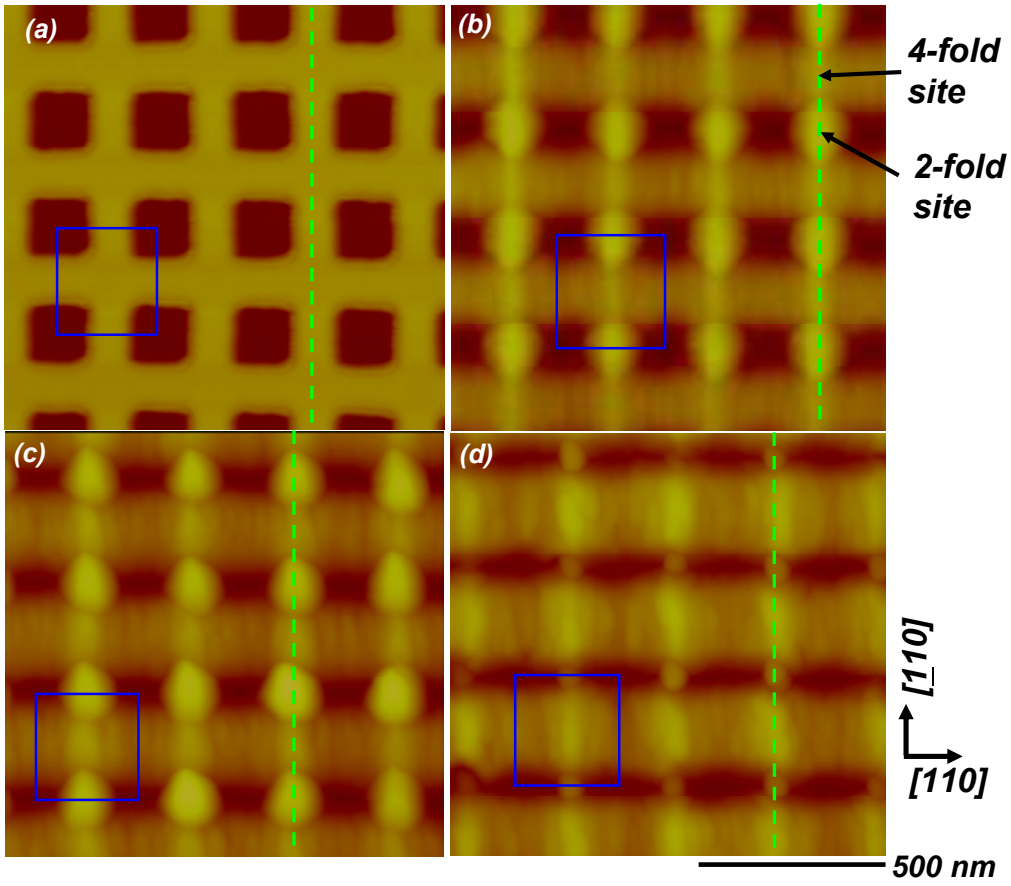

Fig. 4.7 *AFM images of nanopatterned GaAs(001) topography before and after homoepitaxial growth: (a) before growth; (b) after growth of 60 nm; (c) after growth of 100 nm; (d) after growth of 150 nm. Initial nanopit widths w =140nm; center-center spacing between nanopits = 280 nm; growth temperature = 460 ℃; growth rate = 0.28 nm/s. Blue squares show a pattern unit cell.*

The starting topography is shown in Fig. 4.7 (a), and subsequent panels show the topography which results from the growth of films of thickness (b) 60 nm, (c) 100 nm and (d) 150 nm. Due to the anisotropies of the GaAs(001) surface reconstruction, diffusion coefficients and adatom sticking probabilities, the evolution of nanopits is different along [110] and [$\underline{1}$10] [4.10- 4.13]. The AFM images show a broadening of nanopits and thus a narrowing of the "bridges" between them along [110]. The nanopit widths along [$\underline{1}$10] show the opposite behavior, i.e. a narrowing during epitaxial growth. At early stages of growth, as seen in Fig. 4.7 (b)-(c) mounds self-assemble at the centers of bridges between near-neighbor nanopits along [110], which are at the 2-fold bridge sites. Our previous results in chapter three suggest that this is due to the combined effect of Ehrlich-Schwoebel (ES) barriers along [110]-oriented steps [4.3- 4.5] and a reduced nucleation barrier at the corresponding pit edges [4.2, 4.17], and we will have further discussion later in this chapter.

The evolution of the mounds during growth can be tracked in Fig. 4.8, which shows a series of height profiles along the path indicated by the green dashed line in Fig. 4.7. This set of line profiles allow us to compare the growth fronts at 2-fold bridge sites, 4-fold bridge sites and the unpatterned areas. Again, at early stages of growth, the mounds forming at the 2-fold bridge sites dominate the surface profiles. However, at later stages of growth, between 100 nm and 150 nm, a sharp change in the evolution of the surface morphology occurs: while before this point the mounds at 2-fold bridge sites grow and sharpen, after this they are surpassed by mounds at 4-fold bridge sites, i.e. between quartets of neighboring nanopits. Thus, we find the mounds at 2-fold bridge sites 'self-limit' at certain point, and this behavior results in

the 'transition' between mound structures with different dominant sites relative to the underlying pattern we described earlier in this chapter.

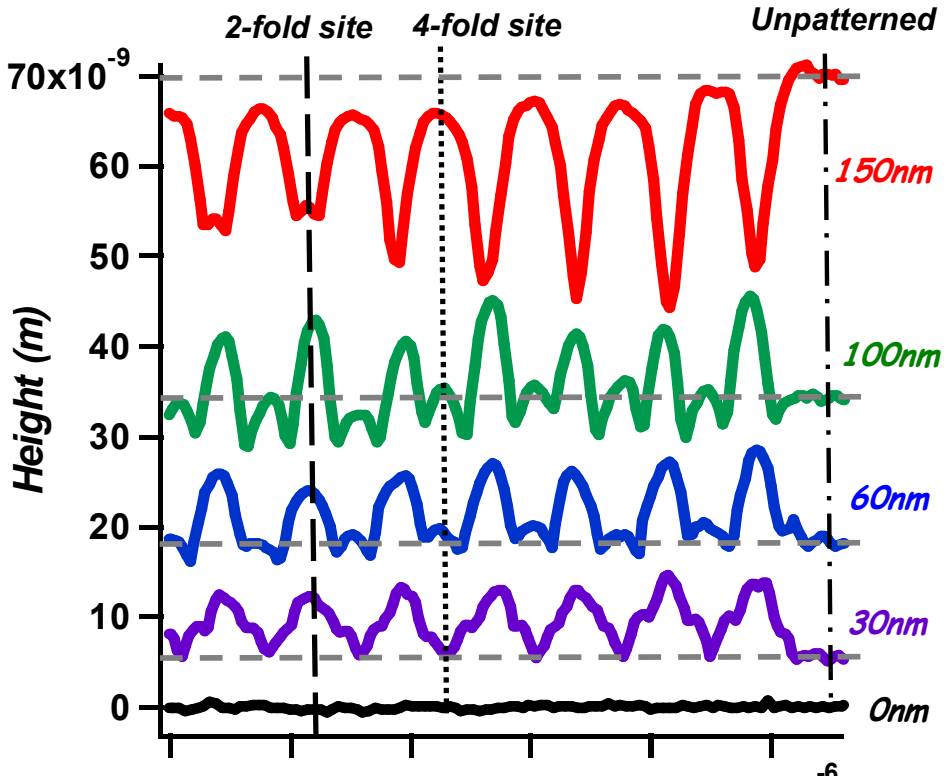

Fig. 4.8 *Measured height profiles from Figs.4.7(a)-(d), taken along [1̲10] across bridge sites, as indicated by green dashed line in Fig. 4.7.*

4.2.1 Quantitative Height Analysis of Growth

In this section we quantify the of self-limiting growth behavior, measuring the mound heights as a function of average layer thickness. A first interesting question that arises in tracking the height of the mounds during growth is what to use as a

reference level; since during growth, in principle the entire surface is propagating. There are at least two ways of measuring it, which we consider below. In Fig. 4.9 (a) we summarize the heights of mounds at 2-fold and 4-fold bridge sites, relative to the bridges on which they form, for growth on a 280 nm period pattern. Consistent with the height profiles of Fig. 4.8 the height of mounds above 2-fold bridge sites (depicted here by solid triangles) reaches a maximum at a film thickness of approximately 100 nm, beyond which it decays, and is surpassed by the height of mounds at 4-fold sites (depicted by solid squares) which do not yet decay.

On the other hand, since the nanopit arrays are of finite size, it is instead possible to measure the mound heights relative to the unpatterned, surrounding surface, with somewhat different results. This behavior can be seen in Figs. 4.5-4.6, for which the AFM images are sufficiently broad so as to include both the patterned and surrounding unpatterned parts of the surface. For finite-sized patterns, it is seemingly preferable to measure the height of mounds relative to the unpatterned areas, as this reference level can be common for the height measurement for various sites on the surfaces. The results of such a measurement are shown in Fig. 4.9 (b); the heights of mounds at both 2-fold bridge sites (depicted by open triangles) and 4-fold bridge sites(depicted by open squares), relative to the unpatterned surface both reach maxima after growth of a smaller average film thickness in this case, approximately 60 nm, beyond which they decay relative to the unpatterned areas as we grow thicker films. Presumably the self-limiting growth behavior initiates as the height reaches a maximum, and results in a decreasing relative height, which eventually becomes negative relative to the reference level.

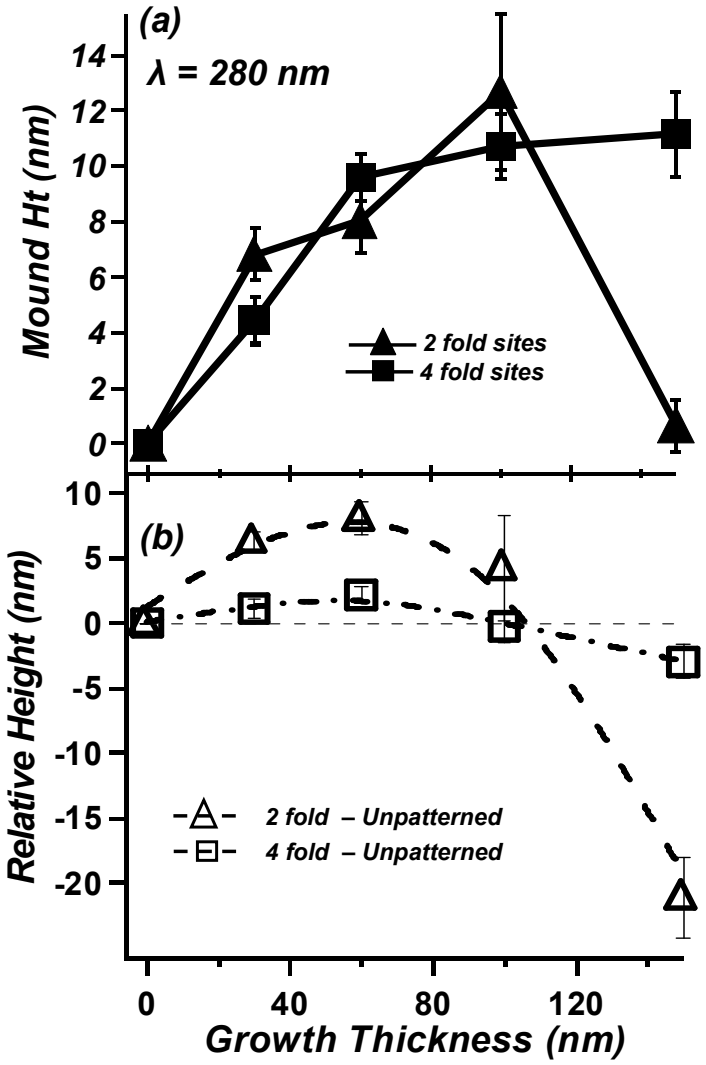

Fig. 4.9 *Mound evolution for array with spatial period = 280 nm; (a) Mound heights vs. grown thickness, measured above local bridges on which they form; (closed triangles) mounds at 2-fold bridge sites; (closed squares) mounds at 4-fold bridge sites. (b) Mound heights vs. grown thickness, measured above the unpatterned part of the surface; (open triangles) mounds at 2-fold bridge sites; (open squares) mounds at 4-fold bridge sites.*

4.2.2 Growth Rate Analysis

A somewhat different way to quantify this behavior, which we consider here, is to track the relative growth velocity of various sites on the surface. In Fig. 4.10 we plot the growth rates of the heights of three different features, relative to that of the surrounding unpatterned surface, and normalized to the average growth rate: these are for the mounds at 2-fold bridge sites (dashed curve), mounds at 4-fold bridge sites (dashed-dotted curve) and the pit bottoms (dotted line).

Early on, the local growth rate at mound sites is greater than the average growth rate, while that at pit bottoms is below the average. Such a difference leads to an initial amplification of the pattern corrugation during the early stage of growth. By a film thickness of 60 nm, at which point the analysis of the relative height (Fig. 4.9 (b)) showed that the self-limiting growth of mounds initiates, the local growth rate falls behind that at both the reference level and at the pit bottoms. Strikingly, coincident with this, the growth rate at the pit bottoms reaches a maximum, and exceeds that of the reference. The pattern corrugation amplitude in this regime decays. We thus observe a transition from the amplification of the patterns to decay of the patterns, in agreement with the results of Tadayyon et al., Kan et al., and Shah et al. [4.3, 4.14- 4.16]. In that earlier work the initial understanding was based on phenomenological models; the analysis and observations presented here strongly suggest a much more physical understanding: ***the self-limiting growth of mounds is relevant and, at least in part, responsible for the transient amplification of the topographic patterns during growth on GaAs(001).***

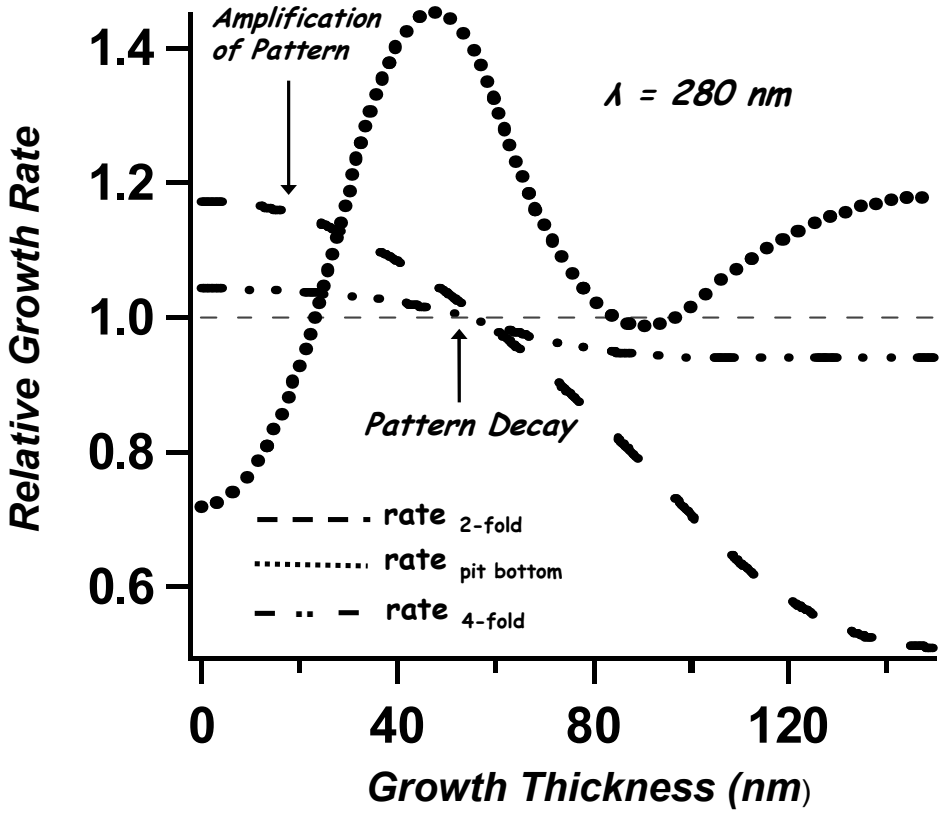

Fig. 4.10 *Growth rate, relative to, and normalized to that of the reference level, defined as that unpatterned region of surface of mounds; results are for: mounds at 2-fold bridge sites(dashed line), mounds at 4-fold bridge sites(double dot-dashed line), nanopit bottoms(dotted line).*

4.2.3 Evidence for a Critical Top Terrace Width

In the previous sections, we analyzed the results of growth on nanopit arrays with spatial period of 280 nm to demonstrate the "self-limiting" behavior of mounds on these surfaces. We find this behavior to be general: we observe such self-limiting behavior on nanopit arrays with other spatial periods as well, occurring for different amount of growth thickness, as summarized in Table. 4.1.

Width (nm) of nanopits	**Spacing (nm) between nanopits**	**Thickness (SLG occurs, nm)**
100	*200*	*30*
140	*280*	*60*
200	*400*	*100*

Table 4.1 *Self-limiting growth (SLG) we observe on nanopit arrays with different spatial period for growth at 460 ℃. SLG occurs at thicker growth for larger spatial periodicity of nanopit arrays.*

A remaining question is what is the physical mechanism behind the self-limiting growth behavior? A plausible explanation, based on observations that the mounds sharpen before self-limiting, is that self-limitation comes from the existence of a minimum terrace width, beneath which further islands do not nucleate. In Fig. 4.11 (a), we plot the apparent top terrace width as a function of growth thickness based on

measured height profiles across 2-fold bridge sites. The analysis shows a minimum size after growth of 60 nm, i.e. coincident with the initiation of self-limiting behavior shown in Fig. 4.9 (b) from the height analysis . This is added evidence that reaching the minimum top terrace width causes the observed self limiting growth of mounds.

Fig. 4.11 (b) shows a histogram of apparent apex terrace widths, measured at the minimum shown in top terrace width distribution, e.g. after 60 nm growth in Fig. 4.11(a). This histogram is based on the statistics that we measured the apex terrace widths of mounds formed on various spatial periods of nanopit arrays that exhibit self-limiting behavior, which are the mounds described in Table 4.1. Interestingly, the histogram exhibits a distribution of widths, with a peak value of 45-50 nm for the critical terrace size. This is undoubtedly an overestimate, and sets an upper limit for the critical width, as it includes the convolution with a fairly blunt AFM probe. Deconvolution of the point spread function, using the manufacturers range of tip radii of 20 ± 10 nm would yield a value of 23 ± 23 nm, a range which includes a width as small as a single unit cell.

Intuitively one might expect the critical terrace width to be small, perhaps on the order of a one, or a few unit cells of the GaAs(001) - c(4x4) reconstruction. Indeed a plausible hypothesis is that this effect related to "reaction limited island nucleation" of compound semiconductors during MBE growth, as proposed by Kratzer et al., [4.18, 4.19]. Specifically, in this picture the incorporation of a new layer of GaAs into the solid would be prevented once the top terrace width is too small to have a finite probability for island nucleation to occur. Island nucleation involves multiple

species (Ga adatoms, As_2 molecules) adsorbed in sequence, along with selection of sufficiently strong absorption sites and surface geometry.

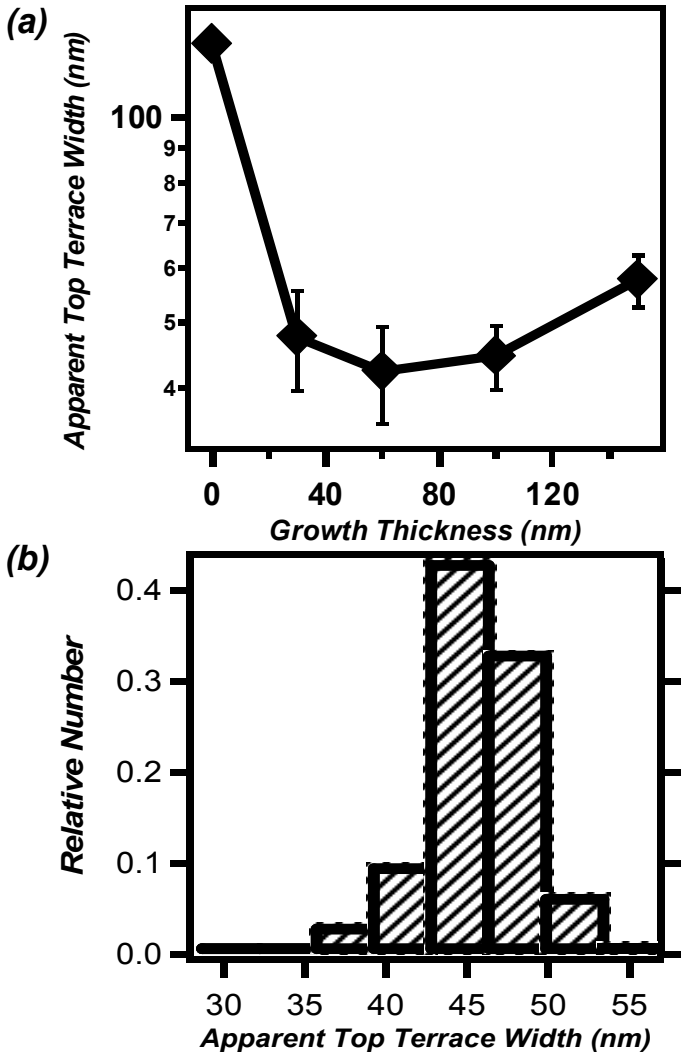

Fig. 4.11 *(a) Measured widths of the topmost terrace width for mounds at 2-fold bridge sites, measured along [110]. (b) Histogram of measured topmost terrace widths is measured at the growth thickness corresponding to the minimum in (a) and that of other pattern periods described in Table 4.1.*

A second possible mechanism, proposed by Giesen et al. [4.20], is that the Ehrlich-Schwoebel barrier might vanish due to quantum confinement effects of electronic states on the surface if the top terrace width drops below a certain critical size. The vanishing of the ES barrier at the apexes of mounds would increase the probability of interlayer mass transport from the top of the mounds to the pit bottoms, reducing the probability of island nucleation growth at the apexes, and initiating self-limiting behavior. Distinguishing between these, and other possibilities, require further investigation.

4.3 Understanding of the Sequence of Nucleation Sites on Patterned GaAs(001)

In our previous results, we observed a sequence of dominant mound formation sites on patterned GaAs(001) surface: the mounds form at 2-fold bridge sites first, self-limit and eventually are dominated by the mounds at the 4-fold bridge sites. Below we try to understand the reason for this sequence of mound formation.

Seemingly this sequence might be explained if a peak in adatom concentration occurred at 2 fold bridge sites initially, and once those mounds form, a secondary peak of adatom concentration occurred at the 4-fold bridge sites.. This is based on the notion that mound formation is most likely at regions of high adatom concentration. In order to check this hypothesis, we carried out numerical solutions of the diffusion equation to calculate the adatom concentration on patterned surface, in the absence of, and in the presence of Ehrlich-Schwoebel barrier, as discussed in section 3.5.

However, this analysis showed that whether an Ehrlich-Schwoebel barrier is present or not, the adatom concentration is always higher at the 4-fold bridge sites, not the 2-fold bridge sites. This is shown again in Fig. 4.12 (a) and (b) (it was shown earlier in Fig. 3.16). Furthermore, in Fig. 4.12 (c) and (d), we show the results of adatom concentration of the surface with an adatom sink, i.e. an existing island nucleated at the 4-fold bridge sites. The results show that only when there is an existing mound at the 4-fold bridge sites, the adatom concentration reaches a maximum near the 2-fold bridge sites; this is so whether there is Ehrlich-Schwoebel effect or not. This behavior is the opposite of what we would expect based upon our

experiments. We conclude that it is not the adatom concentration that is responsible for determining the dominant mound formation sites.

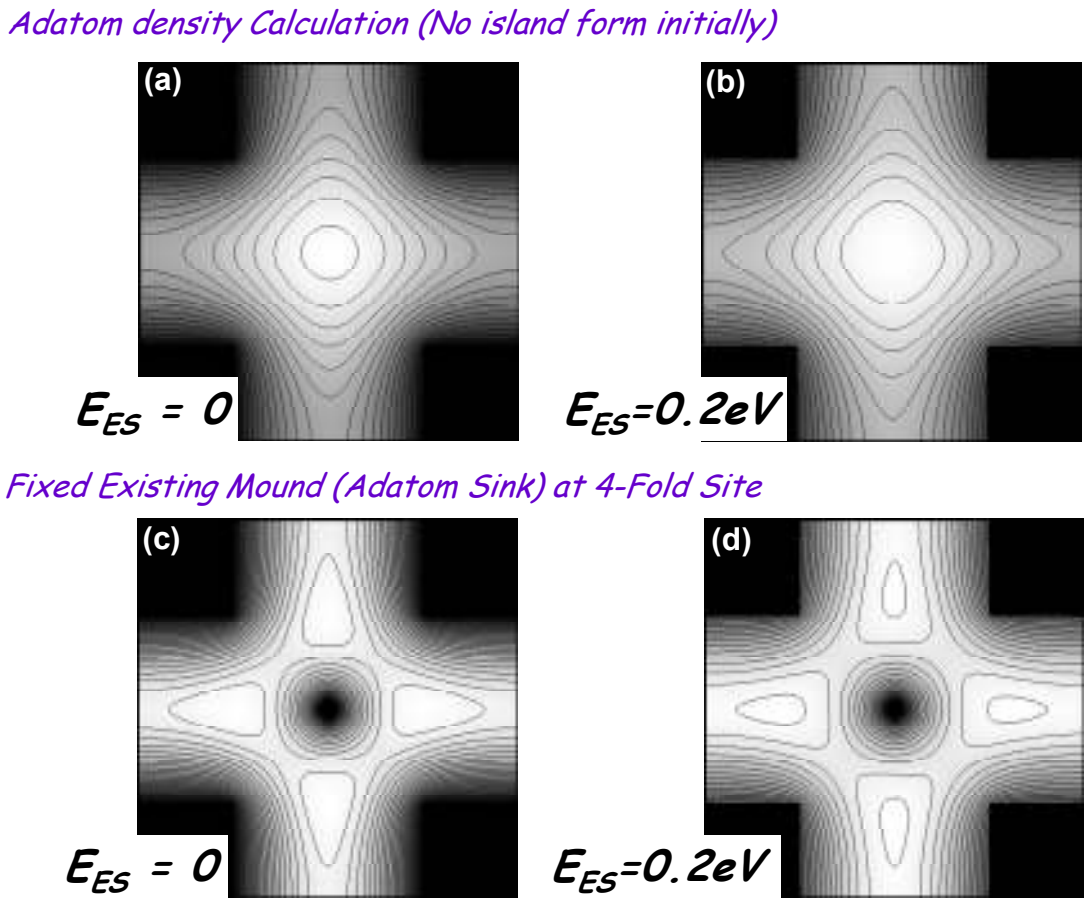

Fig. 4.12 *Simulations of local density of adatoms by diffusion equation (a) with Ehrlich-Schwoebel (E_{ES})=0 eV; (b) with E_{ES} =0.2 eV, both (a) and (b) have no nucleated islands formed yet; (c) with E_{ES} =0 eV; and (d) with E_{ES} =0.2 eV, both (c) and (d) show the results after one island formed at 4-fold sites. Bright region: high density; dark region: low density.*

A very plausible explanation based on the above discussion is that the mounds *nucleate at heterogeneous sites*. Based on classical nucleation theory in two dimensions, the energetic cost of nucleation is the perimeter energy, i.e. the free energy (β) per unit length of edges around the mounds:

$$\Delta G = -\Delta G_A A + \int_{perimeter} \beta dl$$

Also from nucleation theory, at certain types of heterogeneous nucleation sites,

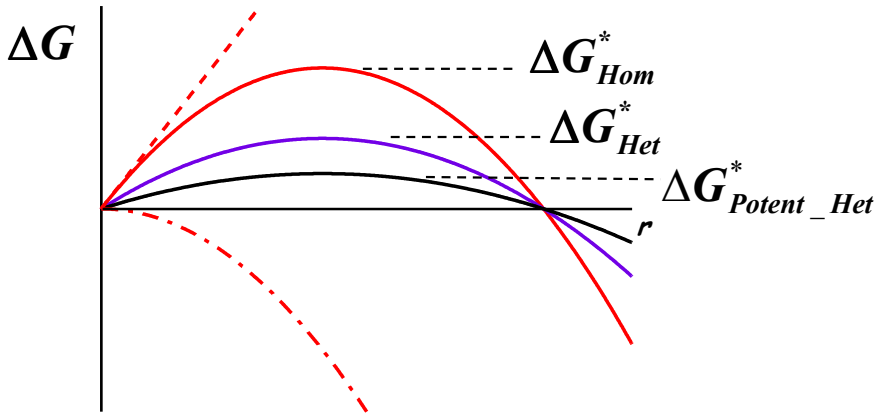

Fig. 4.13 *Schematic of nucleation barriers for homogeneous (red curve), heterogeneous (purple curve) and potent heterogeneous (black curve) nucleation from classical nucleation theory. Dashed curve indicates the energy cost from perimeter energy, and dashed-dotted curve indicates the energy gain of mound formation.*

there is a reduction in the perimeter free energy that causes a reduction in nucleation barrier; Fig. 4.13 illustrates schematically that the nucleation barrier for heterogeneous nucleation (purple curve) is significantly reduced from that for homogeneous nucleation (red curve).

What then is the mechanism for the reduction of the perimeter energy at certain edges of pits? A likely explanation is the formation of a multistep reconstruction. Based upon our observations, this apparently only occurs for steps running

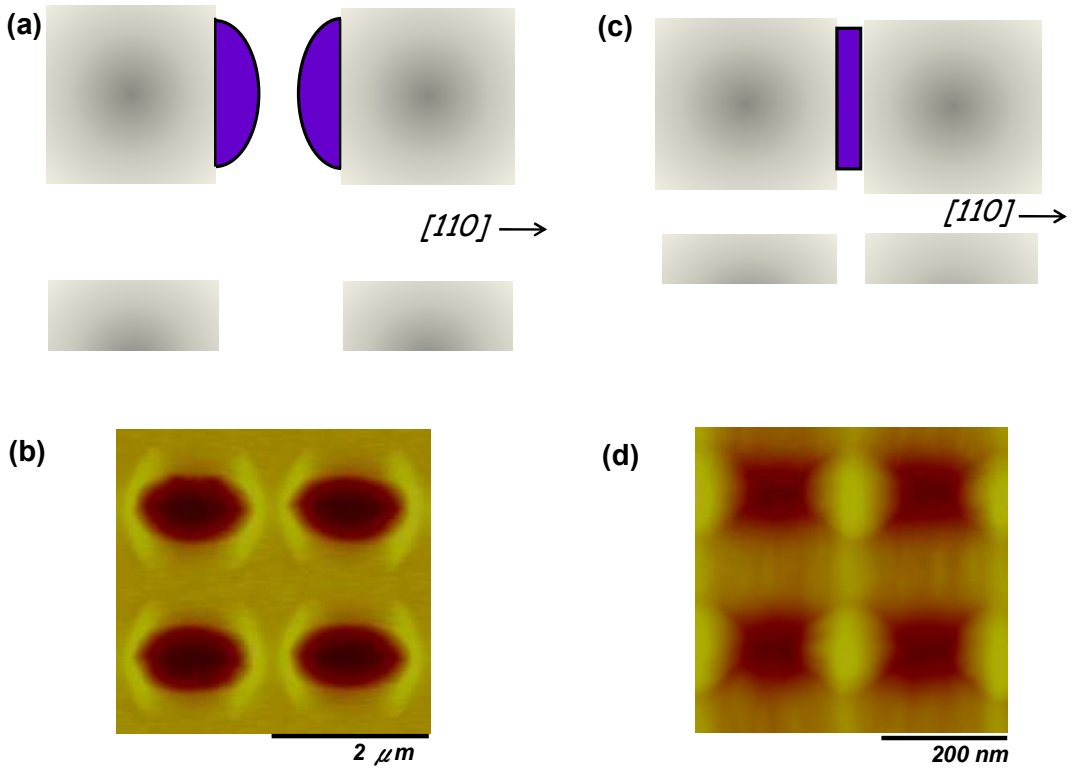

Fig. 4.14 *(a) Schematic of mound formation through heterogeneous nucleation sites. Mounds form as a pair of ridges along certain edges between larger separated pits; (b) Experimental result for micron-size pits; (c) Schematic of mound formation between two nanopits - forming a single mound; (d) Experiment result for nanopits.*

perpendicular to [110]-type directions, but not perpendicular to [$\bar{1}$10]-type directions. Indeed GaAs(001) is a 2-fold symmetric, not a 4-fold symmetric surface [4.10, 4.22-26]. As illustrated in Fig. 4.14 (a) and (b), this idea explains both the anisotropy of forming mounds only along [110] orientation around micron-size pits that Tadayyon et al. reported earlier [4.3] as well why we only see a single mounds at 2-fold bridge sites for patterns of nm length scales. In Fig. 4.14 (c) we show a schematic illustrating the idea that as these pits get close together, the critical size of these mounds is large enough to simultaneously take the advantage of the reduction of perimeter energy at two adjacent pits, reducing the nucleation barrier further (as the black curve shown in Fig. 4.13) and making 2-fold bridge sites even more potent for the nucleation of mounds. For comparison we show an AFM image of such mounds on a nanopatterned GaAs(001) surface in Fig. 4.14 (d). Finally, we point out that the 4 fold bridge sites are seemingly less potent as they only take the advantage of the reduction of nucleation barrier at the corners of those heterogeneous nucleation sites.

This explanation is in good agreement with our experiments, but brings us to a very different picture of mound formation from that suggested by Politi and Villain [4.27, 4.28]. In our model the mound formation is a nucleated process, and not due to the instability on the surface which instead would suggest a formation process akin to spinodal decomposition

4.4 Conclusion

In summary, we have observed intriguing self-limiting behavior of mounds which form on nanopatterned GaAs(001) during growth. We find that growth near 500°C is dominated by formation of multilayer mounds. Evidently island nucleation is faster than the incorporation of diffusing adatoms at steps. Once a mound reaches a self limiting shape, it can apparently only grow further via the slow incorporation from below of atoms at the steps which form its sidewalls. Our observations strongly suggest that a critical, minimum terrace width for island nucleation is an important effect in understanding the transient amplification of pattern corrugation during growth [4.3, 4.14-16]. These observations provide new insights of growth instabilities during epitaxial growth [4.21]. Finally, the sequence of the mounds forming on the patterned surfaces gives us rather direct evidence that the formation of growth mounds on the surface is a nucleated process, rather than an instability.

Chapter 5

Conclusions and Future Work

5.1 Conclusions

In this thesis, we have demonstrated both via kinetic Monte Carlo simulations and by direct MBE growth experiments that it is indeed possible to use a patterned substrate to direct the self assembly of mounds in the presence of a kinetic barrier, the Ehrlich-Schwoebel barrier. We also observe the system lock-in into a series of ordered mound structures, 1/3 x 1/3, $1/\sqrt{2}$ x $1/\sqrt{2}$ and 1 x1 periodicity relative to the underlying pattern periodicity in different temperature windows. We found that the pattern parameters (pit size) and growth parameters (temperature, which defines natural mound size) both affect the direction of growth mounds on the surface. We interpret our observations as evidence for a kind of entropic interaction between the size of patterns and the size of mounds: since mounds don't overhang pit edges, pits reduce the configurations of mound arrangement so that only certain configurations (periodicities) exist. From a technological point of view, it is interesting and

important that the density of mounds in these structures can exceed that of the initial pattern, which demonstrate an amplification of resolution of the patterns we defined. We expect this phenomenon could find application in the fast, controlled assemblies of nanostructures in nanotechnology.

We also found that the persistence of mounds which form on patterned surfaces is limited. The mounds initially form at the 2-fold bridge sites, and after certain amount of growth, these mounds sharpen up and "self- limit"; then they are replaced by the mounds form at the 4-fold bridge sites. We proposed that this "self-limiting" behavior is due to the existence of "critical terrace width" on top of mounds, below which, further islands don't nucleate; then the self-limitng mounds are surpassed by the surrounding interface. The observation of self-limiting growth on GaAs(001) also indicates that the sticking coefficient for atoms to incorporate to steps or sidewalls is rather small since once a mound reaches "self-limit", mounds can only grow further via incorporation of atoms at steps which form its sidewalls, and the incorporation to sidewalls is apparently a slow process. On the contrary, if the sticking coefficient is large or the growth of sidewall is fast, those mounds will probably not show the self-limiting growth of mounds, such as the growth on many metal surfaces. Incidentally, the observation of self-limiting growth gave us the physical mechanisms to understand the transient behavior of pattern corrugation during growth that Taddayon et al. reported a few years ago.

Finally, and perhaps most interestingly, the experimental observation of the sequence of the mound formation sites on the patterned surfaces gives rather direct evidence that the formation of growth mounds on the surface is a nucleated process,

not an instability, as had been suggested earlier by Johnson et al. [1.9] and Politi et al. [1.10]. The most potent heterogeneous nucleation sites, 2-fold bridge sites, take advantage of reduction of perimeter energy simultaneously from the edges of two adjacent nanopits, and the second preferred nucleation sites, 4-fold bridge sites, take advantage of reduction of perimeter energy only at the corners of nanopits. We think a multistep reconstruction formed along certain edges, [110] orientation, of patterns during growth on GaAs is associated with this anisotropic behavior of formation of mounds that we observed.

5.2 Future Work

In this section, we propose possible and interesting future work which could be done to extend our understanding, as reported in previous chapters of this thesis.

1. **Competition between kinetic and strain driven self assembly**

In our investigation, we demonstrated a direction of self assembly of a series of multilayer island or "mound" arrangements, with the relative placement of mounds respect to lithographically-defined nanopits. The placement of mounds is controllable by varying the growth temperature. The direction is driven by a purely kinetic barrier, the Ehrlich-Schwoebel barrier, which is different from many previous works of direction of structures driven by strain effect. A great deal of work over the past two decades demonstrates that in lattice-mismatched systems, Stanski-Krastinov (SK) growth leads to the formation of nanometer scale quantum dots. Hence, it would be extremely interesting to investigate the competition between kinetic and strain effects on the direction of self assembly of structures. What we would like to do next is to experimentally investigate the transition from kinetically to strain - driven self assembly for growth of InGaAs quantum dot structures on patterned GaAs(001).

By varying the In composition of InGaAs layers grown on nanopit patterned GaAs(001) we could probe the competition between the elastic energy that drives quantum dot formation and the Ehrlich-Schwoebel barrier that drives kinetically directed mound self organization. We could measure the topography at various

stages of growth using AFM. We anticipate to observe a transition of formation of kinetic-driven mounds to strain-driven quantum dots as we increase the In/Ga ratio.

2. Build in anisotropy in kMC simulations for comparing with GaAs system

In our kMC simuation, we have adopted a code to demonstrate the growth behavior of an isotropic system, which only gave us qualitative agreement with our growth experiments on the system of GaAs. In order to capture more details of what happens in growth of patterned GaAs, it is necessary to incorporate anisotropy properties in our calculation since GaAs is a 2-fold symmetric crystal. In the modified model, we plan to add the anisotropy of diffusion barrier, bonding energy, sticking coefficient along [110] and [$\underline{1}$10] orientations. We anticipate this new model can reproduce the anisotropy of the mounds shapes and the anisotropy of the evolution of patterns for two orthogonal orientations.

3. Explore the generality of direction of ordered mound arrangements through kinetic barrier - designing experiments of growth on patterned metal substrates

We reported very intriguing results of directing self assembly of a series of ordered nanostructures based mostly on kMC simulations with single species of atoms associated with the kMC model. The simplicity of these results is surprising, so that we expect this simple direction of temperature-dependent ordered mound arrangements can be realized in the growth of patterned metal substrate, such as silver, with significant presence of Ehrlich-Schwoebel barrier on the surface, which there is

only one species associated with it. We propose to pattern a silver substrate with nanometer size pit arrays (preferred in-situ by focused ion beam (FIB)). We expect that the temperature dependence of ordered mound arrangements on a silver substrate might find wide applications in fast fabrication of plasmonic arrays.

Appendix A

Evidence for a Large, Thermal-Activated Characteristic Length Scale in Homoepitaxial Growth on GaAs(001)

In this appendix, we report on observations of growth on GaAs(001) surfaces nanopatterned with grooves of varying length/width aspect ratios. For homoepitaxial growth at temperatures near 500 ℃ , we find that ridges build up at the upper long edges of grooves oriented along [110]. No ridges form at the long edges of grooves oriented [$\underline{1}$10]; instead cusps form at the bottoms of such grooves. Most interestingly, we find that the evolution of ridge heights during growth breaks into two distinct branches, with the separation occurring at a groove length of 7.5 $\pm$ 2.5 um for growth at 525 ℃, and at a length which is an order of magnitude smaller than this for growth at 460 ℃. These observations indicate the presence of very large, thermally-activated characteristic lengths which governs the evolution of the topography during growth.

A.1 Motivation

In recent work [A.1- A.4], we have reported the observation of transient instabilities during MBE growth on topographically-patterned GaAs(001), whose characteristics change qualitatively across the temperature range of 500 ºC-600 ºC. We proposed that a small Ehrlich-Schwoebel barrier[A.5, A.6] at steps which descend along [110], along with a reduced nucleation barrier[A.7, A.8] at the edges of lithographically defined pits on the surface play significant roles in the observed transient instability and its temperature dependence. In previous chapters, we reported the results of square or round pits, however, it is important and interesting to know the effect of shape f patterns during growth. Therefore in this appendix, we probe the length scale dependence of growth instabilities in this system, using nanogrooved-patterned templates as a means of perturbing the growing surface, and find evidence for a very large, thermal-activated characteristic length scale.

A.2 Experiment

We patterned singular GaAs(001) wafers using electron-beam lithography followed by inductively-coupling plasma etching to create arrays of nanogrooves in the substrates. We oriented the nanogrooves with long axes along both [110] and [$\underline{1}$10], corresponding to the directions of the unit vectors for the the β_2(2x4) and c(4x4) reconstructions which occur during growth under As_2-rich conditions at common growth temperatures. We fabricated two sets of groove arrays on each substrate. In the first set, individual grooves are initially 200 nm wide, with a [110]/[$\underline{1}$10] aspect ratio which we vary systematically over the range from 0.005:1 to 200:1. The

second set consists of 100 nm initial-width grooves whose [110]/[$\bar{1}$10] aspect ratios range from 0.001:1 to 1000:1. For both sets patterned the initial groove depths at approximately 50 nm. We measured the topography of our samples using atomic force microscopy (AFM) in tapping mode, using carbon nanotube terminated probes. Each patterned sample was cycled between the molecular beam epitaxy (MBE) growth chamber (base pressure 2 x 10^{-11} mbar) for homoepitaxial growth and the AFM for characterization in atmosphere. At the beginning of each growth experiment the surface oxide was desorbed by heating the samples to 400 ℃ during exposure to atomic hydrogen within the MBE chamber, minimizing desorption induced roughness. The measured growth rate was 0.28 nm/sec, with the As_2 and Ga fluxes set for a beam equivalent pressure ratio of 10:1. We carried out growth at two temperatures, 460 ℃ and 525 ℃ to investigate the influence of kinetic parameters for epitaxial growth on these surfaces. Reflection high energy electron diffraction (RHEED) measurements showed that the surface reconstruction was c(4x4) beneath approximately 550 ºC in our growth experiments.

A.3 Results

A.3.1 Formation of Ridges at [110]-oriented Edges

In Fig. A.1, we show example of AFM images for samples initially patterned with arrays of 200 nm wide grooves, before and after various amounts of growth. The upper row of images, i.e. Figs. A.1(a)-(d) show [110]-oriented nanogrooves for the starting surface, and after growth of thicknesses of 60 nm, 100 nm, and 150 nm, respectively, for growth at a temperature of 460 ℃.

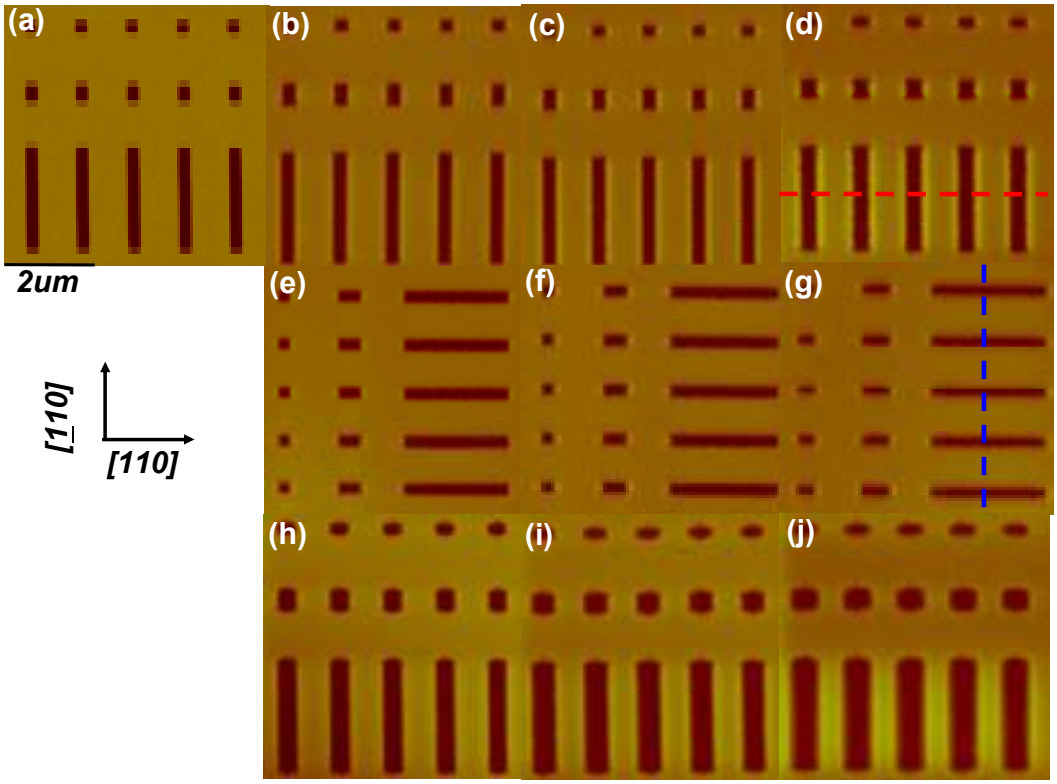

Fig. A.1 *(a)-(d) AFM images of 200 nm wide nanogrooves (long edges along [110] direction) with different growth thickness (a) 0nm; (b) 60nm; (c) 100nm; (d) 150nm at growth temperature of 460 ℃, [110]/[1̄10] aspect ratio is 1:1, 2:1 and 10:1; fig.A1(e)-(g) are AFM images of nanogrooves (long edges along [1̄10] direction) with different growth thickness at growth temperature of 460 ℃, (e) 60nm; (f) 100nm; (g) 150nm; with [110]/[1̄10] aspect ratio 1:1, 1:2 and 1:10; fig.1(h)-(j) AFM images of 200 nm wide nanogrooves (long edges along [110] direction) with same sequence of growth (h) 60nm; (i) 100nm; (j) 150nm at higher growth temperature of 525 ℃.*

The growing ridges at the long upper edges are visible as bright fringes to either side of the grooves. These ridges are even more easily seen in Fig. A.2(a), which consists of height profiles, measured from the images shown in Fig. A.1(a)-(d) along [110], as indicated by the red dashed line in Fig. A.1(d). In Figs. A.1(e)-(g), we show AFM images of orthogonal, [1̲10]-oriented grooves, for the same growth sequence. In this case no ridges are apparent at the upper sides of the long edges of the grooves; instead such features appear along the short directions.

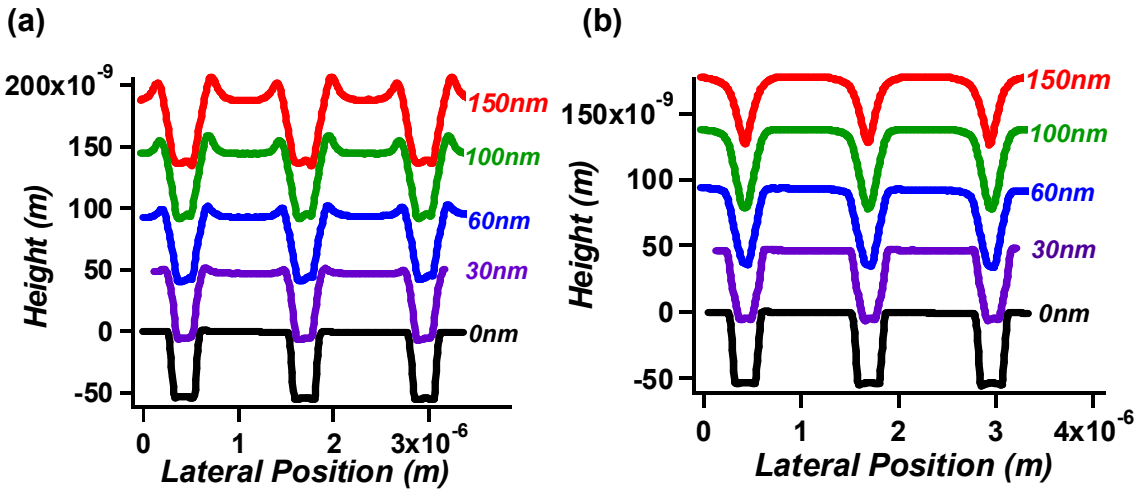

Fig. A.2 *(a) stacked line profiles cross perpendicular to the grooves along red dotted line of fig. A.1 (a)-(d); (b) stacked line profiles cross perpendicular to the grooves along blue dotted line of fig. A.1(e)-(g).*

This result is consistent with the earlier observations of Tadayyon et al.[A.1], of anisotropic ridge formation around circular pits during growth at 500 ºC. The absence of ridge formation at the long edges of [$\underline{1}$10]-oriented grooves is confirmed in Fig. A.2(b), which shows height profiles measured from Fig.1(e)-(g) along [$\underline{1}$10], as indicated by the blue dashed line in Fig. A.1(g). We have previously proposed that the anisotropic ridge formation might be understood based the effect of forming multi-step reconstruction along [110] orientation that reduces the nucleation barrier at the corresponding pit edges [A.7, A.8].

A.3.2 Anisotropy of Surface Evolution

Comparison of the two sets of height profiles in Fig. A.2 shows another striking difference between the modes of surface evolution during MBE growth for patterns made up of nanogrooves oriented along these two perpendicular orientations. Those oriented with their long edges parallel to [$\underline{1}$10] show a discernable narrowing along their short axis, with cusps first forming, and then persisting at the bottom of the grooves. For nanogroove patterns with long edges along [110], growth produces nearly the opposite behavior, i.e. a pronounced broadening along the orthogonal, [110] direction. The rate of broadening is temperature dependent, as can be seen in the bottom row of images, Figs. A.1(h)-(j), which show the results of a similar growth sequence, but at a somewhat temperature of 525 ℃. At this higher temperature, the rate of broadening of nanogrooves along [110] is approximately three times faster, than at 460 ℃, consistent with a smaller adatom sticking probability to the steps which bound these grooves.

A.3.3 Analysis of Ridge Heights

A.3.3.1 Length Scale Dependence of Ridge Heights-High T

We now show that analysis of the height of ridges vs. nanogroove length reveals a characteristic lateral length scale. In Fig. A.3(a) the heights of the ridges which form during growth at 525 ℃ along 200 nm wide [110]-oriented grooves are plotted as a function of growth thickness, for a range of [110]/[$\underline{1}$10] length aspect ratios. As the growth proceeds, the evolution of the ridge heights separates into two branches. For larger aspect ratios, i.e. 200:1, 100:1 and 50:1, the ridge heights evolve to a maximum of approximately 15 nm at a grown thickness of approximately 120 nm. In contrast, for the smaller groove aspect ratios, i.e. 20:1, 10:1 and 2:1, the ridge heights evolve to a maximum value of approximately 8 nm for grown thickness of approximately 100 nm. The pronounced break between the two branches indicated by the arrow in Fig. A.3(a) occurs at an initial aspect ratio of between 20:1 and 50:1, which corresponds to a groove length of between 4 um and 10 um. It is suggestive of an exceedingly long characteristic lateral length scale beyond which the growth kinetics changes abruptly. As a check of this interpretation, we examine the behavior of ridge heights for another set of arrays of nanogrooves, whose initial widths were 100 nm. As seen in Fig. A.3(b). the evolution of ridge heights for these narrower grooves also shows a break into two branches, at an aspect ratio between 50:1 and 100:1, corresponding to a groove length of between 5 um and 10 um. This is in agreement with that for the wider grooves.

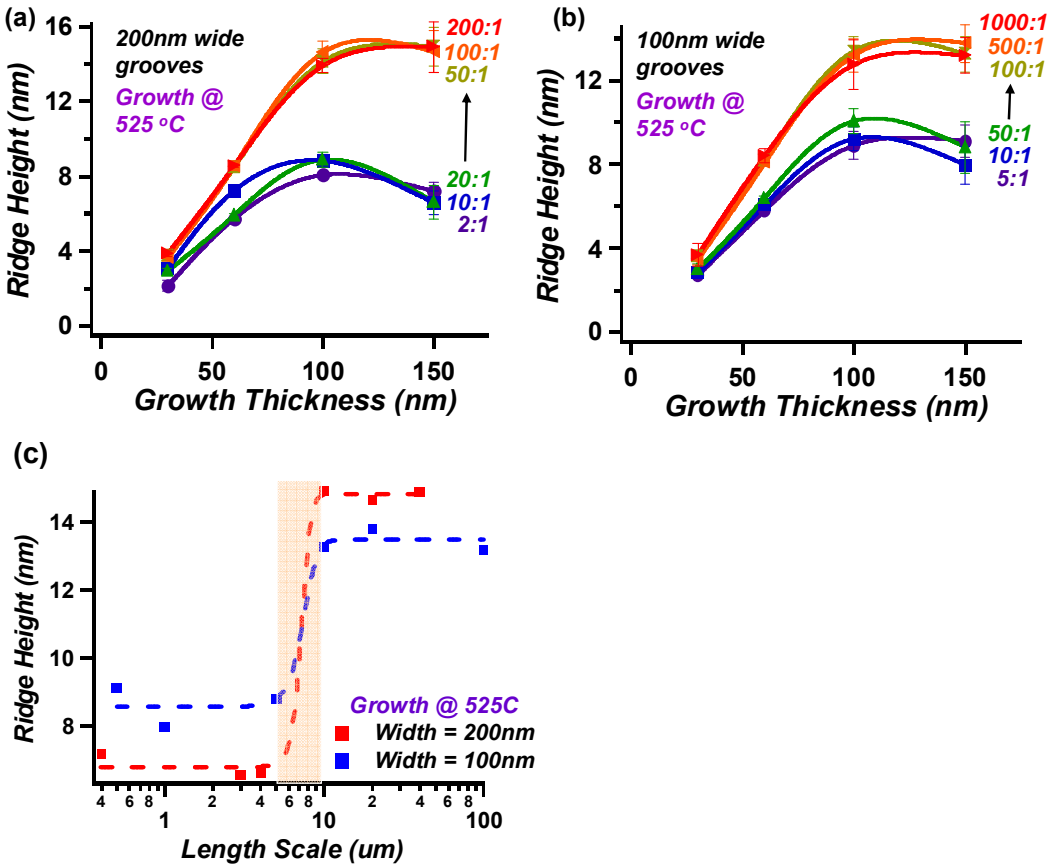

Fig. A.3 *Ridge heights vs. growth thickness at growth temperature of 525 ℃, showing aspect ratios (length scales) dependence of ridge heights for both sets of nanogrooves, (a) 200 nm wide nanogrooves; (b) 100 nm wide nanogrooves. Fig. A.3(c) consistence of characteristic lengths of 7.5 ± 2.5 um for both sets of nanogroove-patterned surface.*

We summarize this intriguing behavior Fig. A.3(c) where we plot the ridge height vs. groove length for both sets of nanogrooves for growth at 525 ℃. Both curves, display an inflection point at a characteristic length of 7.5 ± 2.5 um.

A.3.3.2 Length Scale Dependence of Ridge Heights- Low T

To probe the temperature dependence of this length scale we lowered the growth temperature to 460 ℃. The ridge heights have not yet reached a maximum by a grown thickness of 150 nm, however we do see signs of a splitting of the evolution into two branches at this temperature as well. Figs. A.4(a) and A.4(b) show plots of the ridge heights as a function of growth thickness, for 200 nm and 100 nm wide nanogrooves respectively, again for a range of aspect ratios. As shown by arrow in Fig. A.4(a) for the 200 nm wide nanogrooves a break, in the ridge height distribution curves occurs at an aspect ratio of between 2:1 and 10:1, corresponding to a groove length along [110] of between 400 nm and 1000 nm. For the 100 nm wide nanogrooves, as shown in Fig. A.4(b), the break in evolution occurs between aspect ratios 5:1 and 10:1, corresponding to a groove length of between 500 nm to 1000 nm. This is again in agreement with that for the wider grooves to within the uncertainty set by the increments between successive patterned lengths. Fig. A.4(c) summarizes this behavior, and shows that this characteristic length decreases by an order of magnitude, from 7.5 $\pm$ 2.5 um to 750 $\pm$ 250 nm, on lowering the growth temperature from 525 ℃ to 460 ℃.

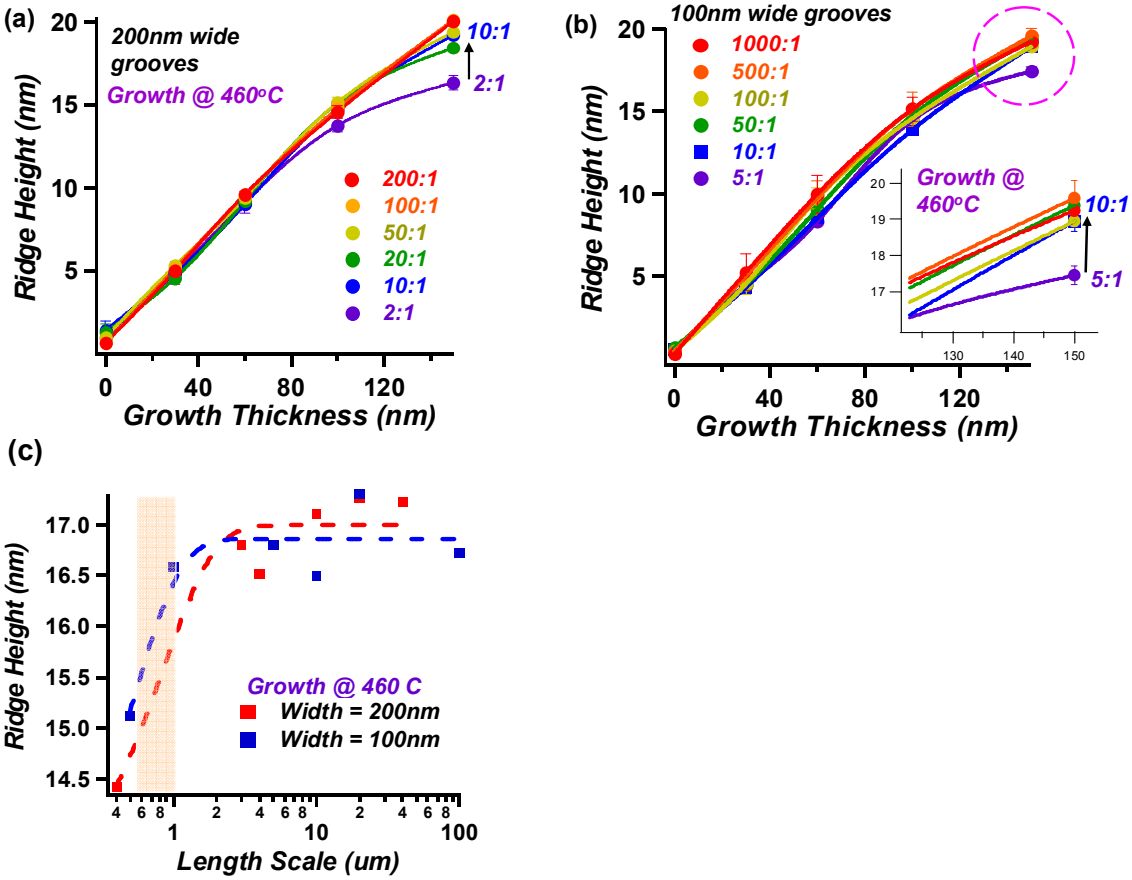

Fig. A.4 *Ridge heights vs. growth thickness at growth temperature of 460 ℃, showing aspect ratios (length scales) dependence of ridge heights for both sets of nanogrooves, (a) 200 nm wide nanogrooves; (b) 100 nm wide nanogrooves. Fig. A.4(c) Consistence of characteristic lengths of 750 ± 250 nm for both sets of nanogroove-patterned surface.*

A.4 Discussion

What is the physical origin of this behavior? We expect that the formation of the observed ridges, along upper edges of nanogrooves, initiates with island nucleation. In nucleation the kinetics of deposition, surface reconstruction and surface diffusion likely all play key roles. However as the individual fluxes and the surface reconstruction are the same for each of our growth experiments, the temperature dependence of large characteristic length scale we observe must derive from a thermally activated process. A logical candidate is surface diffusion. In fact it is widely assumed that during homoepitaxial growth on GaAs(001) under As-rich conditions, it is the diffusion of Ga adatoms on the growing surface is the rate limiting process [A.9]. Based upon this, a reasonable hypothesis is that the very long, thermal-activated characteristic lengths we observed might be a measure of the effective surface diffusion length of Ga adatoms before adding to a step[A.10], such as those which bound the grooves, or the sidewalls along [110]. If we assume that the presence of a small anisotropic Ehrlich-Schwoebel barrier tends to inhibit the attachment of Ga adatoms to steps at the edge of [110]-oriented grooves, then such adatoms on landing onto the surface regions between long nanogrooves should be "trapped", and more likely to nucleate islands. The maximum distance such an atom would need to diffuse to "escape" from between grooves, is. half of the length of grooves. The larger the ratio of this length to the adatom diffusion length, the more likely that an island will be nucleated between grooves. On the other hand, in the limit in which the half-length of the grooves is much shorter than the diffusion length of adatoms, they are likely to diffuse out of the region between nanogrooves, without

island nucleation. We thus associate a value of approximately one half of the groove length at which the break in the ridge height occurs with the Ga diffusion length. We thus estimate an effective diffusion length of 3.8 $\pm$ 1.3 um, at 525 ºC which is approximately a factor of three larger than the previously reported diffusion length for Ga adatoms on GaAs(001)- β_2(2x4) or at the transition from β_2(2x4) to c(4x4) under MBE growth conditions [A.10-15].

A.5 Conclusion

To summarize, our homoepitaxial growth experiments on nanogroove patterned GaAs(001) show evidence for a very large, thermal-activated characteristic length scale beyond which the kinetics change abruptly. The value of the observed characteristic length is 7.5 $\pm$ 2.5 um, at 525 ºC., and an order of magnitude less than this at 460 ºC. The logical interpretation is that we are probing the effective diffusion length of Ga adatoms, The nanogrooved patterned arrays on the surface might effectively reduce 2D Brownian motions of adatoms into a quasi-1D problem to enhance the diffusion length of diffusing Ga atoms. It is remarkable that even though the distance between grooves, and thus between available steps is many times smaller than this distance that a seemingly small Ehrlich-Schwoebel barrier [A.1, A.7] can result in adatoms diffusing such a long distance, and in the process encountering, but not adding to the edges of the lithographically defined grooves.

Appendix B

Another Mound Separation Analysis

– using the Generalized Wigner Surmise (GWS)

We use the approach proposed by Einstein et al. [B.1, B.2] which have been used to study terrace width distribution (TWD) on vincinal surfaces and also the capture zone (CZ) radii on surface where island growth occurs. This is the so called the General Wigner Surmise (GWS) with the equation shown below:

$$\boldsymbol{P_\rho(s) = A_\rho s^\rho \exp(-B_\rho s^2)}$$

where coefficients $A_\rho = 2\Gamma(\frac{\rho+2}{2})^{\rho+1} / \Gamma(\frac{\rho+1}{2})^{\rho+2}$, $B_\rho = \left[\Gamma(\frac{\rho+2}{2}) / \Gamma(\frac{\rho+1}{2})\right]^2$, s is the separation between two objects, ρ is the exponent parameter.

The exponent ρ in the generalized Wigner Surmise (GWS) provides valuable information of underlying physics of a few systems. In one example, i.e. the study of terrace width distributions, the exponent ρ takes on a value greater than 2 if there is a repulsion between steps [B.1]. It is not immediately clear if this aspect of the GWS carries over to the case of the mound separation distribution, as it is not clear what physics is behind the exponent ρ in this case. While it is interesting to speculate that

the exponent ρ might in some sense indicate the interaction between mounds, it will require further study to understand if this is so.

Nevertheless, for curiosity, we examined the distributions of mound separations in our simulations to see if they are "Wigner-like". The way we define the spacing is to take the edge to edge spacing as shown in Fig. B.1. Since mound size nearly reaches steady state after 1000ML of growth, we analyze the mound-mound separations at that stage of growth thickness. Again, we adopt image segmentation method to allow us to obtain the information of mound separations.

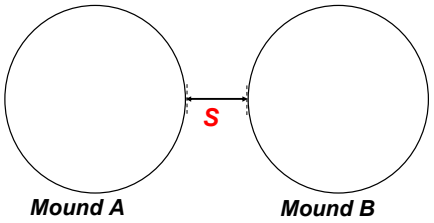

Fig. B.1 Defining separation s between two neighboring mounds after 1000ML of growth.

In Fig. B.2, we show plots of the mound separation distributions of our kMC simulations for both unpatterned and patterned surfaces. Figs. B.2 (a) and (b) are examples of mound separation distributions for the growth on unpatterned surfaces at two different growth temperatures, which the data are shown as open circles in plots ; Figs. B.2 (c) and (d) show examples of those for patterned surfaces, and the data are shown as open squares in plots. We fit our data by the expression of generalized Wigner Surmise (GWS), and the fits are reasonably well for both cases with and without patterns on the surfaces. Hence, the mound separation distributions display "Wigner-like" distributions.

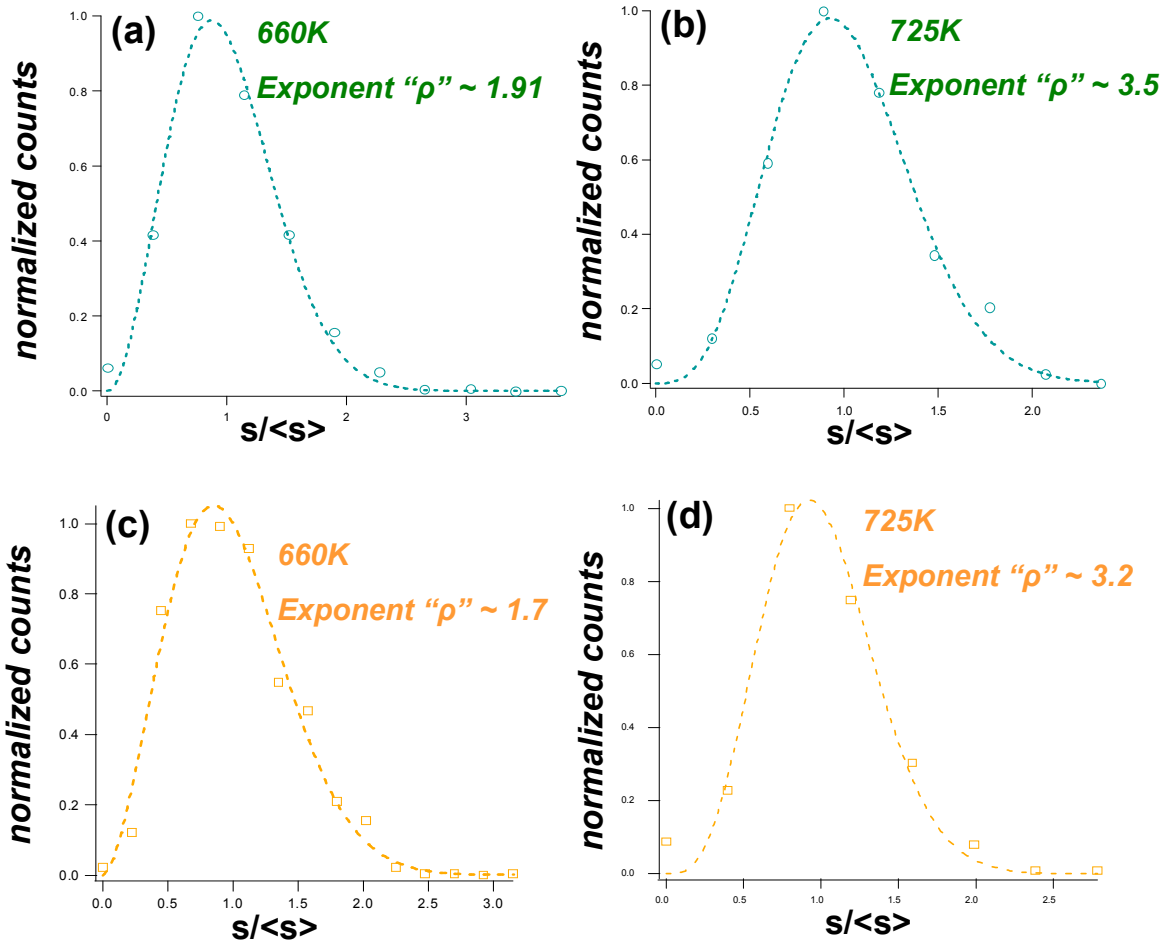

Fig. B.2 Mound separation distributions(open circles or squares) fitted by expression of Generalized Wigner Surmise (GWS (dashed curves). *(a) and (b) are the cases for growth on unpatterned surfaces, with the growth temperature of (a) 660K and (b) 725K; (c) and (d) are the cases for growth on patterned surfaces, with the growth temperature of (c) 660K and (d) 725K.*

Now based on many simulations, we systematically plot the exponents as a function of growth temperatures for both unpatterned and patterned cases, which is shown in Fig. B.3.

For the simulated growth on unpatterned surfaces, corresponding to the green curve in Fig. B.3, the exponent starts with a value close to 2 at low growth temperature. As we raise the growth temperature, the exponent slowly increases to a value of 4.

For comparison, results for simulated growth on the patterned surfaces are illustrated by the orange curve in Fig. B.3; the insets are the corresponding topological structures and correlation maps at the growth temperature pointed by arrows. At a relatively low temperature of 660K, where we start seeing (A/3 x A/3) periodicity of mound structure, the natural size of the mounds is smaller than 1/3 of the spacing between patterns. The best fit to a GWS dependence leads to an exponent close to 2. As we raise the temperature to 700K, the natural separation of mounds increases continuously, passing through a value of 1/3 of the pattern spacing at 680 K, but still the simulated mound spacing remains locked in the same fixed amount as lower temperature. The simulated images indicate that increasing the temperature beyond 680K gives arise to disorder arrangement of growth mounds: the mound shapes distort and the lattice of mound seems to start rotating in order to accommodate mounds with larger size. The value of the GWS exponent, increases though a value of 4 at 680K, reaching a maximum close to 6 by 700K. Based upon the analogy with the terrace width case this increase in exponent might be interpreted

as signifying a mound-mound interaction which becomes more repulsive due to accommodating mounds with increasing size in the (A/3 x A/3) phase

Raising growth temperature further to 710K in the simulations results in an abrupt change of the mound arrangement, to a lower density $A/\sqrt{2}$ x $A/\sqrt{2}$ phase. Coincident with this, the GWS exponent drops abruptly. The natural mound separation size is 0.62 A, i.e. smaller than the $1/\sqrt{2}$ of the pattern spacing at the growth temperature of 710K. Raising the growth temperature further results again in a monotonic increase in the GWS exponents, as the natural mound separation increases through and beyond a value of $A/\sqrt{2}$. The exponent again drops abruptly at a temperature of ~738K, coincident with an abrupt change in the mound arrangement to a third, even lower density, A x A phase.

Intriguingly, we thus observe that the GWS exponent displays abrupt changes coincident with the phase transitions between the ordered mound phases in our simulations. This seems to support a hypothesis in which the exponent ρ is related to the interaction between mounds and the generalized Wigner Surmise (GWS) could possibly be adopted in the system of mound formation, with the "neutral" value corresponding to $\rho=4$, rather than the $\rho=2$ value found in the case of step interactions [B.1]. Further analysis is warranted to test this hypothesis.

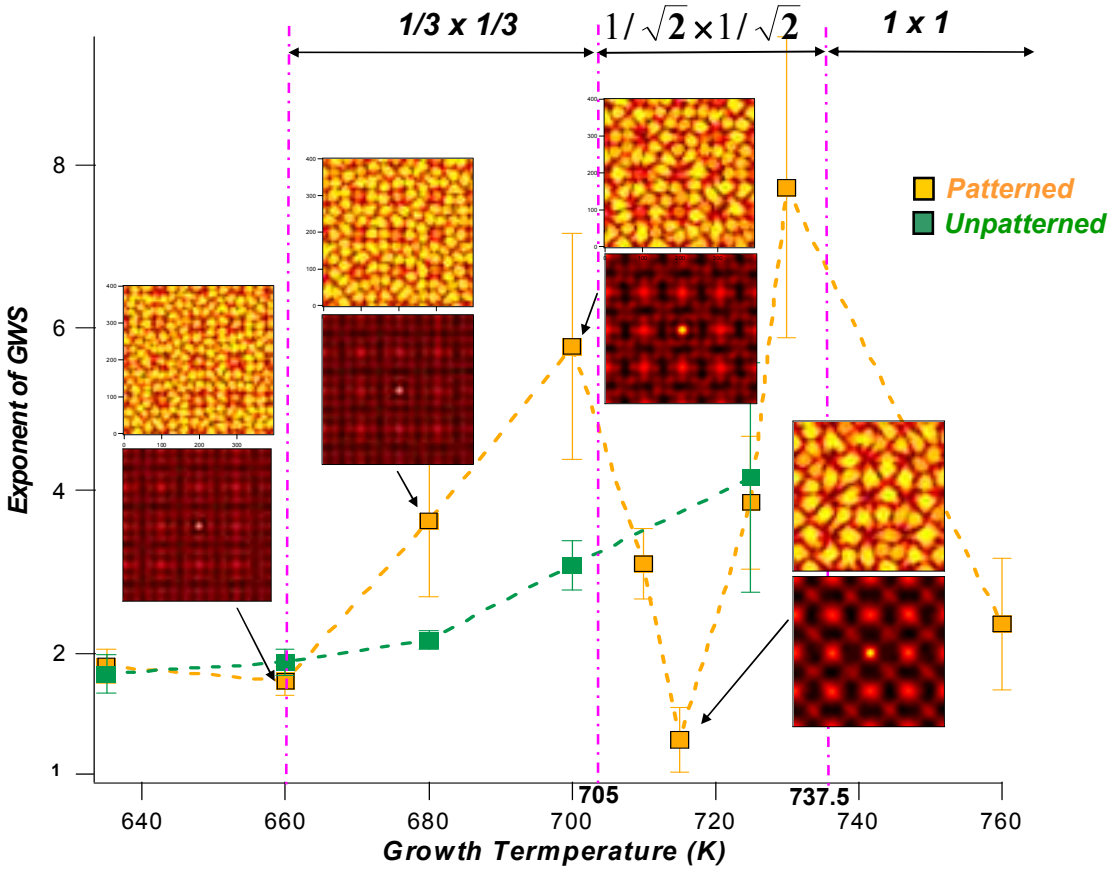

Fig. B.3 Exponent of GWS vs. growth temperature. *Orange curve is showing the case of patterned surface; green curve is for unpattered surface. Insets are the corresponding topological structures and correlation maps at the growth temperature pointed by arrows.*

Appendix C

Image Segmentation Method - Fortran 95 Code

Below is the Fortran code developed by Dr. Hung-Chih Kan that allow us to calculate mound size distributions, mound separation distributions and number of density of mounds.

```
!     Last change:  HCK   5 Feb 2010    10:36 am

program Img_Seg
CHARACTER*80 imagefile, segfile
CHARACTER*1200 txline
INTEGER Nx,Ny,Nt,Nk,Nx1,Ny1

! Variables for Sorting
INTEGER*8, ALLOCATABLE, DIMENSION(:,:) :: hR,hC,hT,hB,h
INTEGER*8, ALLOCATABLE :: indx(:), key(:),k_freq(:),k_start(:), k_indx(:)
DOUBLE PRECISION, ALLOCATABLE:: h0(:), BMask(:)
DOUBLE PRECISION hmin,hmax,lmin,lmax
INTEGER i,j,k
INTEGER tmpkey1,tmpkey2,tmpkey3

! Variables for  distance transformation
INTEGER, allocatable :: DT_h(:)
INTEGER :: island,c_dt=0,subis
INTEGER, ALLOCATABLE :: ispxl(:)
LOGICAL :: edge_detected, abnormal
CHARACTER*1 ans

! Variables for Segmentation
```

```
INTEGER:: MASK = -2, WSHED = 0, INIT=-1
INTEGER*8,ALLOCATABLE :: h_out(:), h_dist(:)
INTEGER*8, ALLOCATABLE :: que(:)
INTEGER:: c_label=0,c_dist, p_false=-1
INTEGER p,q1st,qend,qsize,p1,p2,round_1st,round_end
INTEGER, DIMENSION(8) :: pn,pn1
LOGICAL :: Que_empty, q1st_rst = .FALSE., qend_rst=.false.

! Variable for post processing

DOUBLE PRECISION, ALLOCATABLE :: p_tbl(:),
p_pxl(:),p_1st(:),Partial_key(:),NewMask(:)
DOUBLE PRECISION, ALLOCATABLE :: Iimg(:),Timg(:),Vstp(:),Vtrs(:)
INTEGER, allocatable :: Itrs(:),Istp(:)
INTEGER, DIMENSION(8) :: E_pxl=(/2,1,4,3,8,7,6,5/)
INTEGER :: A_partial_island
LOGICAL :: partial_island, edge_pixel, repeated_pixel
INTEGER :: edg1,edgx,past_edg,edgpxl,ipartial,cpartial
INTEGER :: Ntrs,Nstp
DOUBLE PRECISION :: htmp
LOGICAL :: same_terrace


! Mound statistics

DOUBLE PRECISION :: M_size_avg, M_size_std, M_num_density
INTEGER, ALLOCATABLE :: M_num(:), M_c(:), M_x(:),M_y(:)
INTEGER :: M_size,dmx,dmy,MdV

DOUBLE PRECISION, ALLOCATABLE,DIMENSION(:) :: M_d
INTEGER, ALLOCATABLE, DIMENSION(:) :: M_d_hist
DOUBLE PRECISION :: M_d_min, M_d_max, M_dd

!**********************!
!                      !
!  Input Graphic File  !
!                      !
!**********************!


PRINT *,'Enter image filename: '
read *,imagefile
Nx=400;Ny=400
Nx1=Nx-1;Ny1=Ny-1
Nt=Nx*Ny
Nk=SQRT(REAL(Nt))
```

```
ALLOCATE (h0(Nt),indx(Nt),key(Nt),k_freq(Nk),k_start(Nk),k_indx(Nk))
ALLOCATE (BMask(NT),DT_h(Nt))
ALLOCATE (h(Nx,Ny))

OPEN(101,FILE=imagefile)

do i=1,Ny
  read (101,*) (h0(j),j=1+(i-1)*Nx,i*Nx)
  h(:,i)=h0(1+(i-1)*Nx:i*Nx)
end do
CLOSE(101)


do i=2,Nx-1
  do j=2,Ny-1

    abnormal = (abs(h(i,j) - h(i+1,j)) > 100 ) .and.  (abs(h(i,j) - h(i-1,j)) > 100 )  .and.
&
            (abs(h(i,j) - h(i,j+1)) > 100 ) .and.  (abs(h(i,j) - h(i,j-1)) > 100 )
    if (abnormal) then
      PRINT *,'abnormal pixel at (',i,',',j,') h = ',h(i,j)
      h(i,j)=(h(i+1,j)+ h(i-1,j)+ h(i,j+1) + h(i,j-1))/4
      PRINT *,'Modified h = ', h(i,j)
    end if
  end do
end do

!do i=1, 20
!  h( 1,2:Ny1)  =  h(  2,2:Ny1)
!  h(Nx,2:Ny1)  =  h(Nx1,2:Ny1)
!  h(2:Nx1, 1)  =  h(2:Nx1,  2)
!  h(2:Nx1,Ny)  =  h(2:Nx1,Ny1)
!  h(1,1)=h(2,2)
!  h(Nx,1)=h(Nx1,2)
!  h(1,Ny1)=h(2,Ny1)
!  h(Nx,Ny)=h(Nx1,Ny1)
!  h(2:Nx1,2:Ny1) = (REAL(h(1:Nx1-
1,2:Ny1))+REAL(h(3:Nx,2:Ny1))+REAL(h(2:Nx1,1:Ny1-
1))+REAL(h(2:Nx1,3:Ny)))/4
!end do
OPEN(102,FILE='Transmap.dat')
do i=1,Ny
  WRITE(102,'(600(I8,2x))') (h(j,i), J=1,Nx)
end do
CLOSE(102)
```

```
do i=1,Ny
   Dt_h(1+(i-1)*Nx:i*Nx)=h(:,i)
end do

OPEN(102,FILE='Transmap2.dat')
do i=1,Ny
  WRITE(102,'(600(I8,2x))') (Dt_h(j), J=1+(i-1)*Nx,i*Nx)
end do
CLOSE(102)

!hmin=MINVAL(Dt_h)
!hmax=MAXVAL(Dt_h)
!do
!  PRINT *,'The maxium in the image is ',hmax
!  PRINT *,'The minimum in the image is ',hmin
!  PRINT *,'Do you want to set the saturate the image with a lower maximum? [y/n]
'
!  read *, ans
!  if (ans .eq. 'n') exit
!  if (ans .eq. 'y') then
!    do
!      PRINT *,'Enter a new maximum D, ',hMIN,'=< D <=',hmax,' '
!      read *,tempkey2
!      if ((tempkey2>=hmin).AND.(tempkey2<=hmax)) exit
!    end do
!    DT_h=MIN(DT_h,tempkey2)
!    do
!      PRINT *,'Enter a new minimum D, ',hMIN,'<= D <=',hmax,' '
!      read *,tempkey2
!      if ((tempkey2>=hmin).AND.(tempkey2<=hmax)) exit
!    end do
!    DT_h=MIN(DT_h,tempkey2)
!
!    OPEN(103,'modified_map.dat')
!    do i=1,Ny
!      write (103,'(600(I6,1x))') (DT_h(j), j=(i-1)*Nx+1,i*Nx)
!    end do
!    CLOSE(103)
!    PRINT *,'map updated'
!  end if
!end do
!DT_h=DT_h-tempkey2
!DT_h=h0-MINVAL(h0)
DT_h=DT_h -MINVAL(DT_h)
```

```
!*********************************!
!                                 !
!  Sorting Image Pixels with Key  !
!                                 !
!*********************************!
key=DT_h+1
indx=-1

k_freq=0
do i=1,Nt  !Scan key for the occuring frequency for each  value
  k_freq(key(i)) = k_freq(key(i)) + 1
end do

k_start(1)=1
do i=1,Nk-1
   k_start(i+1)=k_start(i) +k_freq(i)
   !PRINT *,i,k_start(i),k_freq(i)
end do
 !PRINT *,Nk,k_start(Nk),k_freq(Nk)

k_indx=0
do i=1,Nt
  tmpkey1=key(i)
  tmpkey2=k_start(tmpkey1)+k_indx(tmpkey1)
  indx(tmpkey2)=i
  k_indx(tmpkey1)=k_indx(tmpkey1)+1
end do


!******************!
!                  !
! Imspection codes !
!                  !
!******************!

!open (102,FILE='sort.dat')
!do i=Nk,1,-1
!  WRITE(102,'(100(I12,1x))') ( key(indx(j)),j=k_start(i),k_start(i)+k_freq(i)-1)
!  WRITE(102,'(100(I12,1x))') (indx(j),j=k_start(i),k_start(i)+k_freq(i)-1)
!  WRITE(102,'(100(E12.6,1x))') (h0(indx(j)),j=k_start(i),k_start(i)+k_freq(i)-1)
!end do
!close (102)


!********************!
```

```
!                          !
! Image Segmentation       !
!                          !
!**************************!

qsize= 10*MAXVAL(k_freq)+1
ALLOCATE (que(qsize),h_out(Nt),h_dist(Nt))
h_out = INIT
h_dist = 0
qend=0 ; round_end=0
q1st=1 ; round_1st=1

do i=Nk,0.05*Nk,-1
  tmpkey1=k_freq(i)
  if (tmpkey1 > 0 ) then
    !PRINT *,'Level',i
    do j=k_start(i),k_start(i)+tmpkey1-1
      p=indx(j)
      !PRINT *,'Level:',i,j,p
      h_out(p)=MASK
      call neighbor8(p,pn)
      !if ((MOD(p,Nx)==0).OR.(MOD(p,Nx)==1)) PRINT *,p,pn
      !if ((p<Nx).OR.(p>Nt-Nx)) PRINT *,p,pn
      do k=1,8
        if ((h_out(pn(k))>0).OR.(h_out(pn(k))==WSHED)) then
          h_dist(p)=1
          call fifo_add(p)
        end if
      end do
    end do

    c_dist=1; call fifo_add(p_false)

    do
      call fifo_first(p)
      if (p == p_false) then
        call fifo_empty(que_empty)
        if (que_empty) then
          exit
        else
          call fifo_add(p_false)
          c_dist=c_dist + 1
          call fifo_first(p)
        end if
      end if
    ! PRINT *,'Flooding; Level: ',i
```

```
      call neighbor8(p,pn)
     ! PRINT *,p,pn
      do k=1,8
        if
((h_dist(pn(k))<c_dist).AND.((h_out(pn(k))>0).OR.(h_out(pn(k))==WSHED)))
then
         if (h_out(pn(k)) > 0) then
          if ((h_out(p)==MASK).OR.(h_out(p)==WSHED)) then
            h_out(p)=h_out(pn(k))
          else if (h_out(p) /= h_out(pn(k))) then
            h_out(p)=WSHED
          else
          end if
         else if (h_out(p) == MASK) THEN
          h_out(p) = WSHED
         else
         end if
        else if ((h_out(pn(k))==MASK).AND.(h_dist(pn(k))==0)) then
         h_dist(pn(k))=c_dist+1
         call fifo_add(pn(k))
        else
        end if
       end do
     end do

    ! PRINT *,'new minimun; Level: ',i

     do j=k_start(i),k_start(i)+tmpkey1-1
       p=indx(j)
       h_dist(p)=0
       if (h_out(p) == MASK) then
         c_label=c_label+1
         call fifo_add(p)
         h_out(p)=c_label
         do
           call fifo_empty(que_empty)
           if (que_empty) exit
           call fifo_first(p1)
           call neighbor8(p1,pn1)
           do k=1,8
             if (h_out(pn1(k))==MASK) then
               call fifo_add(pn1(k))
               h_out(pn1(k))=c_label
             end if
           end do
         end do
```

```
     end if
    end do
  end if
end do

OPEN(102,FILE='sort_img_'//imagefile)
do i=1,Ny
  write (102,'(600(I6,1x))') (h_out(j), j=(i-1)*Nx+1,i*Nx)
end do
CLOSE(102)

PRINT *,'There are ' ,c_label,'mounds.'

! h_out = -1 unprocessed pixel
!       =  0 boundary pixels (those can not be assigned between neighboring islands)
!       >= 1 mound pixels

!*******************************!
!                               !
!  Post Segmentation Processing !
!                               !
!*******************************!

! Nk-1 : total number of mounds
! k_freq(i) = pixel coverage of i-th mound (i>1)

Nparticle = c_label
Island = Nt
key=MAX(1,h_out+1)
Nk=MAXVAL(key); PRINT *,NK,MINVAL(key)
DEALLOCATE(k_freq,k_start,k_indx)
ALLOCATE(k_freq(Nk),k_start(Nk),k_indx(Nk))
ALLOCATE(P_tbl(Island), P_pxl(Nparticle), P_1st(Nparticle))
indx=-1
call Sort_key(key,indx,Nk)



!*****************************!
!                             !
!  Identify partial islands   !
!                             !
!*****************************!
A_partial_island = 0
ALLOCATE(Partial_key(Island))
ipartial = 0
```

```
do i=2,Nk
  do j=k_start(i),k_start(i)+k_freq(i)-1
    tmpkey1= indx(j)
    tmpkey2= MOD(tmpkey1,Nx); If (tmpkey2==0) tmpkey2=Nx
    tmpkey3= int((tmpkey1-1)/Nx)+1
    partial_island = (tmpkey2 == 1).OR.(tmpkey2 == Nx) .OR. &
                     (tmpkey3 == 1).OR.(tmpkey3 == Ny)
    if (partial_island) then
      !PRINT *,'Island # ',i, ' is partially scanned in the image.'
      !PRINT *,i,tmpkey1, tmpkey2,tmpkey3
      A_partial_island = A_partial_island + k_freq(i)
      k_freq(i) = 0
      ipartial = ipartial +1
      Partial_key(ipartial)=i
      exit
    end if
  end do
end do
PRINT *,'There are ',ipartial,' partial islands found:'
PRINT *,INT(Partial_key(1:ipartial))


!*********************!
!                     !
!  Monund statistics  !
!                     !
!*********************!

! 1. Average mound size and standard deviation

M_size_avg = REAL(SUM(k_freq(2:Nk)))/REAL(Nk-iPartial-1)

tmpkey1 = 0

do i=2,NK
  tmpkey1 = tmpkey1 + k_freq(i)**2
end do
PRINT *, tmpkey1/REAL(Nk-iPartial-1), M_size_avg**2

M_size_std = SQRT(tmpkey1/REAL(Nk-iPartial-1)-M_size_avg**2)

M_num_density = REAL(Nk-1-ipartial) / REAL(Nt - A_partial_island)



! 2. Histogram of Mound size
```

```
do i= 1,ipartial
  k_freq(Partial_key(i))=M_size_avg
 ! PRINT *, Partial_key(i)
end do

tmpkey1 = MAXVAL(k_freq(2:Nk))
tmpkey2 = MINVAL(k_freq(2:Nk))

PRINT *,' '
PRINT *,'The program is going to generate the histogram of the island island size
distribution.'
PRINT *,'That is the number of islands between size V and V+dV.'
PRINT *,'So far we have the following.'
PRINT *,' '
PRINT *,'Total number of isalnds = ', Nk
PRINT *,'Max, Min island size = ', tmpkey1,tmpkey2
PRINT *,'Average mound size = ', M_size_avg
PRINT *,'Standard deviation = ', M_size_std
PRINT *,' '
PRINT *,'Do you want to choose the size of dV ?'
PRINT *,'or let the program to use dV=(Vmax-Vmin)/20 ?'
do
  PRINT *,'Enter [y/n] '
  read *,ans
    if ((ans == 'y').OR.(ans == 'n')) exit
end do
if (ans=='y') then
   PRINT*,'Enter the size of dV. '
   read *,tmpkey3
   MdV=INT((tmpkey1-tmpkey2)/tmpkey3+1)
else
   MdV=21
   tmpkey3= (tmpkey1-tmpkey2)/20
end if


ALLOCATE(M_num(MdV))
j=1
M_num=0
do i=2,Nk
  IF (i /= Partial_key(j)) then
    tmpkey1 =k_freq(i)/tmpkey3-tmpkey2/tmpkey3+1
    if (tmpkey1 == MdV+1)tmpkey1 = Mdv
    M_num(tmpkey1) = M_num(tmpkey1) + 1
  else
```

```
   j=Min(j+1,ipartial)
  end if

end do

! Export results

OPEN(102,FILE='hist_'//imagefile)

WRITE(102,'(E22.10,2x,A80)') M_size_avg, 'Average mound size (number of
pixels)'
WRITE(102,'(E22.10,2x,A80)') M_size_std, 'standard diviation of mound size
(number of pixels)'
WRITE(102,'(E22.10,2x,A80)') M_num_density*1e4, 'Number density of Mounds
mound ( per (100 pixel)^2 ) '

do i=1,MdV

tmpkey1=MAX(tmpkey3*int(REAL(tmpkey2)/REAL(tmpkey3)+0.5),tmpkey3*(tm
pkey2/tmpkey3+i-1))
  WRITE(102,'(2(I10,2x))') tmpkey1 , M_num(i)
end do

CLOSE(102)

! 3. Height weighted mound center coordinate

hmin=MINVAL(h0)

ALLOCATE(M_c(Nk), M_x(Nk), M_y(Nk))
M_c=0; M_x=0; M_y=0
OPEN(103,FILE='MoundCoor_'//imagefile)

j=1
do i=2,Nk
  IF (i /= Partial_key(j)) then
    tmpkey1 = k_start(i)+k_freq(i)-1
    !tmpkey1 = MAXVAL(h0(indx(k_start(i):tmpkey1))) ;tmpkey2=0; tmpkey3=0
    !PRINT *, tmpkey1
    !tmpkey1=0
    !do k=k_start(i),k_start(i)+k_freq(i)-1
    !  tmpkey2=h0(indx(k))
    !  if (tmpkey2>= tmpkey1) tmpkey1=tmpkey2
    !end do
    !PRINT *, tmpkey1
```

```
    do k=k_start(i),tmpkey1
      tmpkey3=indx(k)
      tmpkey2=h0(tmpkey3)-hmin
      !if (tmpkey2 == tmpkey1) then
        dmx=MOD(tmpkey3,Nx); if (dmx==0) dmx=Nx
        dmy=INT((tmpkey3-1)/Nx)+1
        M_x(i)=M_x(i) + dmx*tmpkey2
        M_y(i)=M_y(i) + dmy*tmpkey2
        M_c(i)=M_c(i) + tmpkey2
        !PRINT *,tmpkey2,tmpkey1
        !PRINT *,M_c(i),dmx,dmy
        !WRITE(103,'(2(I10,2x))') dmx,dmy
      !end if
    end do
    M_x(i)=M_x(i)/M_c(i)
    M_y(i)=M_y(i)/M_c(i)

   ! PRINT *,i,M_x(i),M_y(i)
    WRITE(103,'(2(I10,2x))') M_x(i),M_y(i)
  else
    j=Min(j+1,ipartial)
   ! PRINT *,'partial mound',Partial_key(j)
  end if
end do
CLOSE(103)

! 4. Island spacing statistics

ALLOCATE (M_d((Nk-2)*(Nk-1)/2),M_d_hist(50))
tmpkey1=0
do i=2,Nk
  if ((M_x(i)/=0).or.(M_y(i)/=0)) then
    do j=i+1,Nk
      if ((M_x(j)/=0).or.(M_y(j)/=0)) then
        tmpkey1=tmpkey1+1
        M_d(tmpkey1) = SQRT(REAL( (M_x(i)-M_x(j))**2 + (M_y(i)-M_y(j))**2) )
        !PRINT *,tmpkey1, M_d(tmpkey1)
      end if
    end do
  end if
end do

M_d_min = MINVAL(M_d(1:tmpkey1))
M_d_max = MAXVAL(M_d(1:tmpkey1))
M_dd = (M_d_max-M_d_min)/50
```

```
M_d_hist=0

PRINT *,'M_d_max, M_d_min = ',M_d_max, M_d_min
do i =1,tmpkey1
  tmpkey2=INT((M_d(i)-M_d_min)/M_dd)+1
  if (tmpkey2 == 51) tmpkey2=50
  M_d_hist(tmpkey2)=M_d_hist(tmpkey2)+1
end do

open (104,FILE='Islandspacing_'//imagefile)
do i=1, 50
  WRITE(104,*) (M_d_min+ (REAL(i)-0.5)*M_dd), M_d_hist(i)
end do
CLOSE(104)



! 3. Height weighted mound center coordinate


!ALLOCATE(M_c(Nk), M_x(Nk), M_y(Nk))
!M_c=0; M_x=0; M_y=0
!OPEN(103,FILE='MoundCoor_'//imagefile)

!j=1
!do i=2,Nk
!  IF (i /= Partial_key(j)) then
!    tmpkey1=0    ;tmpkey2=0; tmpkey3=0
!    do k=k_start(i),k_start(i)+k_freq(i)-1
!      tmpkey1=indx(k)
!      tmpkey2=h0(tmpkey1)
!      dmx=MOD(tmpkey1,Nx); if (dmx==0) dmx=Nx
!      dmy=INT((tmpkey1-1)/Nx)+1
!      M_x(i)=M_x(i)+dmx*tmpkey2
!      M_y(i)=M_y(i)+dmy*tmpkey2
!      tmpkey3=tmpkey3+tmpkey2
!    end do
!    M_x(i)=M_x(i)/tmpkey3
!    M_y(i)=M_y(i)/tmpkey3
!
!    PRINT *,i,M_x(i),M_y(i)
!    WRITE(103,'(2(I10,2x))') M_x(i),M_y(i)
!  else
!    j=Min(j+1,ipartial)
!    PRINT *,'partial mound',Partial_key(j)
!  end if
```

```
!end do
!CLOSE(103)

CONTAINS


subroutine neighbor8(p,pn)
INTEGER p                                  !p(5)  p(3) p(6)
INTEGER, DIMENSION(8) :: pn                        !p(1)  p    p(2)
INTEGER px,py                               !p(7)  p(4) p(8)
py=INT((p-1)/Nx)+1
px=mod(p,Nx); if (px == 0) px = Nx
if (px == 1)  then
  pn(1)=p; pn(5)=p; pn(7)=p
  pn(2)=p+1
  if (py == 1) then
    pn(3)=p; pn(6)=p
    pn(4)=p+Nx ; pn(8)=Pn(4)+1
  else if (py == Ny) then
    pn(4)=p; pn(8)=p
    pn(3)=p-Nx; pn(6)=pn(3)+1
  else
    pn(3)=p-Nx; pn(6)=pn(3)+1
    pn(4)=p+Nx ; pn(8)=Pn(4)+1
  end if
else if(px == Nx) then
    pn(6)=p;pn(2)=p; pn(8)=p
    pn(1)=p-1
  if (py == 1) then
    pn(5)=p; pn(3)=p
    pn(4)=p+Nx;pn(7)=pn(4)-1
  else  if (py == Ny) then
    pn(4)=p; pn(7)=p
    pn(3)=p-Nx; pn(5)=pn(3)-1
  else
    pn(3)=p-Nx; pn(5)=pn(3)-1
    pn(4)=p+Nx; pn(7)=pn(4)-1
  end if
else if ((py == 1).AND.(px>1).AND.(px<Nx)) then
   pn(5)=p; pn(3)=p; pn(6)=p
   pn(1)=p-1; pn(2)=p+1
   pn(4)=p+Ny;pn(7)=pn(4)-1;pn(8)=pn(4)+1
else if ((py == Ny).AND.(px>1).AND.(px<Nx)) then
   pn(7)=p; pn(4)=p; pn(8)=p
   pn(1)=p-1; pn(2)=p+1
   pn(3)=p-Ny;pn(5)=pn(3)-1;pn(6)=pn(3)+1
```

```
else
   pn(3)=p-Ny;pn(5)=pn(3)-1;pn(6)=pn(3)+1
   pn(1)=p-1; pn(2)=p+1
   pn(4)=p+Ny;pn(7)=pn(4)-1;pn(8)=pn(4)+1
end if
!PRINT *,p,pn
end subroutine

!*******************************!
!                               !
!  Sorting Image Pixels with Key !
!                               !
!*******************************!
subroutine Sort_Key(key,indx,Nk)
INTEGER*8 :: key(:), indx(:)
INTEGER :: NK
k_freq=0
do i=1,Nt  !Scan key for the occuring frequency for each  value
  k_freq(key(i)) = k_freq(key(i)) + 1
end do
!PRINT *,'Nk =',Nk
k_start=0
k_start(1)=1
do i=1,Nk-1
   k_start(i+1)=k_start(i) +k_freq(i)
   !PRINT *,i,k_start(i),k_freq(i)
end do

!PRINT *,Nk,k_start(Nk),k_freq(Nk)

k_indx=0
do i=1,Nt
  tmpkey1=key(i)
  tmpkey2=k_start(tmpkey1)+k_indx(tmpkey1)
  indx(tmpkey2)=i
  k_indx(tmpkey1)=k_indx(tmpkey1)+1
end do
end subroutine




subroutine fifo_add(p)
INTEGER p
qend=qend+1;
```

```
if (qend>qsize) then
qend_rst=.true.
qend=1
END if
que(qend)=p

if (qend_rst.and.q1st_rst) then
 !PRINT *,'add',q1st,q1st_rst,qend,qend_rst ,qsize
 qend_rst=.false.
 q1st_rst=.false.
end if
!PRINT *,'add',q1st,q1st_rst,qend,qend_rst ,qsize
end subroutine

subroutine fifo_first(p)
INTEGER p
p=que(q1st);
q1st=q1st+1;
if (q1st>qsize) then
  q1st_rst=.true.
  q1st=1
END if

if (qend_rst.and.q1st_rst) then
 !PRINT *,'first',q1st,q1st_rst,qend,qend_rst ,qsize
 qend_rst=.false.
 q1st_rst=.false.
end if
!PRINT *,'first',q1st,q1st_rst,qend,qend_rst ,qsize
end subroutine

subroutine fifo_empty(q)
LOGICAL :: q
if (q1st_rst) then
  q=.true.
else if (qend_rst) then
  q=.false.
else
  q=q1st > qend
end if
!PRINT *,'empty',q1st,q1st_rst,qend,qend_rst ,qsize
!PRINT *,'empty',q
!PRINT *,'empty',round_1st,round_end,q
end subroutine
end program
```

Bibliography

Chapter One:

[1.1] G. E. Moore, Electronics 38, 114 (1965).

[1.2] H. S. Bennett, J. Res. National Institutes of Standards and Technology 112, 25 (2007).

[1.3] S. Mann, Nat. Mater. 8, 781 (2009).

[1.4] J. L. Gray, S. Atha, R. Hull, and J. A. Floro, Nano Lett. 4, 2447 (2004)

[1.5] B. Yang, F. Liu, and M. G. Lagally, Phys. Rev. Lett. 92, 025502 (2004)

[1.6] J. L. Gray, R. Hull, and J. A. Floro, J. Appl. Phys. 100, 084312 (2006)

[1.7] H. C. Kan, S. Shah, T. T. Tadyyon-Eslami, and R. J. Phaneuf, Phys.Rev. Lett. 92, 146101 (2004)

[1.8] Tadayyon-Eslami et al., Phys. Rev. Lett 97, 126101 (2006)

[1.9] M.D. Johnson et al., Phys. Rev. Lett. 72, 116 (1994)

[1.10] P. Politi and J. Villain, Phys. Rev. B 54, 5114 (1996)

[1.11] P. Politi, G. Grenet, A. Marty, A. Ponchet and J. Villain, Phys. Rep. 324, 27 (2002).

[1.12] A. Ballestad et al., Phys. Rev. Lett., 93, 159601 (2004)

[1.13] R. J. Phaneuf, E. D. Williams and N. C. Bartelt, Phys. Rev. B 38, 1984 (1988).

[1.14] R. J. Phaneuf and E. D. Williams, Phys. Rev. Lett. 58, 2563 (1987).

[1.15] Kossel, W., Nach, Ges, Wiss, Göttingen 143, (1927)

[1.16] Stranski, I. N., Z. Phys. Chem 136, 259-278 (1928)

[1.17] A. Kley, P. Ruggerone & M. Scheffler, Phys. Rev. Lett. 79, 5278 (1997).

[1.18] J. Villain, A. Pimpinelli and D. E. Wolf, Comments Condens. Matter Phys. 16, 1 (1992).

[1.19] J. Villain, A. Pimpinelli, L. Tang, and D. E. Wolf, J. Phys. 2, 2107 (1992).

[1.20] P. Kratzer and M. Scheffler, Phys. Rev. Lett. 21, 036102 (2001).

[1.21] G. Ehrlich and F. G. Hudda, J. Chem. Phys. 44, 1039 (1966).

[1.22] R. L. Schwoebel and E. J. Shipsey, J. Appl. Phys. 37, 3682 (1966).

[1.23] R. L. Schwoebel, Journal of Applied Physics 40, 614 (1969).

[1.24] T. Michely et al., J. Phys.:Condens. Matter 14, 4177 (2002)

[1.25] J. E. Van Nostrand, S. J. Chey, and D. G. Cahill, Phys. Rev. B, 57, 12536 (1998).

[1.26] S. J. Liu, E. G. Wang, C. H. Woo and H. C. Huang, J. Computer-Aided Materials Design 7, 195 (2001).

[1.27] E. I. Altman, M. Bienfait, H. P. Bonzel and R. Diehl, “Adsorption on Surfaces and Surface Diffusion”, (Springer, Berlin, 2001).

[1.28] T. Michely & J. Krug, in “Islands, Mounds and Atoms, Patterns and Process in Crystal Growth Far from Equilibrium”, (Springer, Berlin, 2004).

[1.29] M. Li and J. W. Evans, Phys. Rev. B 73, 125434 (2006)

[1.30] Tadayyon-Eslami, PhD dissertation (2006), University of Maryland, College Park

[1.31] A. Ballestad et al., J. of Mat. Sci. and Eng. B SOLID 75: (2-3) 153-156 (2000).

[1.32] W. Brau, "Applied RHEED: Reflection High-Energy Electron Diffraction During Crystal Growth", Springer (Berlin 1999).

[1.33] http://www.wmi.badw.de/methods/leed_rheed.htm

[1.34] J. Krug, P. Politi and T. Michely, arXiv:cond-mat/9912410v1, 22 Dec (1999)

Chapter Two:

[2.1] http://www.microchem.com/Prod-PMMA.htm

[2.2] A. Y. Cho, J. R. Arthur, "Molecular beam epitaxy", Prog. Solid State Chem. 10: 157–192 (1975).

[2.3] Tabassom Tadayyon-Eslami, PhD dissertation (2006), University of Maryland, College Park.

[2.4] V.P. LaBella, M.R. Krause, Z. Ding, P.M. Thibado, Surf. Sci. Rep., 60, 1-53 (2005)

[2.5] http://store.nanoscience.com

[2.6] N. Metropolis, Los Alamos Science, 12, 125 (1987)

[2.7] N. Metropolis, A.W. Rosenbluth, M.N. Rosenbluth, A.H. Teller and E. Teler, J. Chem. Phys. 21, 1087 (1953)

[2.8] J.R. Beeler, Jr., Phys. Rev. 150, 470 (1966)

[2.9] K.A Fichthorn and W.H. Weinberg, J. Chem. Phys. 95, 1090 (1991)

[2.10] P. Kratzer, arXiv:0904.2556v1 [cond-mat.mtrl-sci] 16 Apr (2009)

[2.11] A. Ben-Hamouda, N. Absi, P. E. Hoggan, and A. Pimpinelli, Phys. Rev. B 77, 24530 (2008).

[2.12] A. B. Hamouda, A. Pimpinelli, and T. L. Einstein, Surf. Sci. 602, 3569 (2008).

[2.13] J. L. Roehl, A. Kolagatla, V. K. K. Ganguri, S. V. Khare, and R. J. Phaneuf, Phys. Rev. B 82, 165335 (2010).

[2.14] A. Ballestad et al., Phys. Rev. Lett., 93, 159601 (2004)

[2.15] A. Ballestad et al., J. of Mat. Sci. and Eng. B SOLID 75: (2-3) 153-156 (2000)

Chapter Three:

[3.1] Moore, G.E. Cramming more components onto integrated circuits. Electronics, 38, 1965, pp. 114–117.

[3.2] http://www.itrs.net/reports.html

[3.3] See, for example, S. Mann, Nature Materials 8, 781 (2009).

[3.4] T. I. Kamins and R. S. Williams, Appl. Phys. Lett. 71, 1201 (1997)

[3.5] A. Konkar, R. Heitz, T. R. Ramachandran, P. Chen, and A. Madhukar, J. Vac. Sci. Technol. B 16, 1334 (1998)

[3.6] R. Zhang, R. Tsui, K. Shiralagi, D. Convey, and H. Goronkin, Appl. Phys. Lett. 73, 505 (1998)

[3.7] G. Jin, J. L. Liu, and K. L. Wang, Appl. Phys. Lett. 76, 3591 (2000)

[3.8] H. Lee, J.A. Johnson, M.Y. He, J.S. Speck, and P.M. Petroff, Appl. Phys. Lett. 78, 105 (2001)

[3.9] T. Kitajima, B. Liu, and S. R. Leone, Appl. Phys. Lett. 80, 497 (2002)

[3.10] T. Ogino, Y. Homma, Y. Kobayashi, H. Hibino, K. Prabhakaran, K. Sumitomo, H. Omi, S. Suzuki, T. Yamashtia, D. J. Bottomley, F. Ling, A. Kaneko, Surface Sci. 514, 1 (2002)

[3.11] Z.Y. Zhong, A. Halilovic, M. Mühlberger, F. Schäffler, and G. Bauer, Appl. Phys. Lett. 82, 445 (2003)

[3.12] Z.Y. Zhong, A. Halilovic, M. Mühlberger, F. Schäffler, and G. Bauer, J.Appl. Phys. 93, 6258 (2003)

[3.13] Z.Y. Zhong, A. Halilovic, T. Fromherz, F. Schäffler, and G. Bauer, Appl. Phys. Lett. 82, 4779 (2003)

[3.14] J. L. Gray, S. Atha, R. Hull, and J. A. Floro, Nano Lett. 4, 2447 (2004)

[3.15] B. Yang, F. Liu and M. G. Lagally, Phys. Rev. Lett. 92, 025502 (2004)

[3.16] R.V. Kukta, G. Petroff, and D. Kouris, J. Appl. Phys. 97, 033527 (2005)

[3.17] J. L. Gray, R. Hull, and J. A. Floro, J. Appl. Phys., 100, 084312 (2006)

[3.18] A. Pascale, I. Berbezier, A. Ronda, and P. C. Kelires, Phys. Rev. B 77, 075311 (2008)

[3.19] A. T. N'Diaye, S. Bleikamp, P.J. Feibelman, and T. Michely, Phys. Rev. Lett. 97, 215501 (2006)

[3.20] H. Hu, H.J. Gao and F. Liu, Phys. Rev. Lett. 101, 216102 (2008)

[3.21] G. Ehrlich and F.G. Hudda, J. Chem. Phys. 44, 1039 (1966)

[3.22] R.L. Schwoebel and E.J. Shipsey, J. Appl. Phys. 37, 3682 (1966)

[3.23] M.D. Johnson, C. Orme, A.W. Hunt, D. Graff, J.L. Sudijono, L.M. Sander, and B.G. Orr, Phys. Rev. Lett. 72 116 (1994)

[3.24] P. Politi and J. Villain, Phys. Rev. B 54, 5114 (1996)

[3.25] J. Camarero, V. Cross, M.J. Capitán, J. Álvarez, S. Ferrer, M.A. Niño, J.E. Prieto, L. Gómez, J. Ferrón, A.L. Vázquez de Parga, J.M. Gallego, J.J. de Miguel and R. Miranda, Appl. Phys. A 69, 553 (1999)

[3.26] S. Schinzer, S. Kohler and G. Reents, Eur. Phys. J. B 15, 161 (2000)

[3.27] M. Vladimirova, A. Pimpinelli and A. Videcoq, J. Cryst. Growth 222, 631 (2000)

[3.28] H.-C. Kan, S. Shah, T. Tadayyon-Eslami, and R. J. Phaneuf, Phys. Rev. Lett. 92, 146101 (2004)

[3.29] Z-J. Liu and Y.G. Shen, Surface Sci. 595 20 (2005)

[3.30] A.B.H. Hamouda, A. Pimpinelli and R.J. Phaneuf, Surface Sci. 602, 2819 (2008)

[3.31] J. Krug, V. Tonchev, S. Stoyanov, and A. Pimpinelli, Phys. Rev. B 71, 045412 (2005)

[3.32] G.S. Bales, and A. Zangwill, Phys. Rev. B, 41, 5500 (1990)

[3.33] T. Tadayyon-Eslami, H.-C. Kan, L.C. Calhoun, and R.J. Phaneuf, Phys. Rev. Lett. 97, 126101 (2006)

[3.34] A. Ben-Hamouda, N. Absi, P.E.. Hoggan, and A. Pimpinelli, Phys. Rev. B 77 24530 (2008)

[3.35] A.B-H. Hamouda, A. Pimpinelli, and T.L. Einstein, Surface Sci. 602, 3569 (2008)

[3.36] These values are close to those based upon first principles calculations for c(4x4)-GaAs(001) by Roehl et al., ref. [37].

[3.37] J. Roehl, A. Kolagatla, V.K.K. Ganguri, S.V. Khare, and R.J. Phaneuf, Phys. Rev. B 82, 165335 (2010)

[3.38] P. Bak, Rep. Prog. Phys. 45, 587 (1982)

[3.39] C.-F. Lin, H.-C. Kan, S. Kanakaraju, C.J.K. Richardson, N.C. Bartelt and R.J. Phaneuf, in preparation (2012).

[3.40] C.–F. Lin, A. B.H. Hammouda, H. –C. Kan, N.C. Bartelt, and R. J. Phaneuf, Phys. Rev. B 85, 085421 (2012)

[3.41] T.L. Einstein, Appl. Phys. A 87, 375-384 (2007)

[3.42] A. Pimpinelli and T. L. Einstein, Phys. Rev. Lett. 99, 226102 (2007)

[3.43] A.-L. Barabasi and H. E. Stanley, "Fractal Concepts in Surface Growth", Cambridge University Press 1995.

Chapter Four:

[4.1] S. Mann, Nature Materials 8, 781 (2009)

[4.2] C.–F. Lin, A. B-H. Hammouda, H. –C. Kan, N.C. Bartelt, and , R. J. Phaneuf, Phys. Rev. B 85, 085421 (2012)

[4.3] T. Tadayyon-Eslami, H.–C. Kan, L. C. Calhoun, and R. J. Phaneuf, Phys. Rev. Lett. 97, 126101 (2006)

[4.4] G. Ehrlich, and F. G. Hudda, J. Chem. Phys. 44, 1039 (1966)

[4.5] R.L. Schwoebel and E.J. Shipsey, J. Appl. Phys. 37, 3682 (1966)

[4.6] D.E. Jesson, G. Chen, K.M. Chen and S.J. Pennycook, Phys. Rev. Lett. 80, 5156 (1998)

[4.7] M. Kästner and B. Voigtländer, Phys. Rev. Lett. 82, 2745 (1999)

[4.8] M.D. Johnson, C. Orme, A.W. Hunt, D. Graff, J. Sudijono, L.M. Sander, and B.G. Orr, Phys. Rev. Lett. 72, 116 (1994)

[4.9] M. Li and J.W. Evans, Phys. Rev. B 73, 125434 (2006)

[4.10] J. Roehl, A. Kolagatla, V.K.K. Ganguri, S.V. Khare, S.V. and R.J. Phaneuf, Phys. Rev. B 82, 165335 (2010)

[4.11] M. Itoh, Phys. Rev. B 64, 045301 (2001)

[4.12] T. Shitara, D.D. Vvedensky, M.R. Wilby, J. Jhang, J.H. Neave and B.A. Joyce, Phys. Rev. B 46, 6825 (1992); . Shitara, J. Zhang, J.H. Neave and B.A. Joyce, J. Appl. Phys. 71, 4299 (1992)

[4.13] M. Itoh, G. R. Bell, A.R. Avery, B.A. Joyce, and D.D. Vvedensky, Phys. Rev. Lett. 81, 633 (1998); G.R. Bell, T.S. Jones and B. A. Joyce, Surface Sci. 429, L492 (1999)

[4.14] S. Shah, T.J. Garrett, K. Limpaphayom, T. Tadayyon-Eslami, H.-C. Kan, and R.J. Phaneuf, Appl. Phys. Lett. 83, 4330 (2003)

[4.15] H.-C. Kan, R. Ankam, S. Shah, K.M. Micholsky, T. Tadayyon-Eslami, L.C. Calhoun, and R.J. Phaneuf, Phys. Rev. B 73, 195410 (2006)

[4.16] H.-C. Kan, S. Shah, T. Tadayyon-Eslami, and R.J. Phaneuf, Phys. Rev. Lett. 92, 146101 (2004)I

[4.17] X. Deng and M. Krishnamurthy, Phys. Rev. Lett. 81, 1473 (1998)

[4.18] P. Kratzer and M. Scheffler, Phys. Rev. Lett. 88, 036102 (2002)

[4.19] C.G. Morgan, P. Kratzer, and M. Scheffler, Phys. Rev. Lett. 82, 4886 (1999)

[4.20] M. Giesen, G. Schulze Icking-Konert, and H. Ibach, Phys. Rev. Lett. 82, 3101 (1999)

[4.21] J. Krug, Physica A 313, 47 (2002)

[4.22] G. R. Bell, T. S. Jones, and B. A. Joyce, Surf. Sci. 429, L492 (1999).

[4.23] M. Itoh and T. Ohno, Phys.Rev.B 63, 125301 (2001).

[4.24] M. Itoh, G. R. Bell, A. R. Avery, T. S. Jones, B. A. Joyce, and D. D. Vvedensky, Phys.Rev.Lett.81, 633 (1998).

[4.25] T. Shitara, J. Zhang, J. H. Neave, and B. A. Joyce, J. Appl. Phys. 71, 4299 (1992).

[4.26] T.Shitara, D.D.Vvedensky,M.R.Wilby,J.Zhang,J.H.Neave, and B. A. Joyce, Phys. Rev. B 46, 6825 (1992).11-3

[4.27] P. Politi and J. Villain, Phys. Rev. B 54, 5114 (1996)

[4.28] P. Politi, G. Grenet, A. Marty, A. Ponchet, and J. Villain, Phys. Rep. 324, 271 (2000)

[4.29] A. Ballestad et al., Phys. Rev. Lett., 93, 159601 (2004)

[4.30] A. Ballestad et al., J. of Mat. Sci. and Eng. B SOLID 75: (2-3) 153-156 (2000)

[4.31] G. Lengel, R. J. Phaneuf, E. D. Williams, S. Das Sarma, W. T. Beard & F. G. Johnson, Phys. Rev. B 60, R8469 (1999).

[4.32] C.-F. Lin, H.-C. Kan, S. Kanakaraju, SC.J.K. Richardson, N.C. Bartelt and R.J. Phaneuf, in preparation (2012).

Appendix A:

[A.1] T. Tadayyon-Eslami, H. –C. Kan, L. C. Calhoun, and R. J. Phaneuf, Phys. Rev. Lett. 97, 126101 (2006)

[A.2] H.-C. Kan, S. Shah, T. Tadayyon-Eslami, and R. J.Phaneuf, Phys. Rev. Lett. 92, 146101 (2004)

[A.3] S. Shah, T. J. Garrett, K. Limpaphayom, T. Tadayyon-Eslami, H. C. Kan, and R. J. Phaneuf, Appl. Phys. Lett. 83, 4330 (2003).

[A.4] C.-F. Lin, H. –C. Kan, S. Kanakaraju, C. J. Richardson and R.J Phaneuf, in preparation (2012)

[A.5 G. Ehrlich, and F. G. Hudda, J. Chem. Phys. 44, 1039 (1966)..

[A.6] R. L. Schwoebel, and E. J. Shipsey, J. Appl. Phys. 37, 3682 (1966)

[A.7] C. –F. Lin, A. B. Hammouda, H. –C. Kan, N. C. Bartelt, and R. J. Phaneuf, Phys. Rev. B 85, 085421 (2012)

[A.8] X. Deng, and M. Krishnamurthy, Phys. Rev. Lett. 81, 1473 (1998)

[A.9] M. Kawabe and T. Sugaya, Jpn. J. Appl. Phys. 28, L1077 (1989)

[A.10] M. Hata, T. Isu, A. Watanabe, Y. Katayama, J. Vac. Sci. Techonl. B 8 692 (1990)

[A.11] Y. Kangawa et al., Applied Surf. Sci. 190, 517 (2002)

[A.12] K. Kanisawa and H. Yamaguchi, Phys. Rev. B 56, 12080 (1997)

[A.13] X. –Q. Shen, T. Nishinaga, Jpn. J. Appl. Phys. 32 (1993)

[A.14] T. Sugaya, T. Nakagawa, Y. Sugiyama and Y. Tanuma, Jpn. J. Appl. Phys.36, 5670 (1997)

[A.15] S. Koshiba, J. Appl. Phys. 76, 4138 (1994)

Appdenix B:

[B.1] T.L. Einstein, Appl. Phys. A 87, 375-384 (2007)

[B.2] A. Pimpinelli and T. L. Einstein, Phys. Rev. Lett. 99, 226102 (2007)

[B.3] T. Guhr, Phys. Reports 299 (1998) 189